

How do clouds and other “surfaces” change the effective radius of a transiting exoplanet?

Yan Bétrémieux (Section 326), Mark R. Swain (Section 326)

“SURFACES” ...

- DECREASE CONTRAST OF SPECTRAL FEATURES
- CHANGE SLOPE WITH WAVELENGTH OF RAYLEIGH SCATTERING SIGNATURE
- WIDEN SPECTRAL FEATURES

Lecavelier des Etangs et al. (2008):

EXOPLANET EFFECTIVE RADIUS OCCURS WHERE SLANT OPTICAL DEPTH = 0.56

DOES NOT INCLUDE “SURFACES”

HOWEVER...

ALL EXOPLANETS HAVE “SURFACES”!

ALL?

ALL!

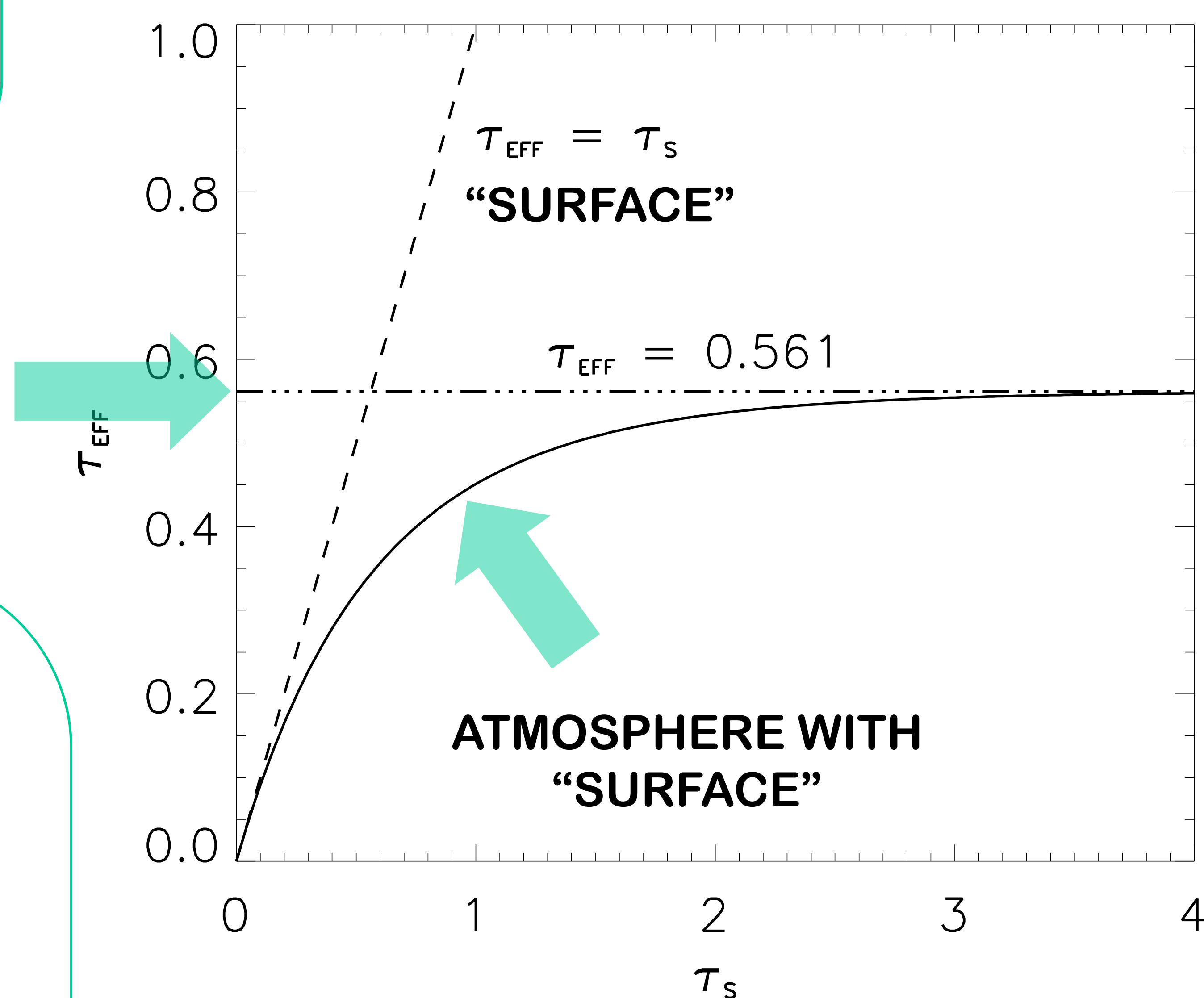
- SURFACE → ROCKY WORLDS
- THICK CLOUD DECK
→ MANY EXOPLANETS HAVE CLOUDS
- ALL OTHERS HAVE REFRACTIVE BOUNDARIES
 - ❖ Bétrémieux & Kaltenegger 2014, 2015
 - ❖ Bétrémieux 2016

ANALYTICAL FORMALISMS ALLOW ONE TO:

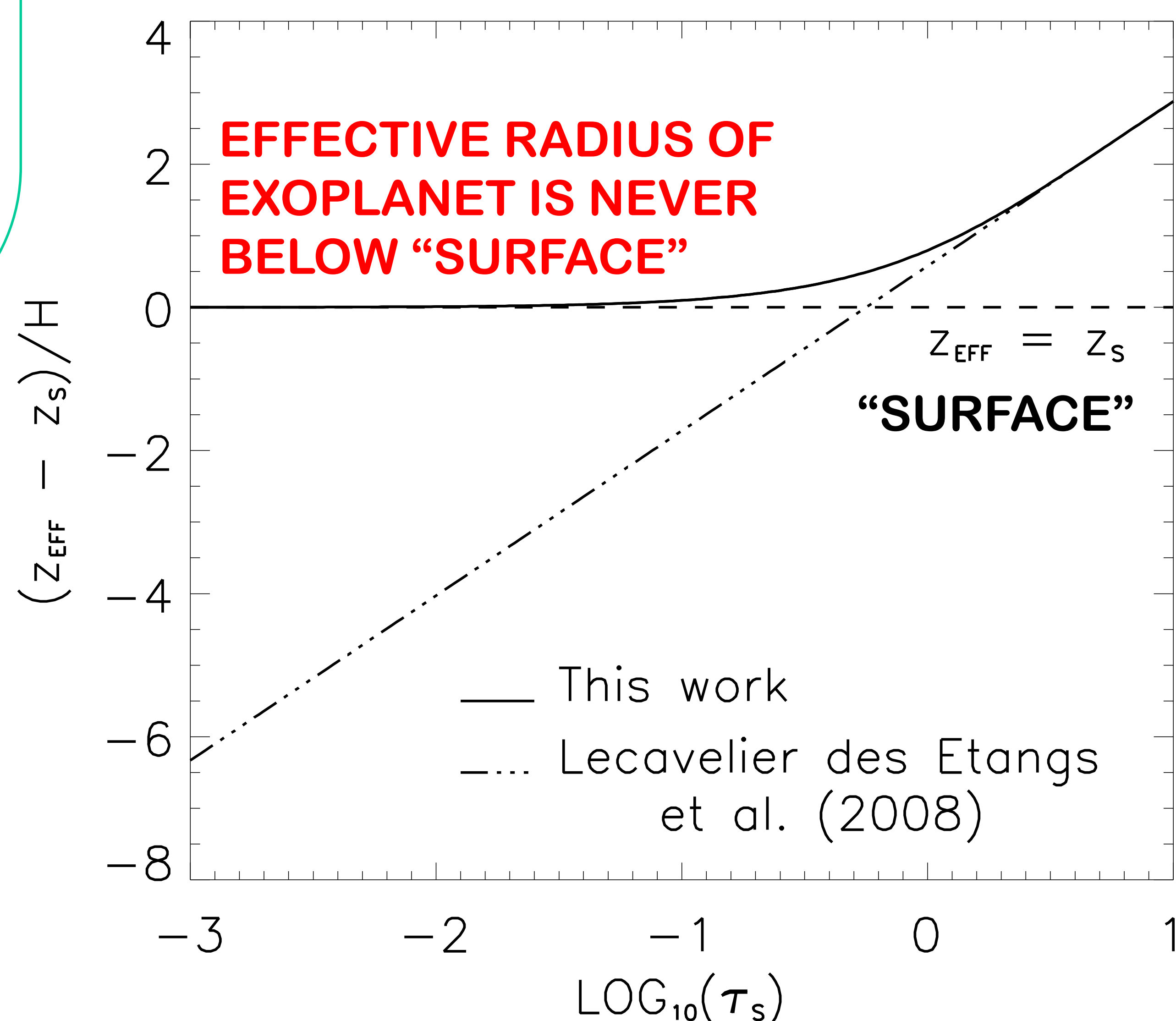
- UNDERSTAND TRANSMISSION SPECTRA
- TEST RADIATIVE TRANSFER CODES
- DESIGN A FAST ATMOSPHERE PARAMETER RETRIEVAL ALGORITHM

WE HAVE DERIVED AN ANALYTICAL FORMALISM WHICH INCLUDES “SURFACES”

EFFECTIVE SLANT OPTICAL DEPTH VS. SLANT OPTICAL DEPTH AT “SURFACE”



EFFECTIVE RADIUS WITH RESPECT TO “SURFACE” (DISTANCE IN ATMOSPHERE SCALEHEIGHT)



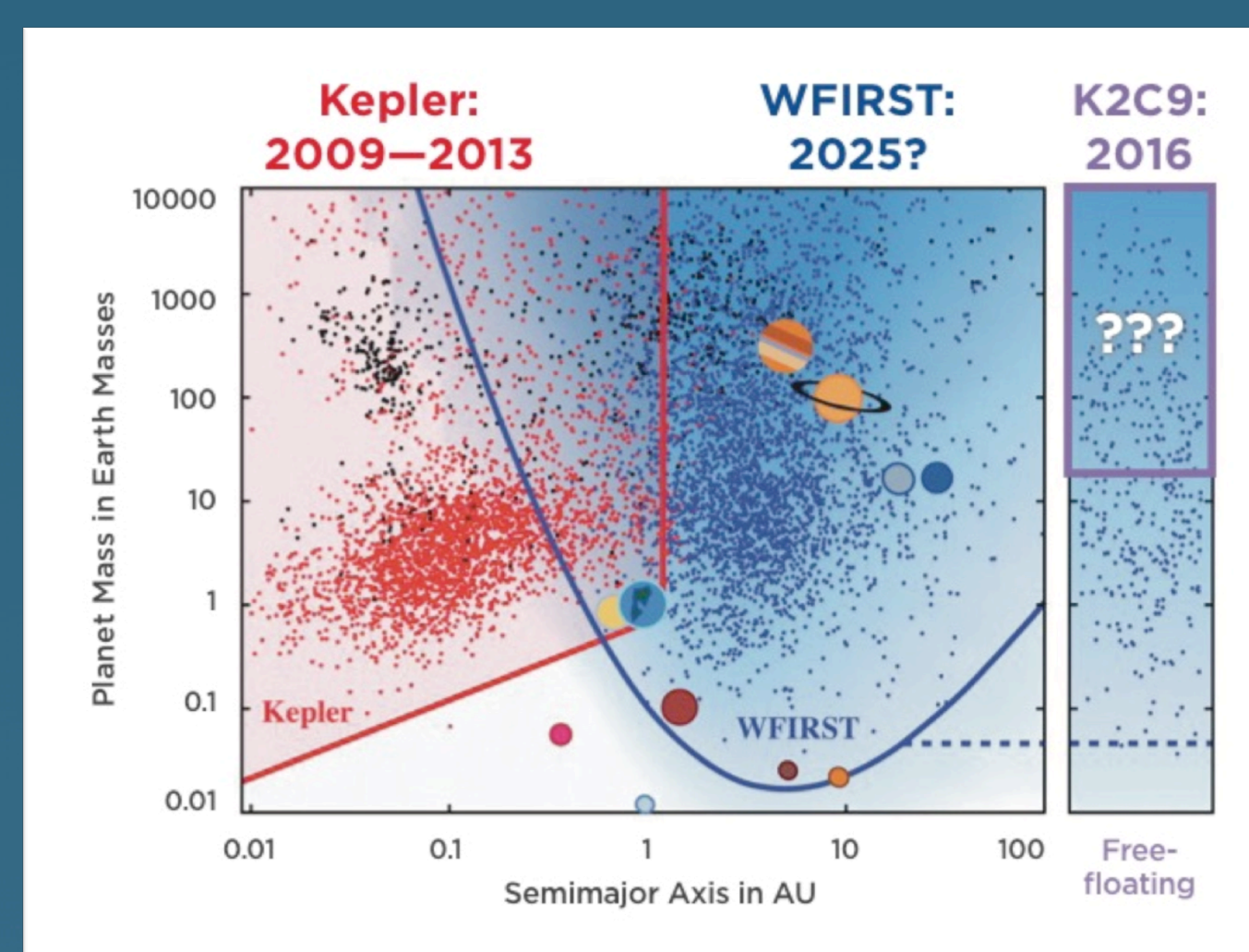
Illuminating the Demographics of Free-floating Exoplanets with Ground- and Space-based Telescopes

Author: Calen B. Henderson (3262)

Coauthor: Yossi Shvartzvald (3262)

Background

A microlensing event occurs when the light from a background "source" star is temporarily magnified by the gravitational potential of an intervening foreground "lens" system. This technique complements other exoplanet discovery methods, and a recent result warrants confirmation.

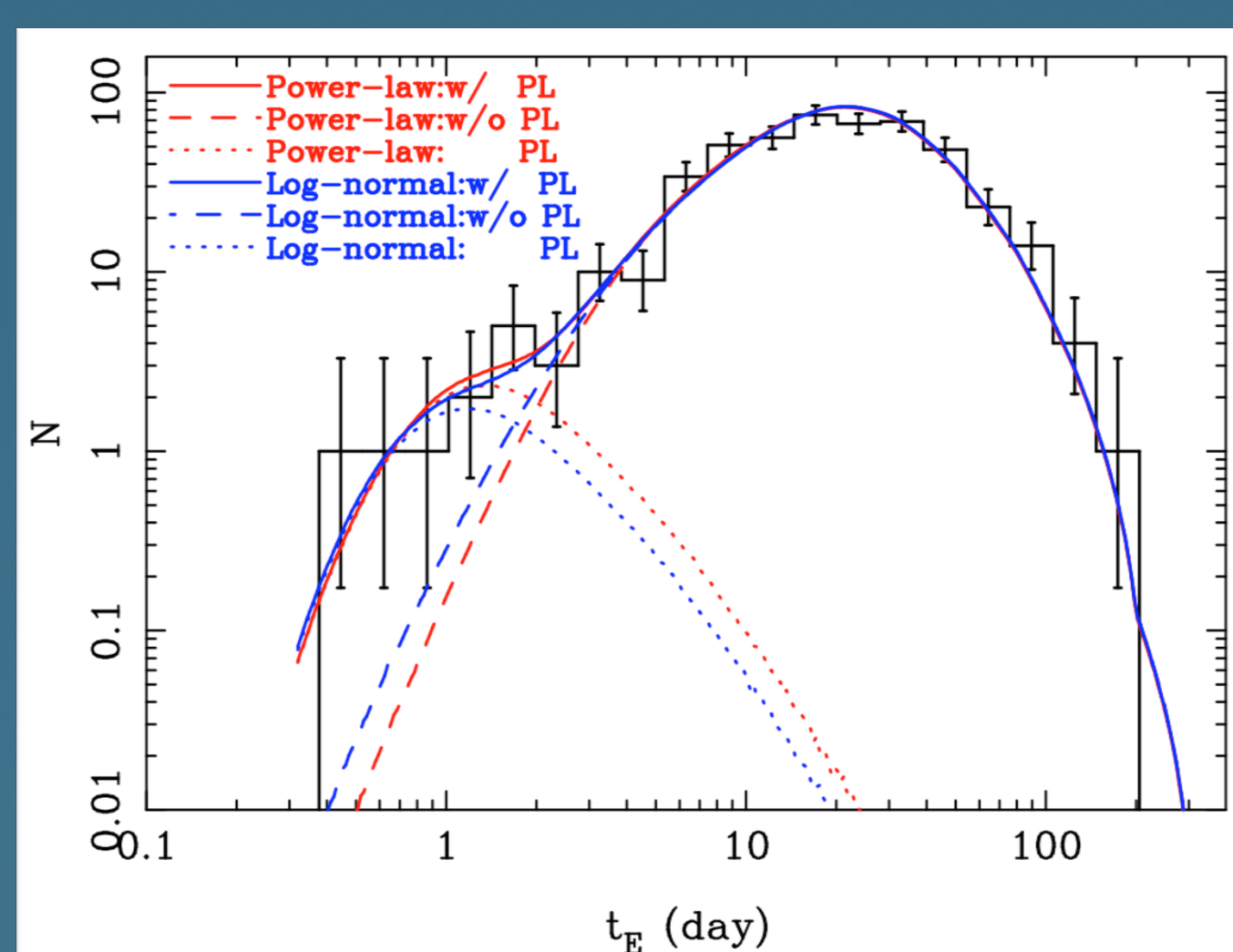


Adapted from a figure created by Matthew Penny and originally found in: Spergel, D., et al. 2015, arXiv:1503.03757

Exoplanet Census

The *Kepler* spacecraft has used the transit technique to discover over 2,300 exoplanets, providing excellent demographic information for planets orbiting close-in to their host stars. A decade from now, the *WFIRST* mission will use microlensing to continue this census begun by *Kepler*, extending our knowledge into the outer reaches of planetary systems. *K2*'s Campaign 9, which completed in July of this year, provides an opportunity to probe a hitherto-unexplored third reservoir of exoplanets – free-floating planets, which are not gravitationally tethered to any host star.

This figure shows simulation-based predictions for the planet mass and orbital distance results from *Kepler*, *WFIRST*, and *K2*'s Campaign 9.



Sumi, T., et al. 2011, *Nature*, 473, 349

Free-floating Planet Candidates

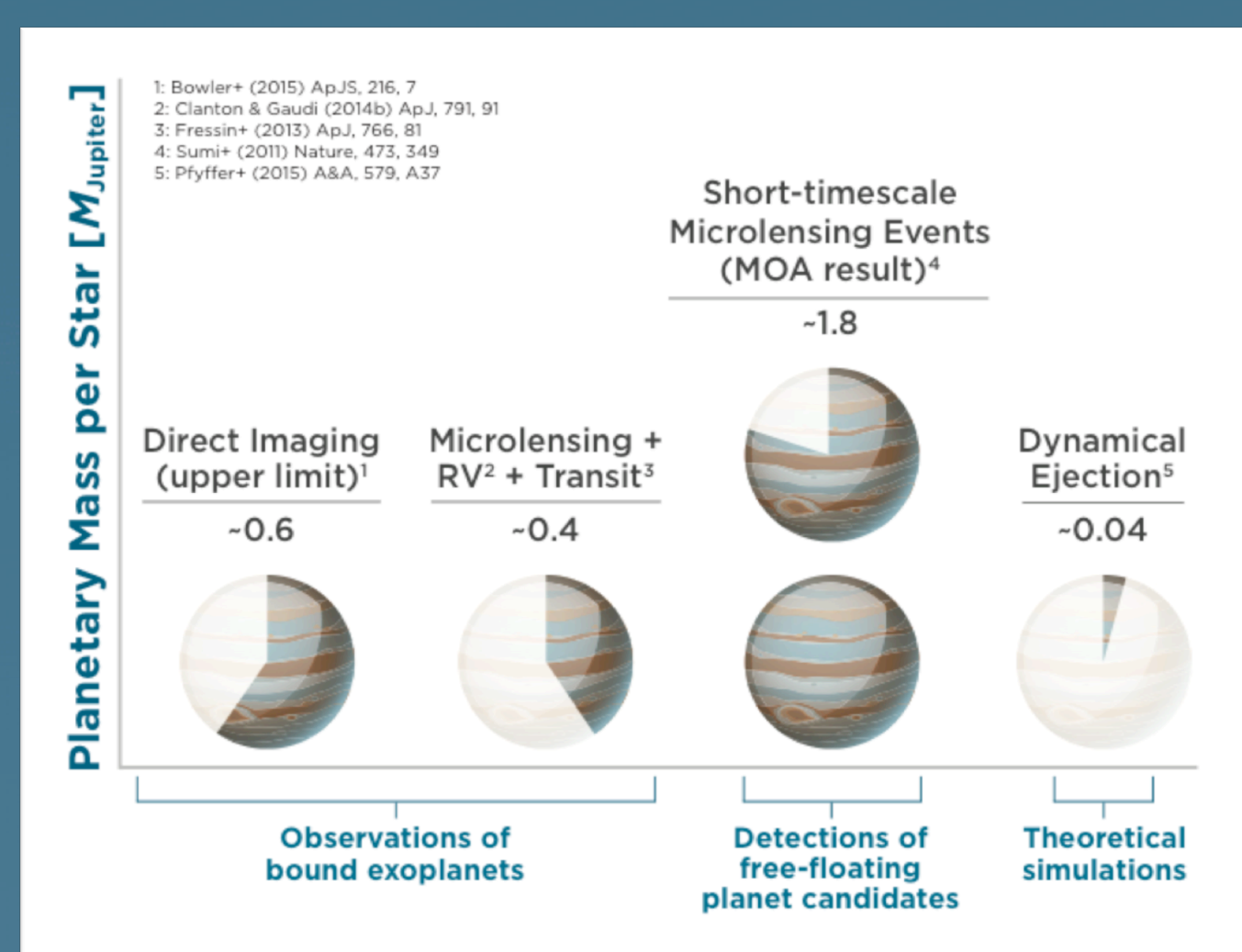
In 2011, the MOA survey group announced the discovery of an abundance of microlensing events with short timescales above what their Galactic model predicted. The timescale t_E increases with the mass of the lensing object. They thus inferred the cause of this excess to be a population of "unbound or distant planetary-mass" objects with masses comparable to that of Jupiter and outnumbering stars by a ratio of nearly 2:1.

This figure shows the histogram of the timescale t_E for the MOA sample, emphasizing the unexpected bump at $t_E \sim 1$ day.

Planetary Mass Budget

The putative population of free-floating planets revealed by the MOA survey implies the existence of ~ 2 Jupiter-mass free-floating planets per star. This abundance stands in stark contrast to observations of bound planetary systems as well as simulations of the formation and evolution of exoplanets. This implies that, if the short-timescale events found by MOA are free-floating planets, these objects dominate the mass budget of planet formation. However, the masses of these lensing objects must be measured to exclude other astrophysical phenomena as the cause.

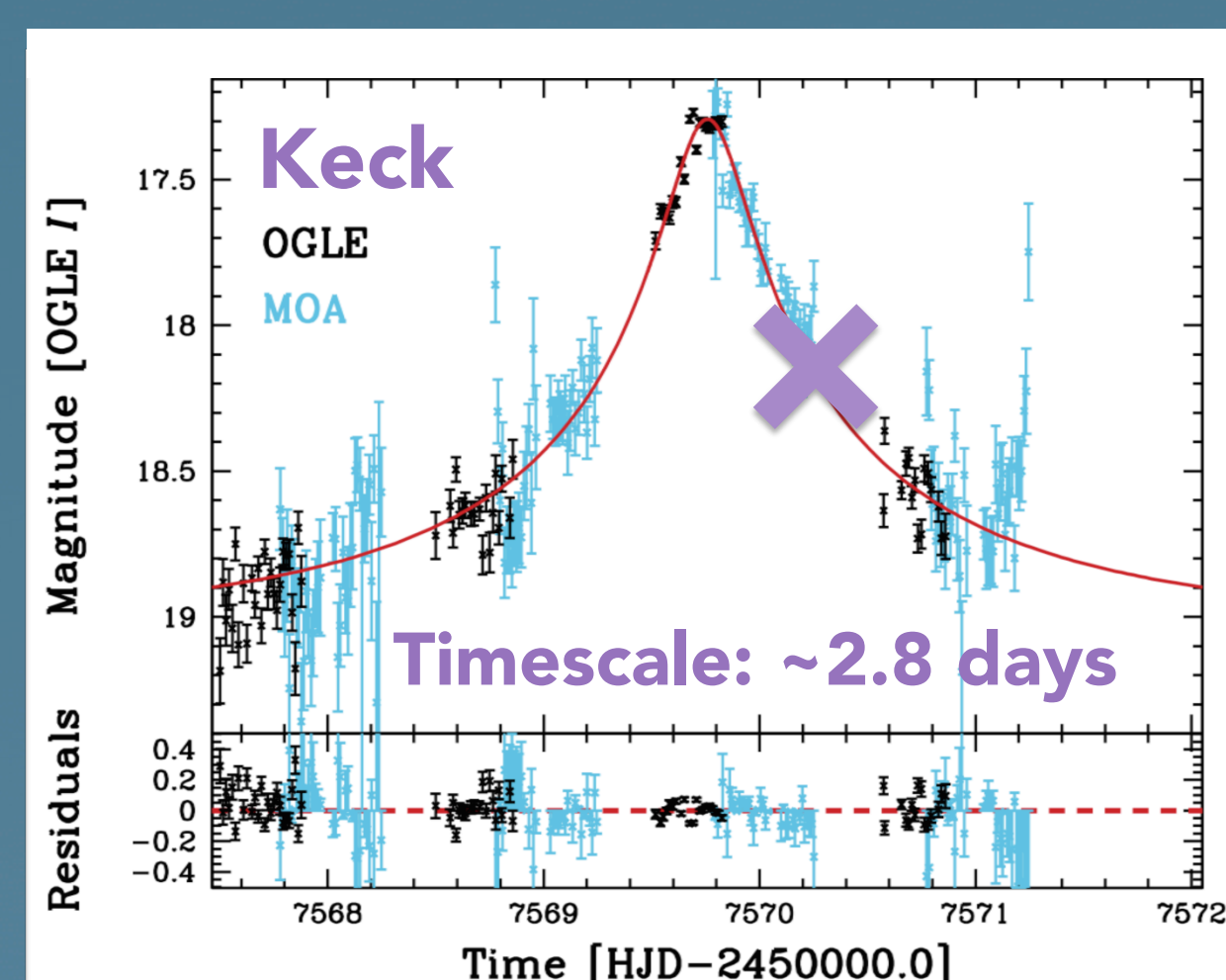
This figure shows an approximate accounting of the planetary mass per star from various observational and theoretical constraints.



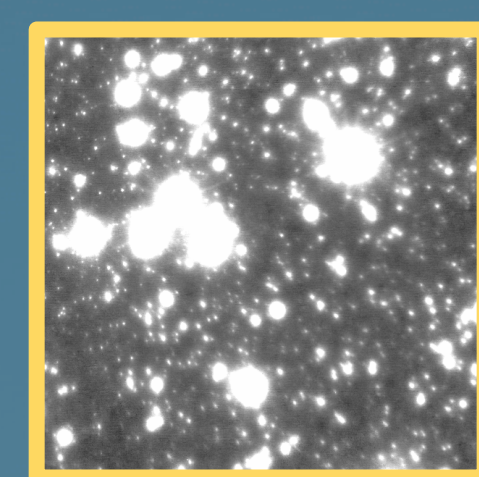
Henderson, C. B., et al. 2015, arXiv:1512.09142

Early Results!!!

Already, 13 microlensing events with a timescale shorter than 3.0 days have been discovered in the *K2C9* survey area by ground-based telescopes. I am currently leading efforts to model the light curves of these short-timescale events in order to: A) eliminate false positives and B) measure the timescales precisely.



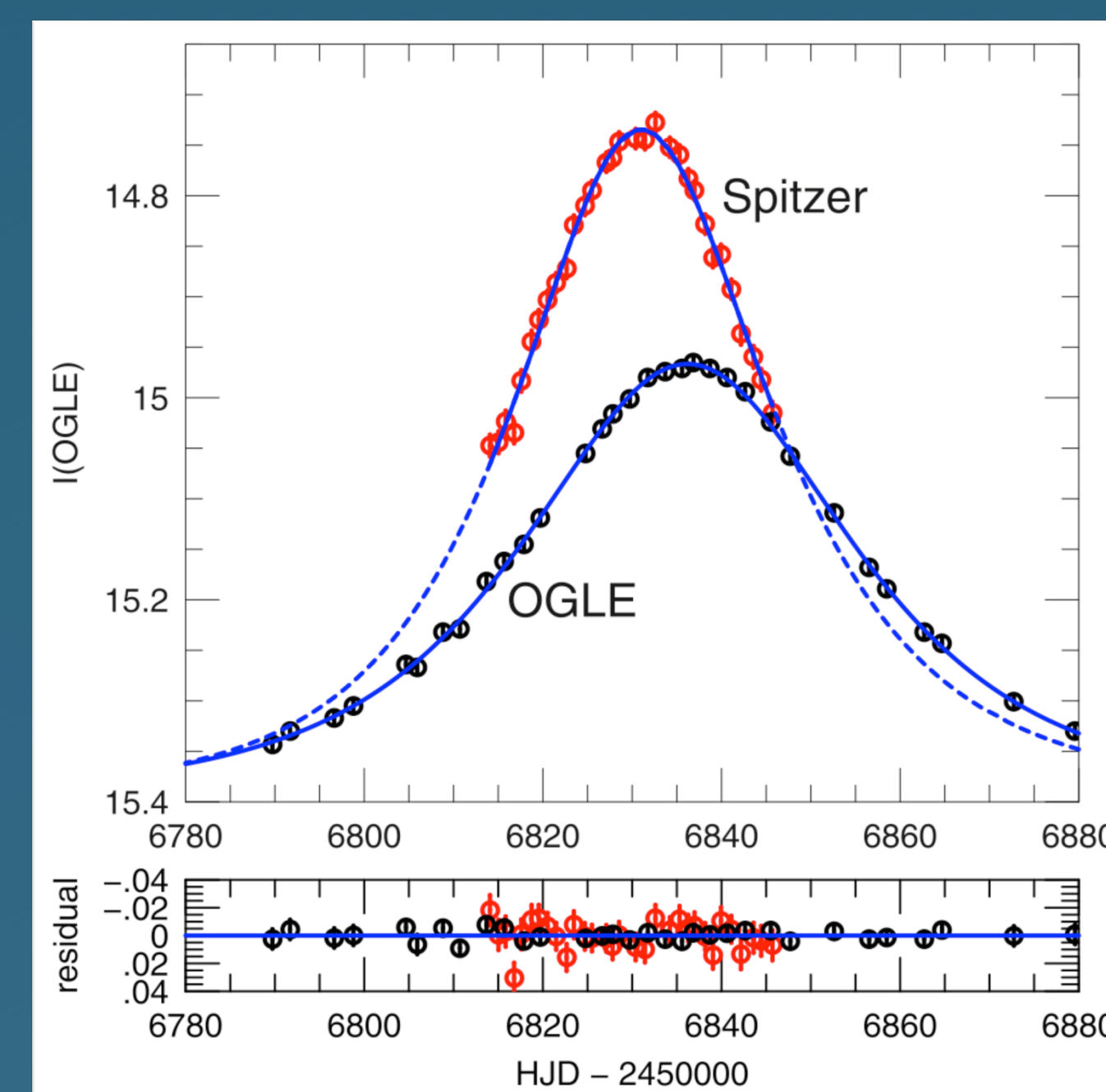
Example Ground-based Light Curve (Preliminary!)



High-resolution Keck Follow-up Image

Mass and Host Star Analysis

I led or co-led efforts during *K2C9* to obtain NIR flux measurements of the source stars using: A) UKIRT (survey), B) ANDICAM (targeted follow-up), and C) Keck (target-of-opportunity triggers). I have also obtained the necessary high-resolution follow-up data using Keck (image on left) in preparation for the release of the *K2C9* data in September, at which point I will measure the satellite parallaxes. In the subsequent months, I and my team will thus be able to measure the mass of the lensing objects for all short-timescale microlensing events discovered during *K2C9* and also determine whether the planetary-mass lensing objects are gravitationally bound or indeed free-floating.

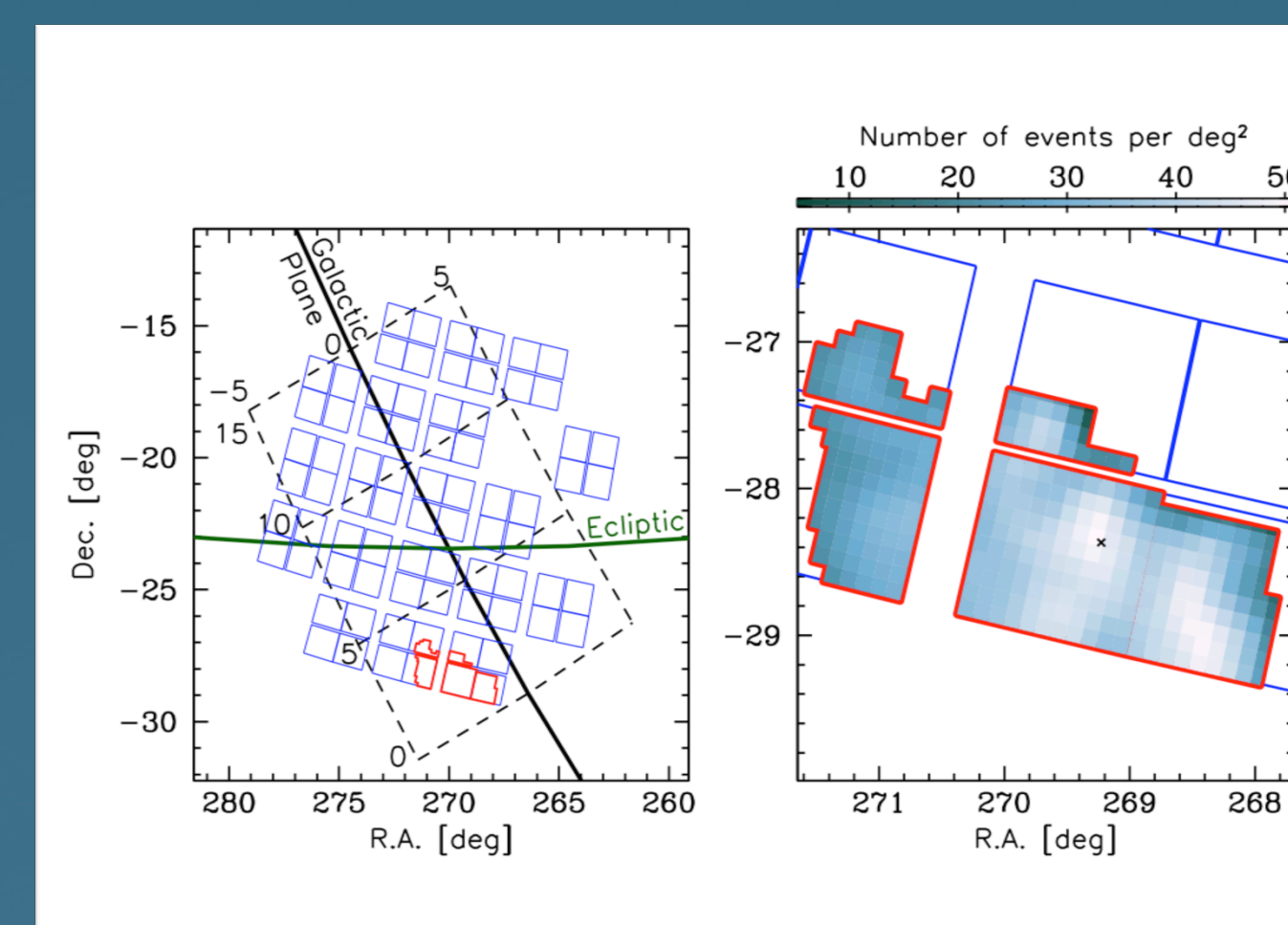


Yee, J. C., et al. 2015, *ApJ*, 810, 155

Measuring Lens Mass

By observing the same region simultaneously from the ground and from space it is possible to measure the satellite parallax. This refers to the shift in the time and magnitude of the magnification of the source in the ground-based light curve compared to the light curve seen from space. With a satellite parallax measurement it is possible to determine the mass of the lens. The *Spitzer* satellite has been used to measure satellite parallaxes – and thus lens masses – for ~ 200 microlensing events. However, short-timescale events are impossible for it to observe, given its inherent ≥ 4 -day lag between target selection and observation. Doing so thus requires automated observations of the same survey area from the ground and from space.

This figure shows the light curve for a microlensing event observed by *Spitzer* and by the ground-based OGLE survey group.



Henderson, C. B., et al. 2015, arXiv:1512.09142

K2's Campaign 9 (K2C9)

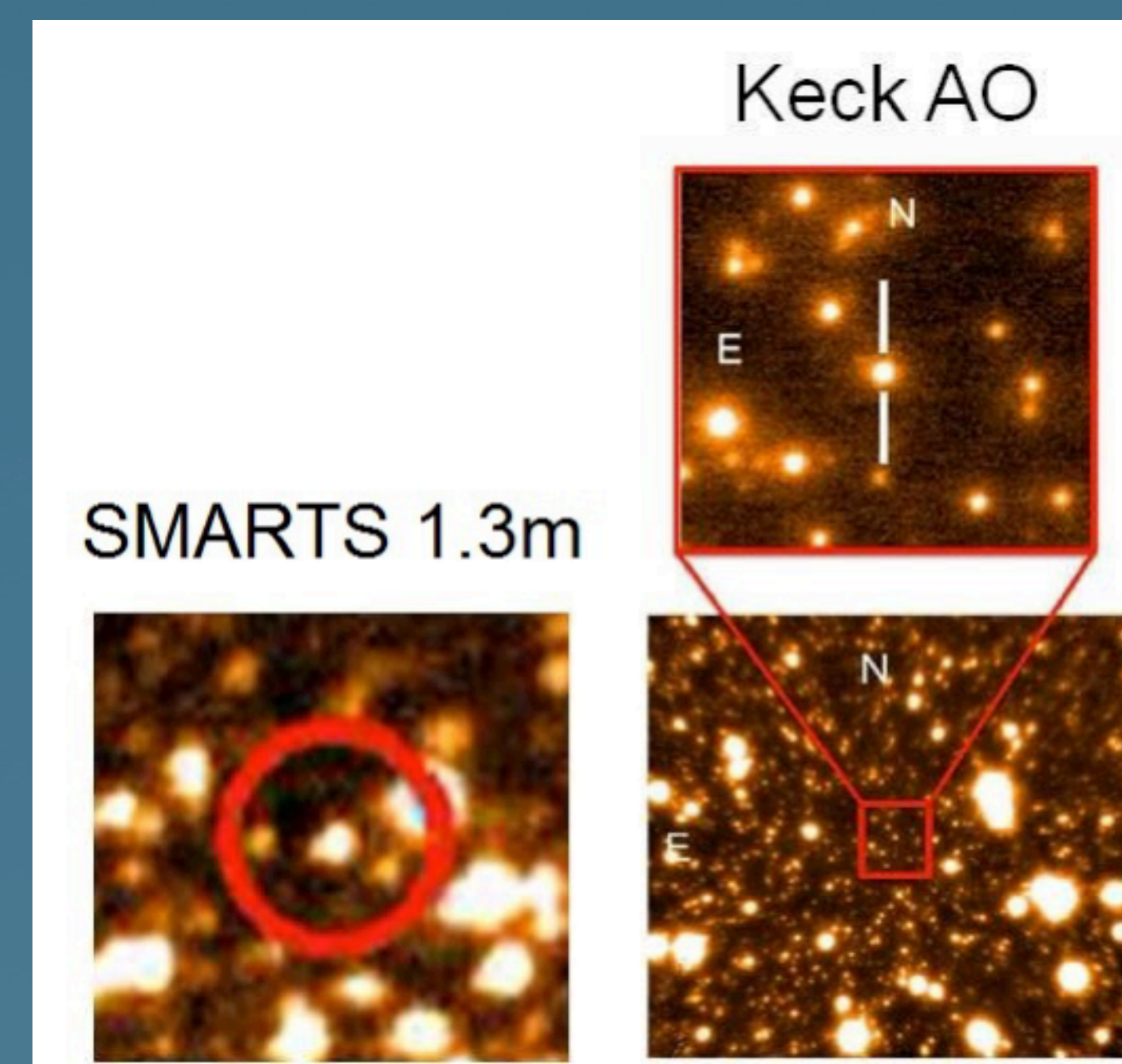
On 2/July of this year, *K2C9* completed a 72-day, 3.74 square-degree automated microlensing survey toward the center of our Milky Way Galaxy. This will facilitate satellite parallax measurements for the ~ 200 events that have already been discovered in the survey area with ground-based telescopes. Coupling data from *K2C9* with data from the ground will thus help determine if the cause of these short-timescale events is indeed a population of planetary-mass objects.

This figure shows the survey area for *K2C9*, outlined in red, on the plane of the sky. The zoom-in (right panel) gives an estimate of the predicted event rate within the survey area.

Searching for Host Stars

The final step is to search the planetary lens for a host star. This requires taking near-infrared (NIR) data at two epochs: (1) during the microlensing event while the source star is magnified, and (2) after the event is over and the source has returned to its baseline brightness. The coupling of these two allows for the NIR flux of the source to be measured. Then, high-resolution NIR follow-up resolves out all stars not dynamically associated with the event, allowing any flux in excess of the source flux to be attributed to a lens host star, proving that the cause of the initial short timescale is a planet that is widely separated from its parent star, but *not* free-floating!

This figure shows how high-resolution imaging with Keck will resolve out all stars except the source and lens, facilitating a search for a potential host star to the planet.



Batista, V., et al. 2014, *ApJ*, 780, 54

Occurrence of Giant Planets around Stars with Dusty Debris Disks

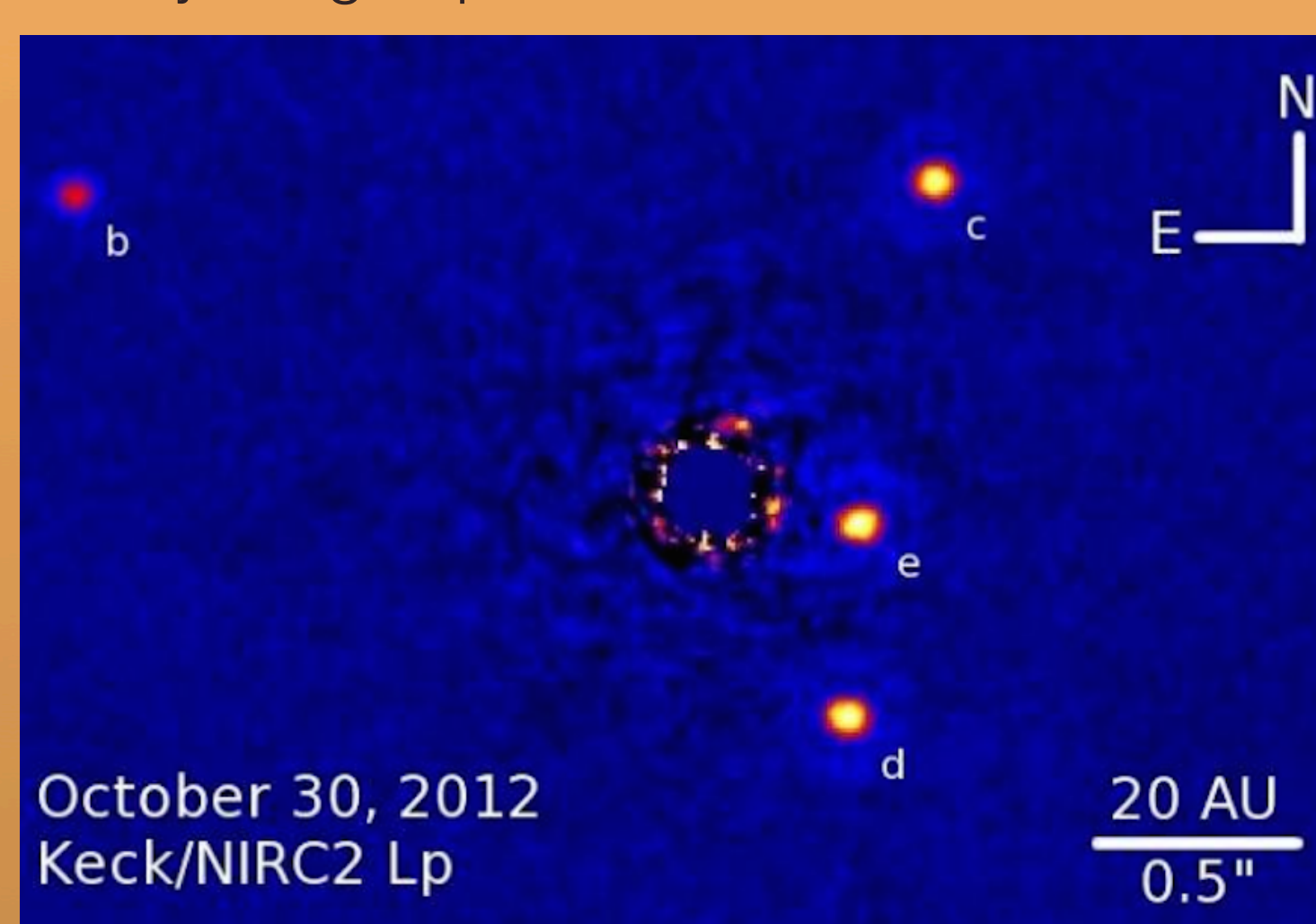
Author: Tiffany Meshkat (3262)

Dimitri Mawet (3262), Karl Stapelfeldt (3260), Sasha Hinkley (Exeter U.), Marta Bryan (Caltech)

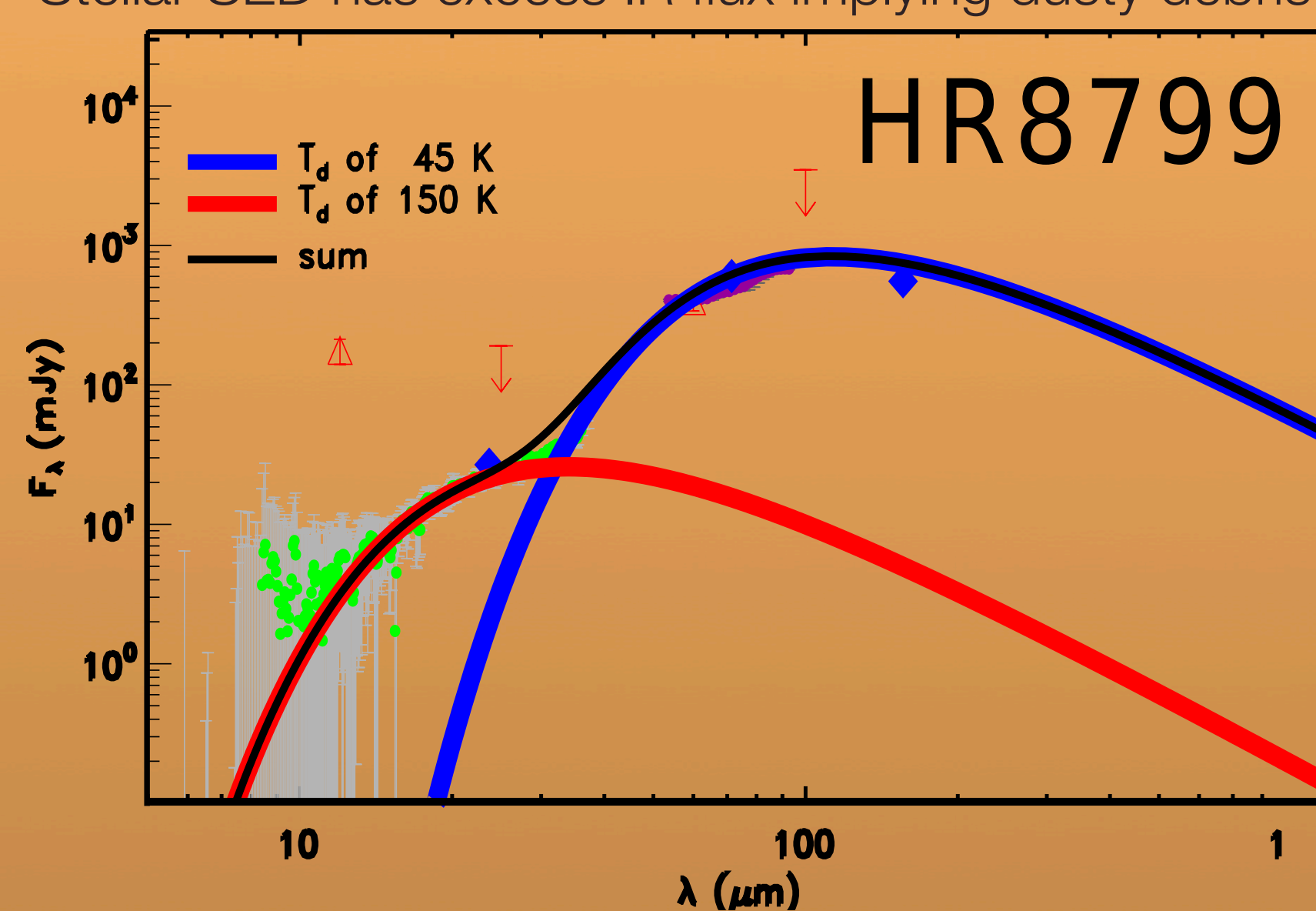
Are debris disks signposts for planets?

Debris disks are circumstellar dust clouds, generated in collisional cascades of asteroids and comets. These small bodies are the remnants of planetesimals¹, which are thought to be the building blocks of planet cores. This connection between debris disks and planets has been seen in several of the currently imaged planetary systems (see HR8799 below), suggesting that debris disks may be signposts for planets.

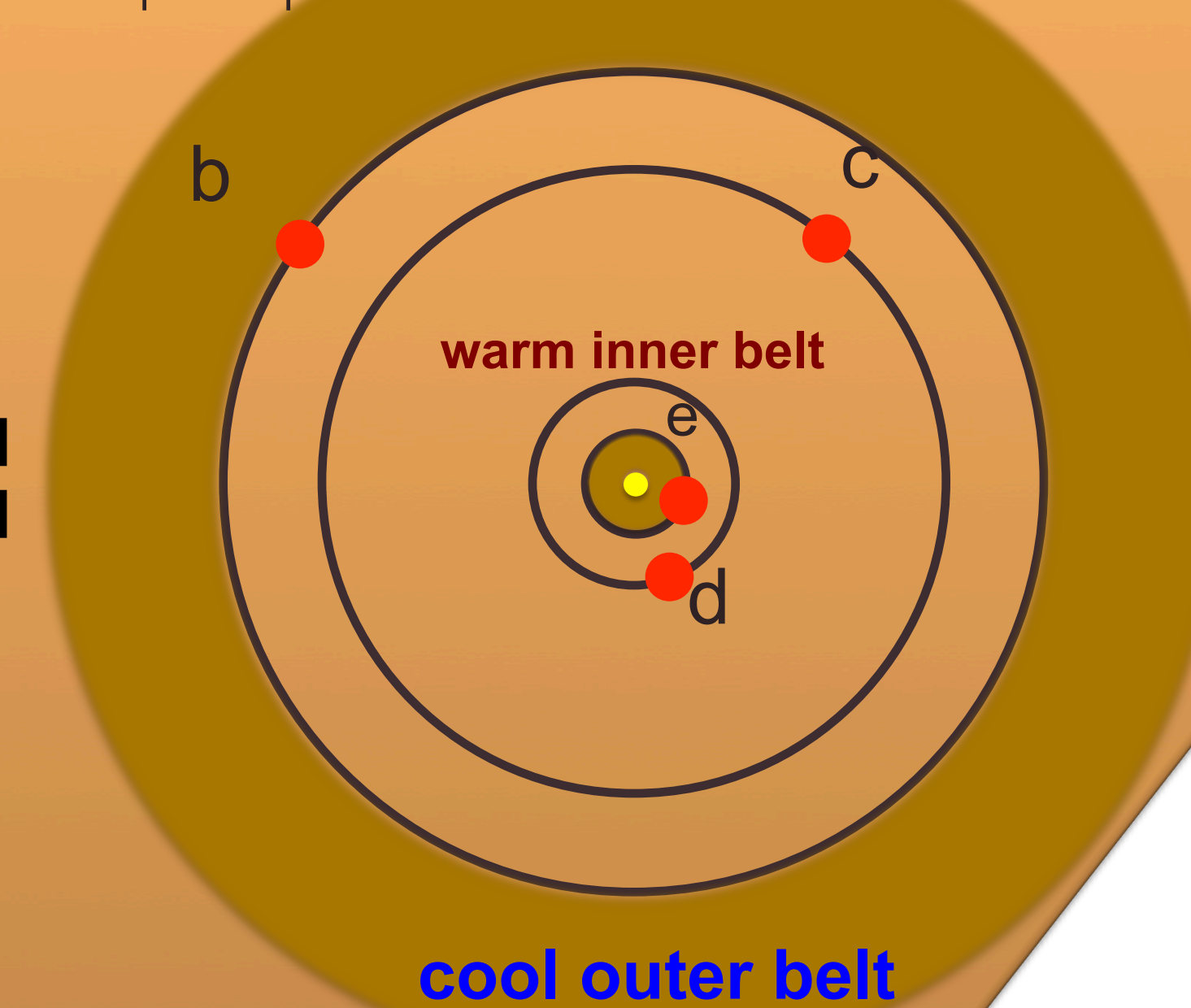
Directly imaged planets around the star HR 8799



Stellar SED has excess IR flux implying dusty debris disk



Complete picture of the HR 8799 architecture



Our Sample

We identified stars with debris disks by searching for the signature excess infrared flux similar to HR 8799 above, using *Spitzer* data⁵. In total, we obtained data on:

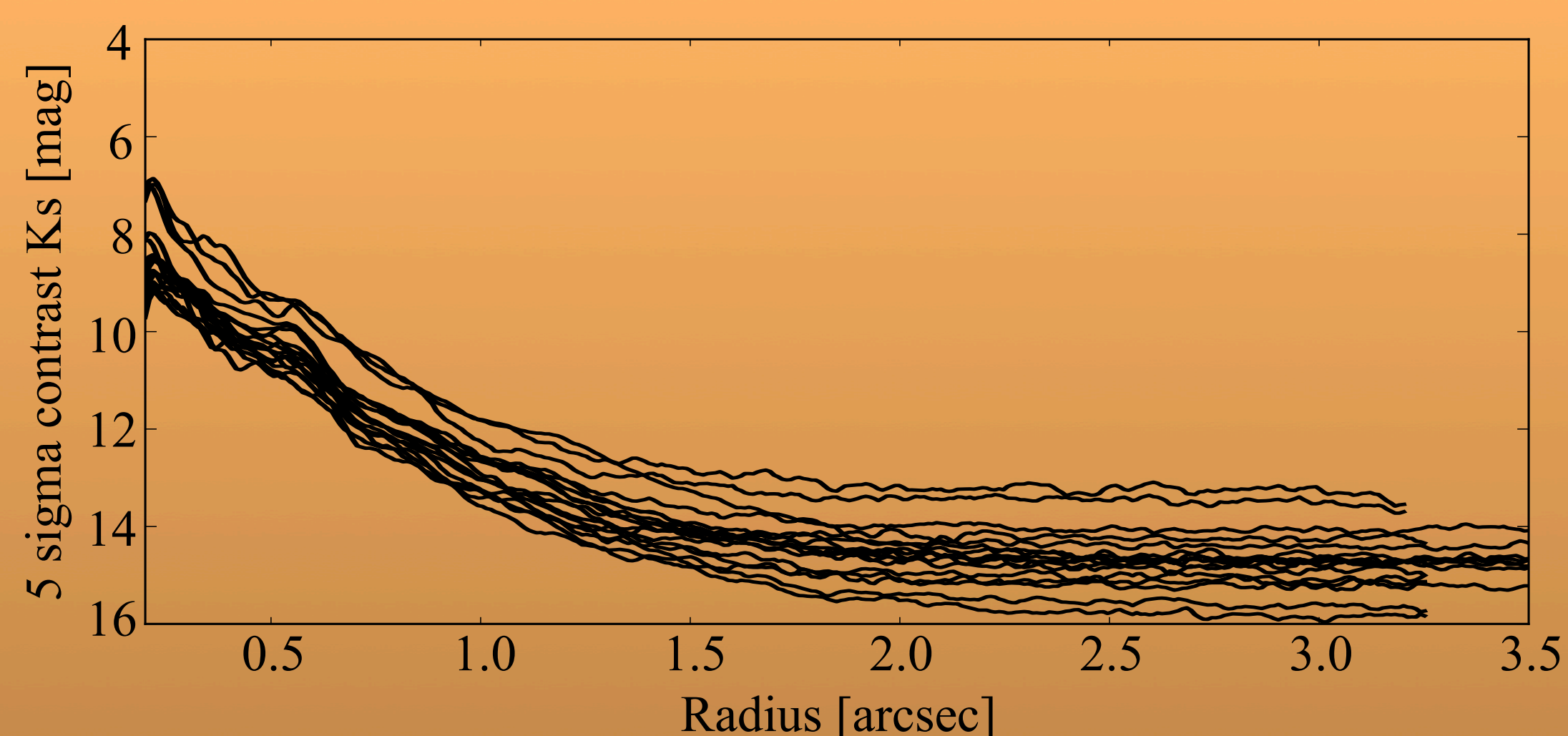
- 20 stars with Keck/NIRC2
- 16 with VLT/NACO

We then combined our data with published data:

- 57 stars with Gemini/NICI²
- 29 with VLT/NACO³
- 41 with Subaru/SEEDS⁴

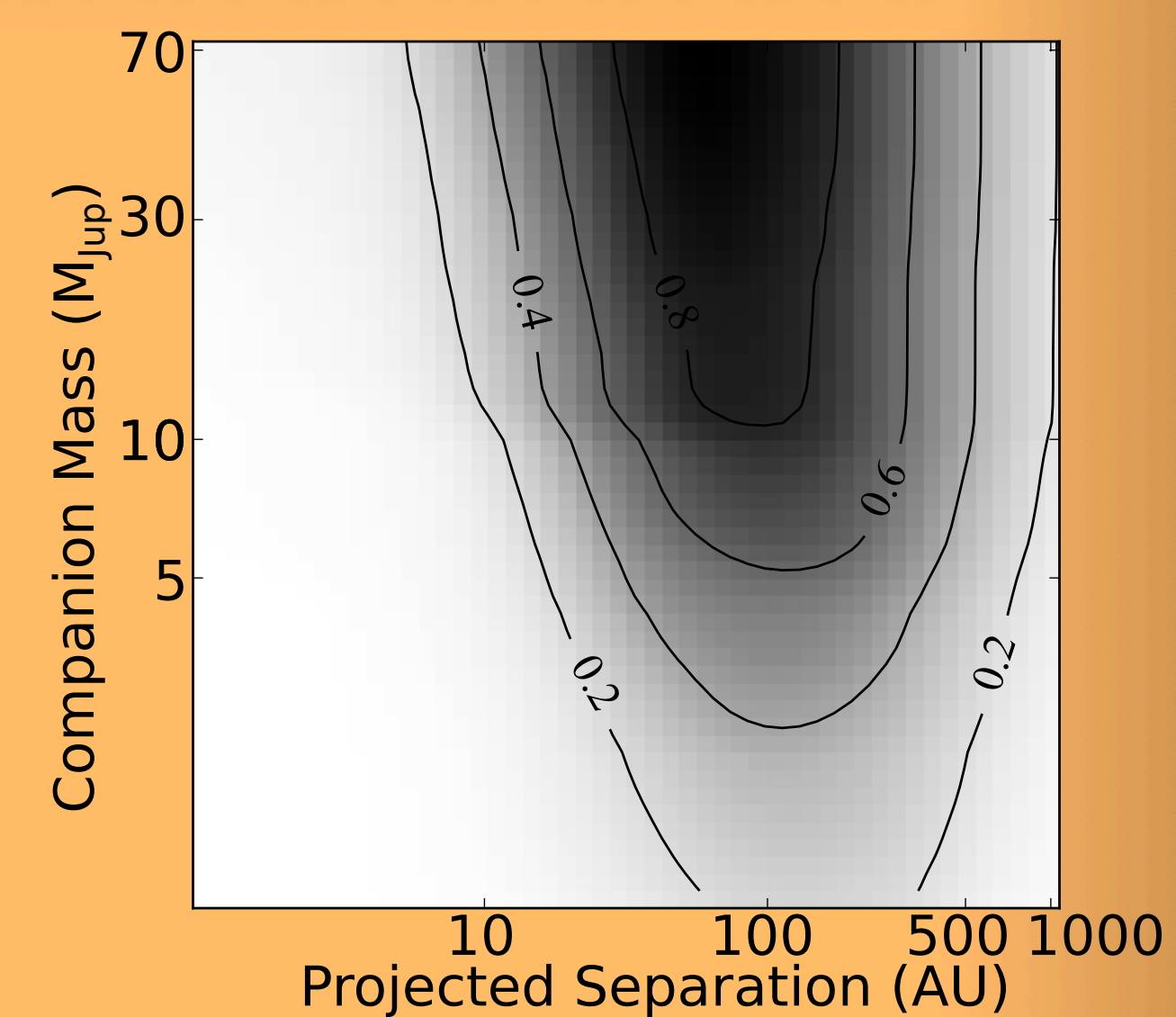
Thus, we have 127 unique targets, the largest sample of stars with debris disks to date.

We created contrast curves for all of our targets, in order to measure our sensitivity to planets around each star.



Results

We converted the contrast curves to Jupiter masses using the COND evolutionary model⁶ and create detection probability maps for each target (Fig. right shows average of the maps).



Finally, we used Monte Carlo simulations to predict the number of giant planets (1 to 13 Jupiter masses) and brown dwarfs (<70 Jupiter masses) we expect to detect around each target, using the detection probability maps and assuming a fixed planet companion mass function ($f(m,a) = Cm^{a\beta}$) extrapolated from 1 to 1000 AU.

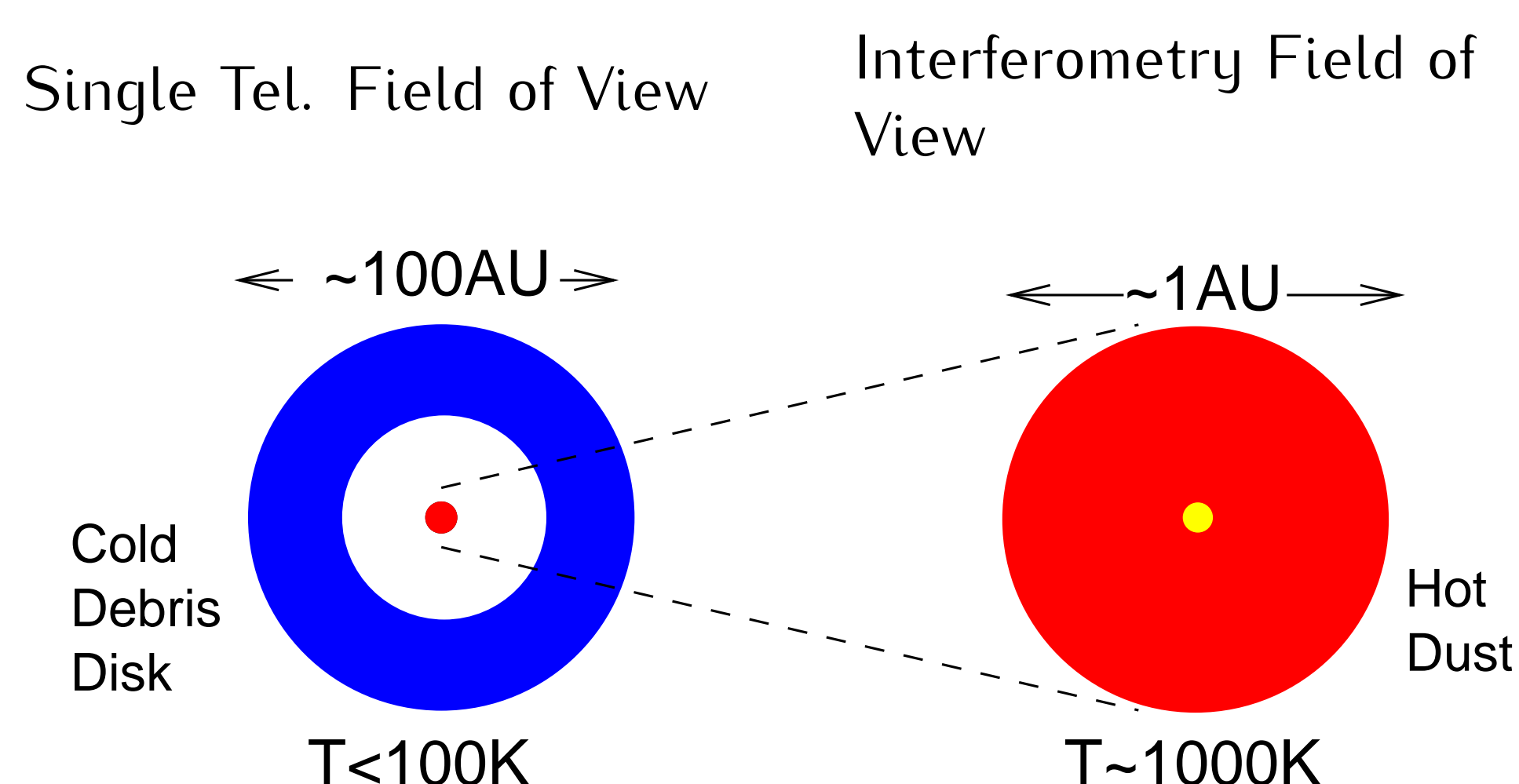
We find that the frequency of giant planets around stars with debris disk is 2.5 to 22% (68 CL), compared to 0.1 to 1.3% from the Bowler 2016 384-star meta control sample⁷.

Searching for exozodiacal light around main sequence stars with JouFLU/CHARA

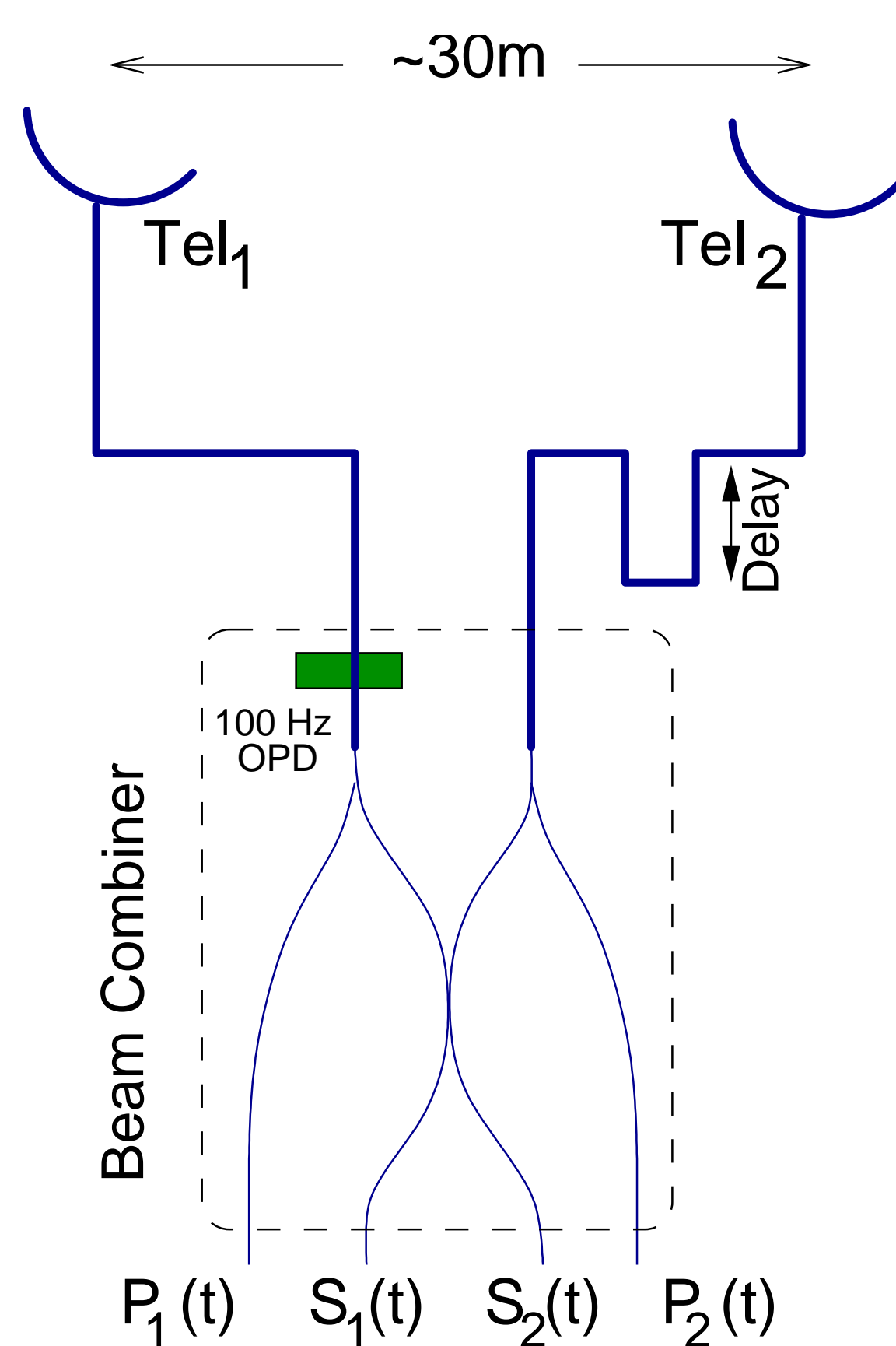
Paul D. Nuñez (3262)

B. Mennesson (3262), N. Scott, T. ten Brummelaar (GSU)

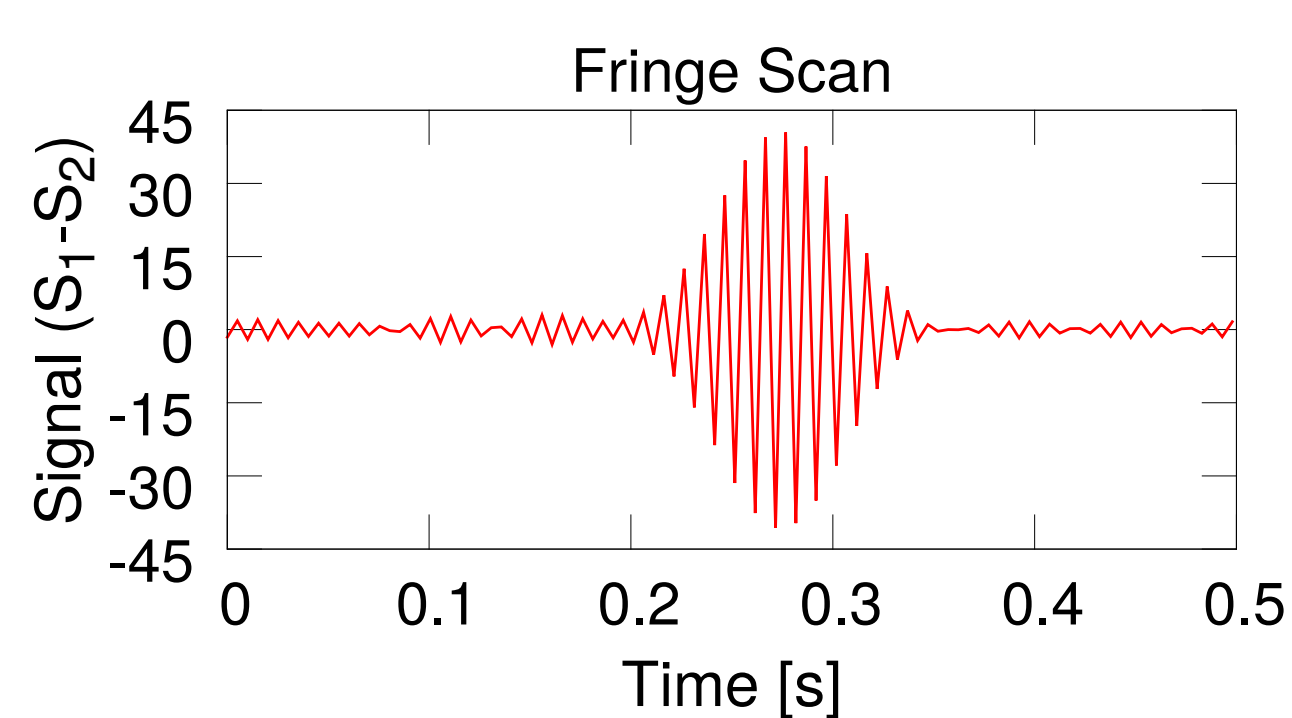
We have been measuring Exozodiacal light levels in the Near Infrared (NIR) around main sequence stars, as part of a NASA Exoplanet Research Program Grant. **NIR Circumstellar excess light within 1AU from neighboring stars most likely originates from hot dust**, which may hint at the existence of exoplanets, but also hinder exoplanet detection with future direct imaging missions.



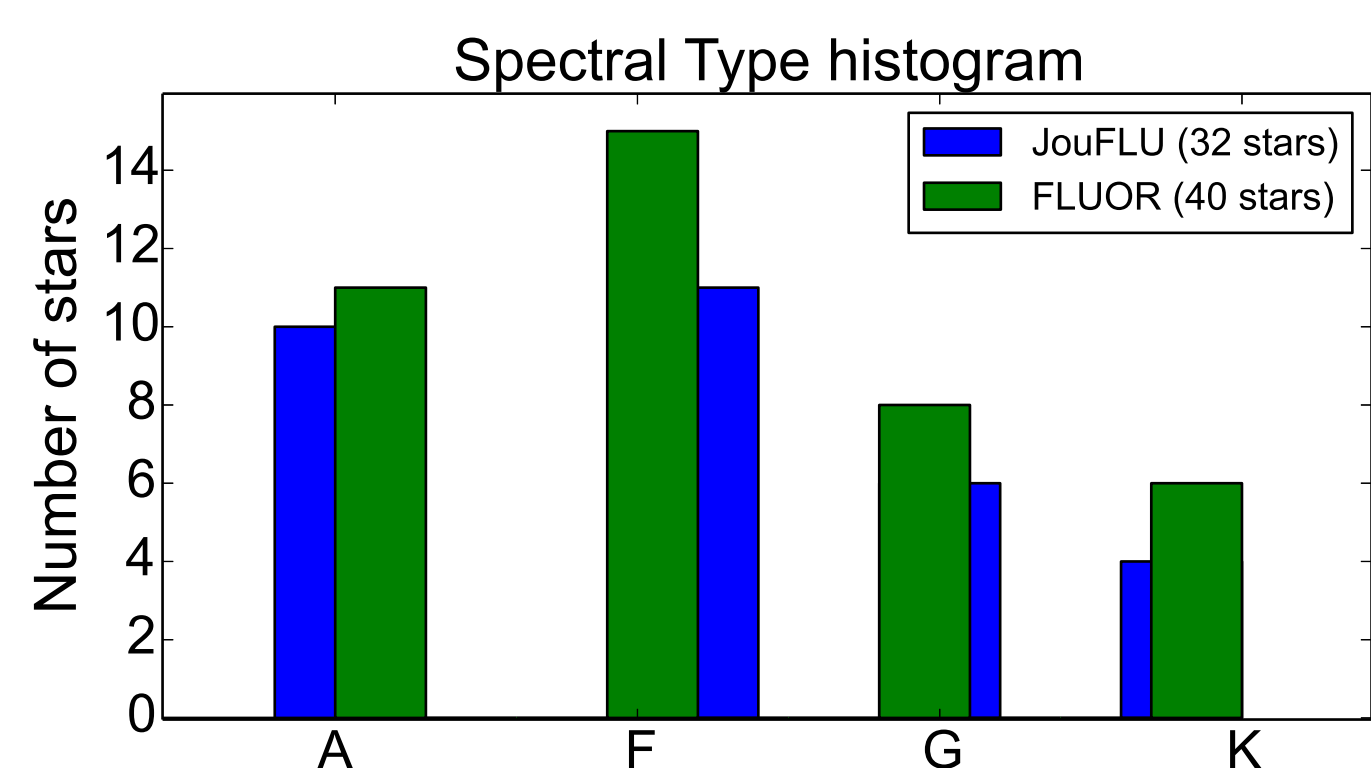
- We require very high angular resolution, attainable with optical long-baseline interferometry, which combines light between separate telescopes to form interference fringes.
- The observational signature of faint ($\sim 1\%$) circumstellar excess light is a small ($\sim 1\%$) deficit in the fringe contrast compared to a non-excess star.



We are using the Center for High Angular Resolution Astronomy (CHARA, Mt. Wilson) telescope array, along with the JouFLU fibered beam combiner, to precisely ($< 1\%$) measure the contrast of interference fringes.

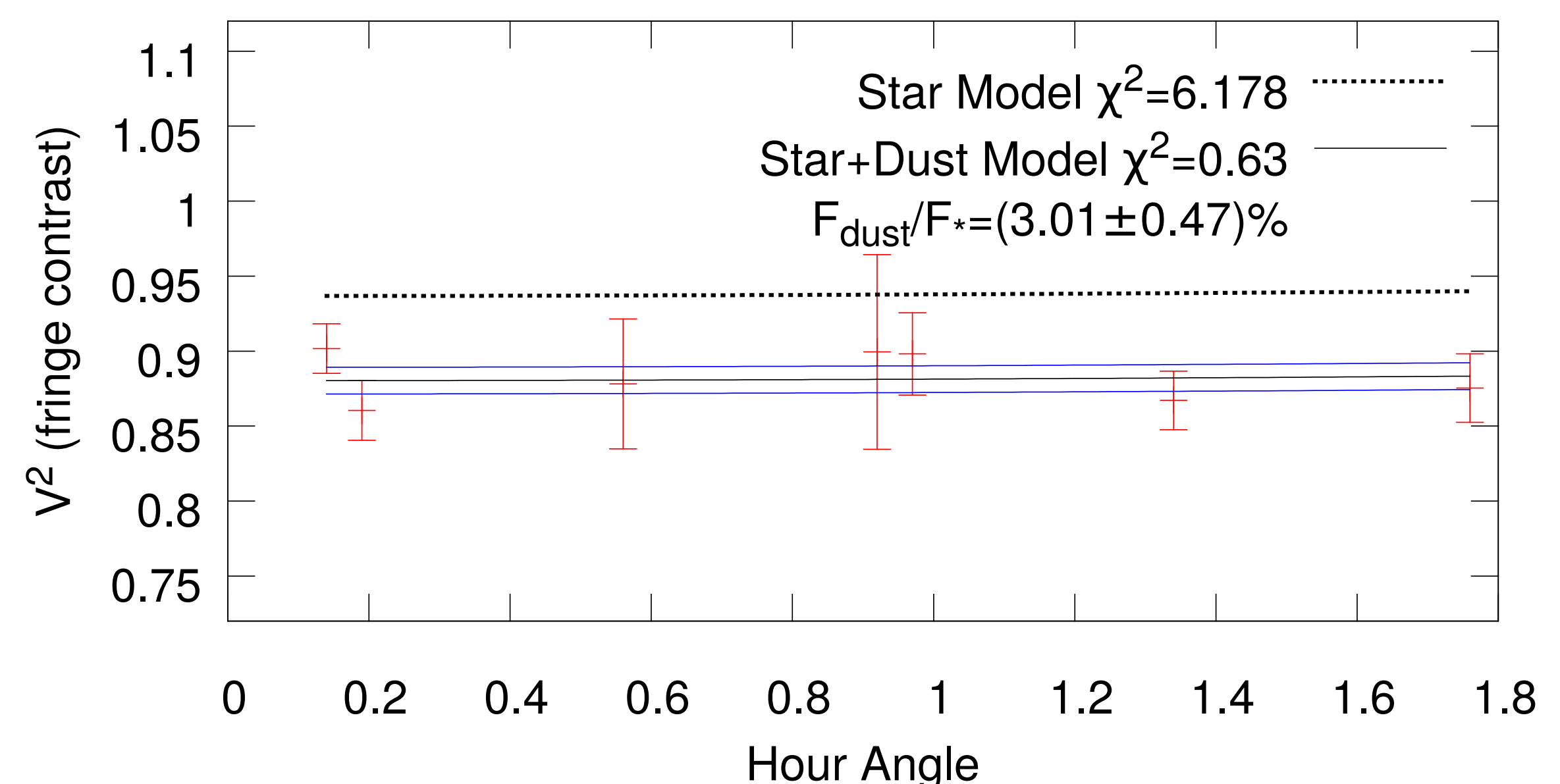


Since 2013, we have obtained data for 32 main sequence stars, which are being analyzed and combined with a previous CHARA survey of 40 stars performed by Absil et al. (2013).

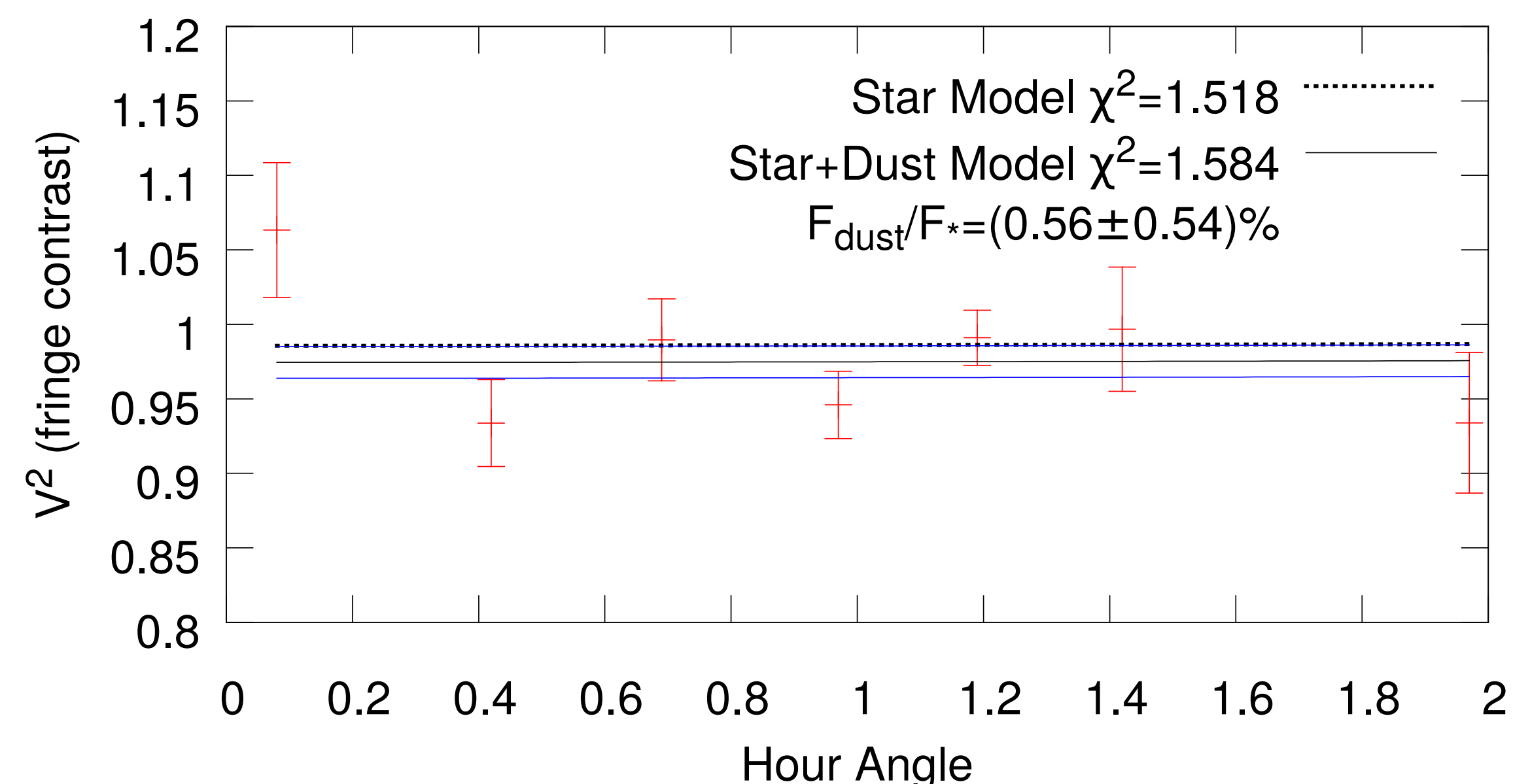


We a total of 18 circumstellar excess detections, 5 of which are new detections that were added with the survey extension.

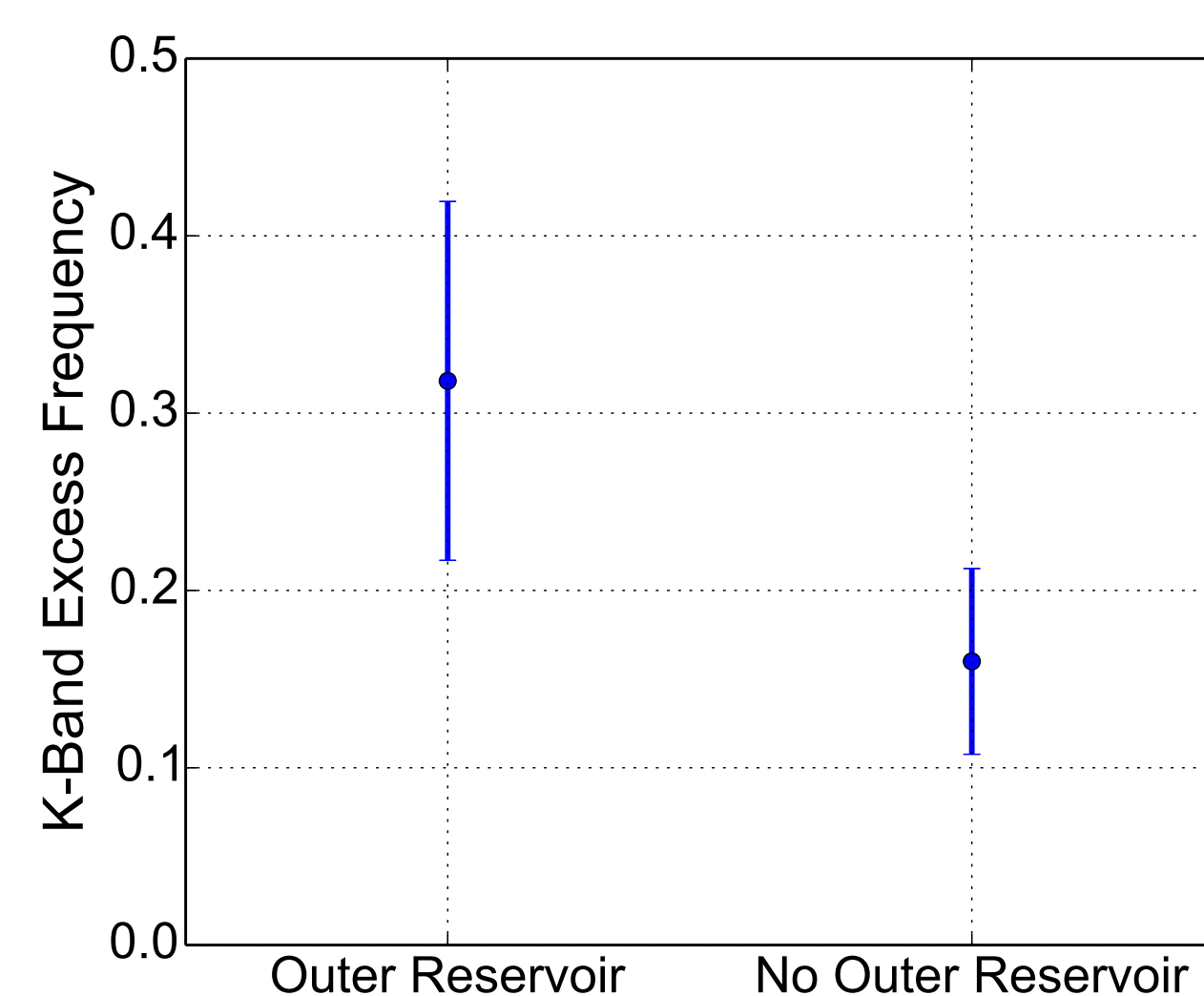
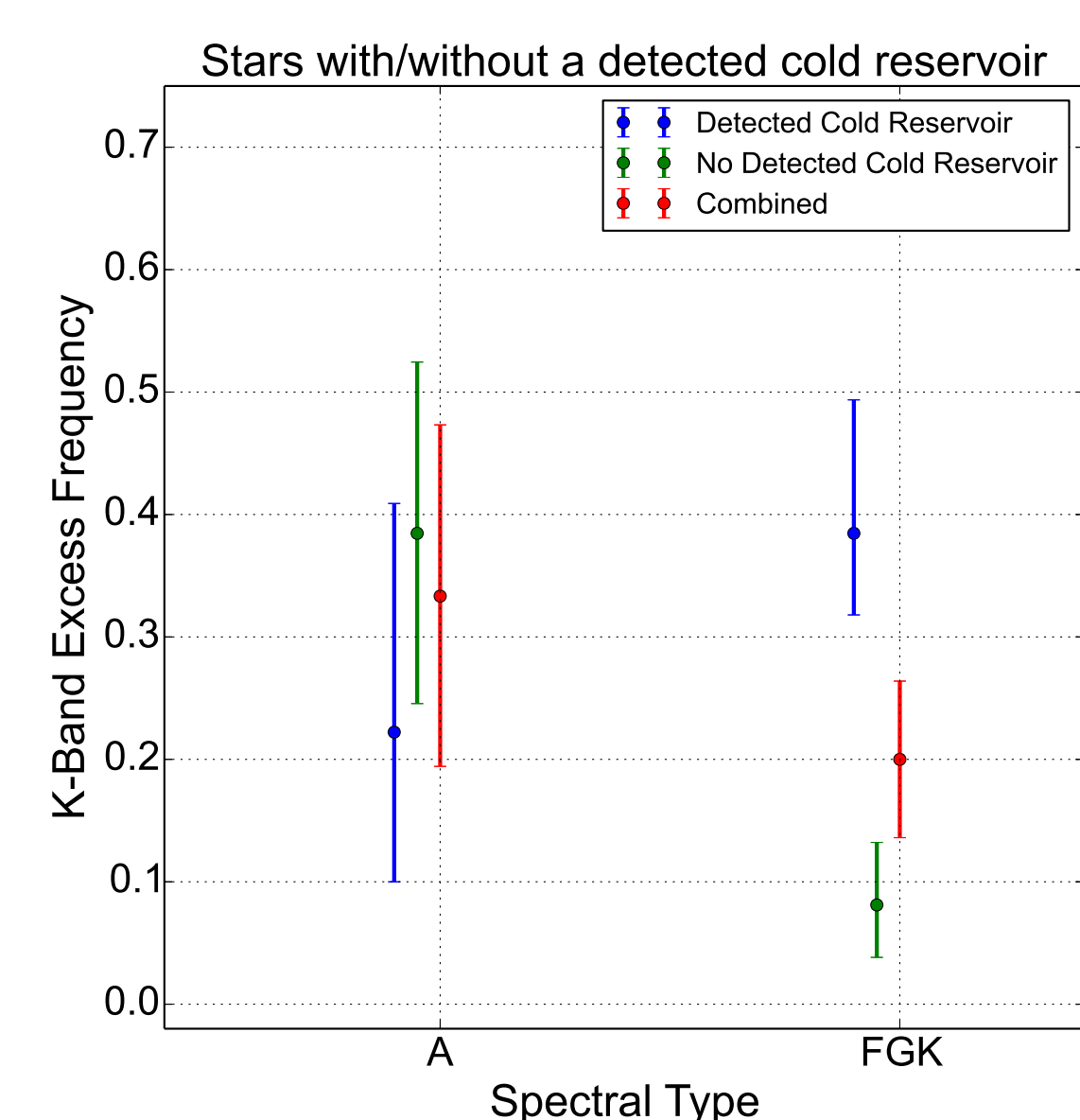
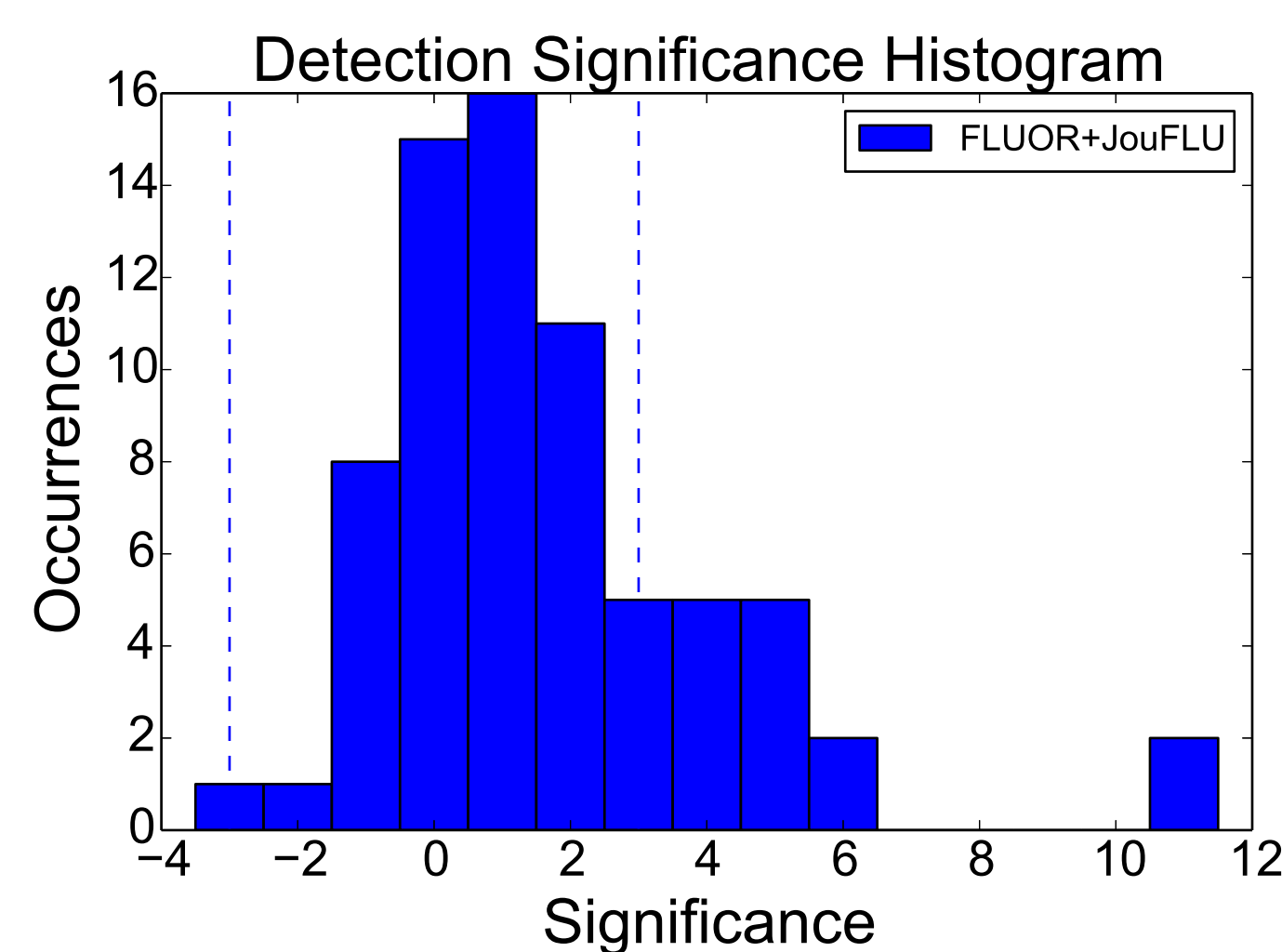
Exozodiacal Light Around Exoplanet Host-Star (HD9826)



No Exozodiacal Light Detected Around HD219134



The histogram of the detection significance is not Gaussian, but has a heavy tail beyond 3σ , indicating that our detections are not due to chance.



K-band excesses seem to occur more frequently for stars with a detected cold dust reservoir (Far-Infrared excess), but this is still not statistically significant.

A-type stars tend to have different behavior than the FGK stars: Detections without a corresponding cold reservoir tend to occur more frequently for A-type stars than FGK stars. FGK detections tend to be more frequent when they have a corresponding cold reservoir. **A preliminary conclusion is that A-type excesses are more likely attributed to exozodiacal dust formed in-situ, while FGK-type excesses may be more likely attributed to the in-fall of matter from an outer reservoir.**

Kepler beaming binaries radial velocity follow-up with WIYN/Hydra



Avi Shporer^{1,7}, Keivan Stassun², Simchon Faigler³, Tabetha Boyajian⁴, Tsevi Mazeh³, Lev Tal-Or^{3,5}, Andrej Prsa⁶
¹JPL, ²Vanderbilt University, ³Tel Aviv University, ⁴Yale University, ⁵Institut für Astrophysik Gottingen, ⁶Vilanova University, ⁷Sagan Fellow



Avi Shporer (3262)
gps.caltech.edu/~shporer

The goal of this project is to identify and confirm a large sample of *Kepler* non-eclipsing binaries, and in doing so study the performance of the BEER algorithm (Faigler & Mazeh 2011, MNRAS, 415, 3921) which is designed to identify non-eclipsing short-period binary companions using high-quality light curves (see Figures 1 and 2). The *Kepler* mission provides data for a large number of stars, which combined with BEER's sensitivity to non-eclipsing systems results in a highly efficient method to detect binary companions. The increased detection efficiency of our approach enables detecting rare objects, specifically brown dwarfs at short periods, that despite decades of transit and radial velocity (RV) surveys only a very small sample is known. Increasing the sample of known short period brown dwarfs orbiting stars across the main sequence will shed light on formation and orbital evolution of both planets and stars.

Since this approach is still in its infancy we carry out RV follow-up to confirm the nature of the system and measure the orbit. In order to be efficient in using telescope time we are using the WIYN/Hydra multi fiber spectrograph. Hydra can observe up to 90 targets simultaneously within a circular field of view with a diameter of one degree. The position of our targets is shown in Figure 3. This project is ongoing, we are currently working on deriving the RVs from all available data and obtaining the orbital solutions. Some results are shown in Figure 1.

Our goal is to obtain 10 RVs for each of our 5 fields, which is sufficient measurements to fit the 5-parameter Keplerian orbital model (the orbital period is accurately known from photometry so is fixed in the model fitting). The next phase of our project will include a search for a third stellar companion, by looking for a long-term RV trend, another set of lines in the spectra, and high angular resolution imaging of our targets.

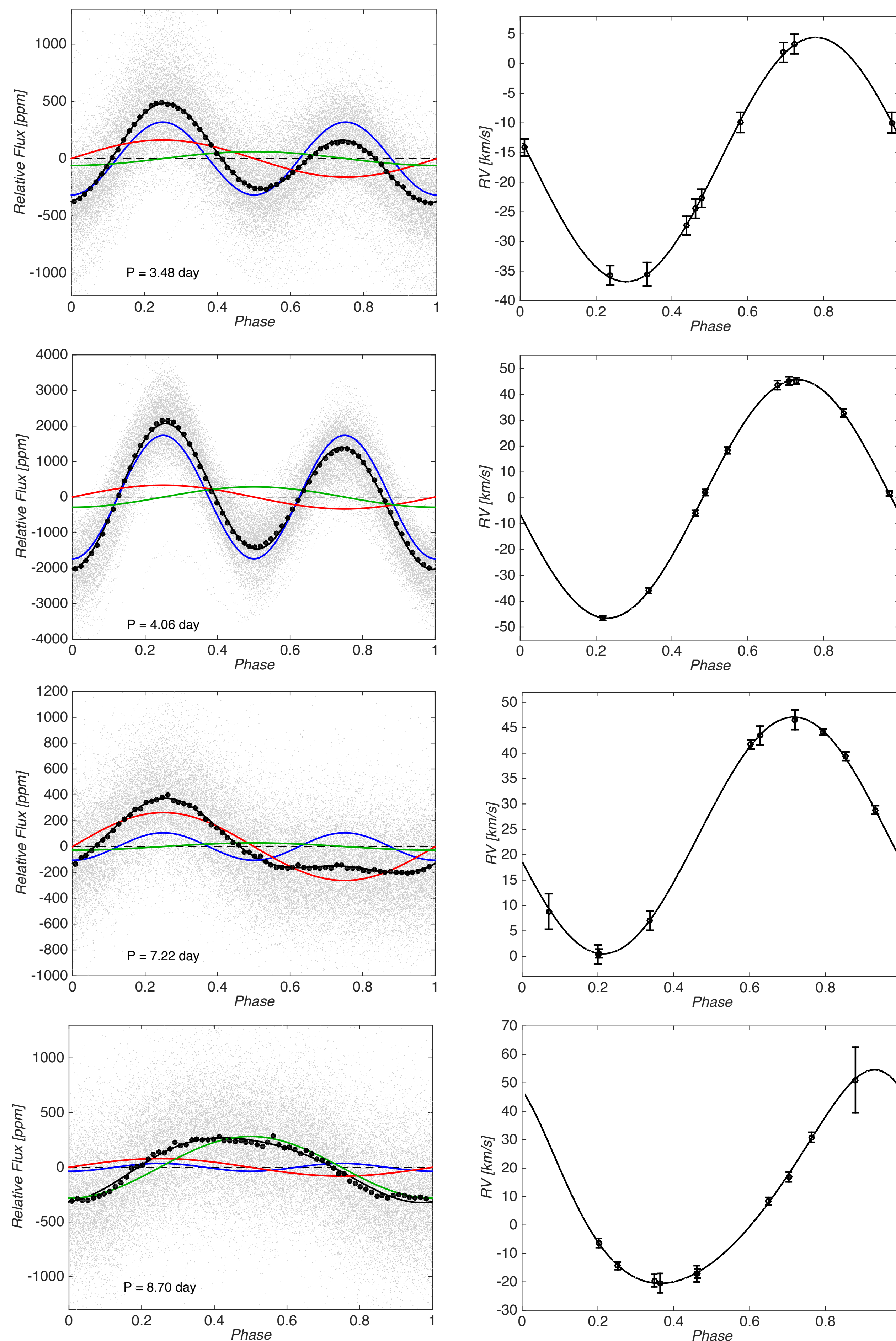
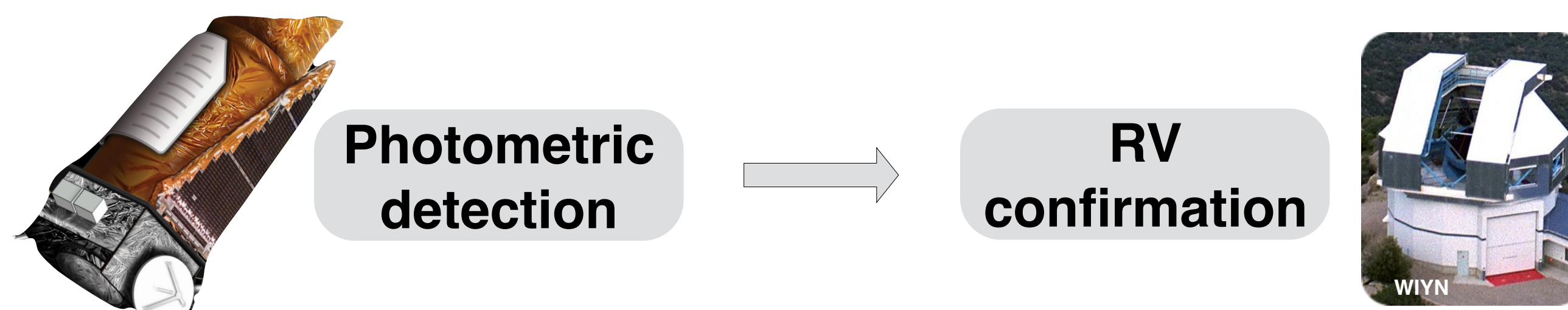


Figure 1. Four examples of a photometric detection of an orbital signal in *Kepler* light curves due to a non-eclipsing binary companion (left), and the RV confirmation obtained by WIYN/Hydra (right) folded on the same orbital period. The light curves show the phase folded *Kepler* data (gray), the binned phase curve (black circles), and the fitted model (black solid line) decomposed to the three BEER phase components, beaming (red), ellipsoidal (blue), and reflection (green). The flux zero point is marked by a dashed black line. The RV curves show the Hydra RVs, overplotted by the fitted Keplerian orbital model.

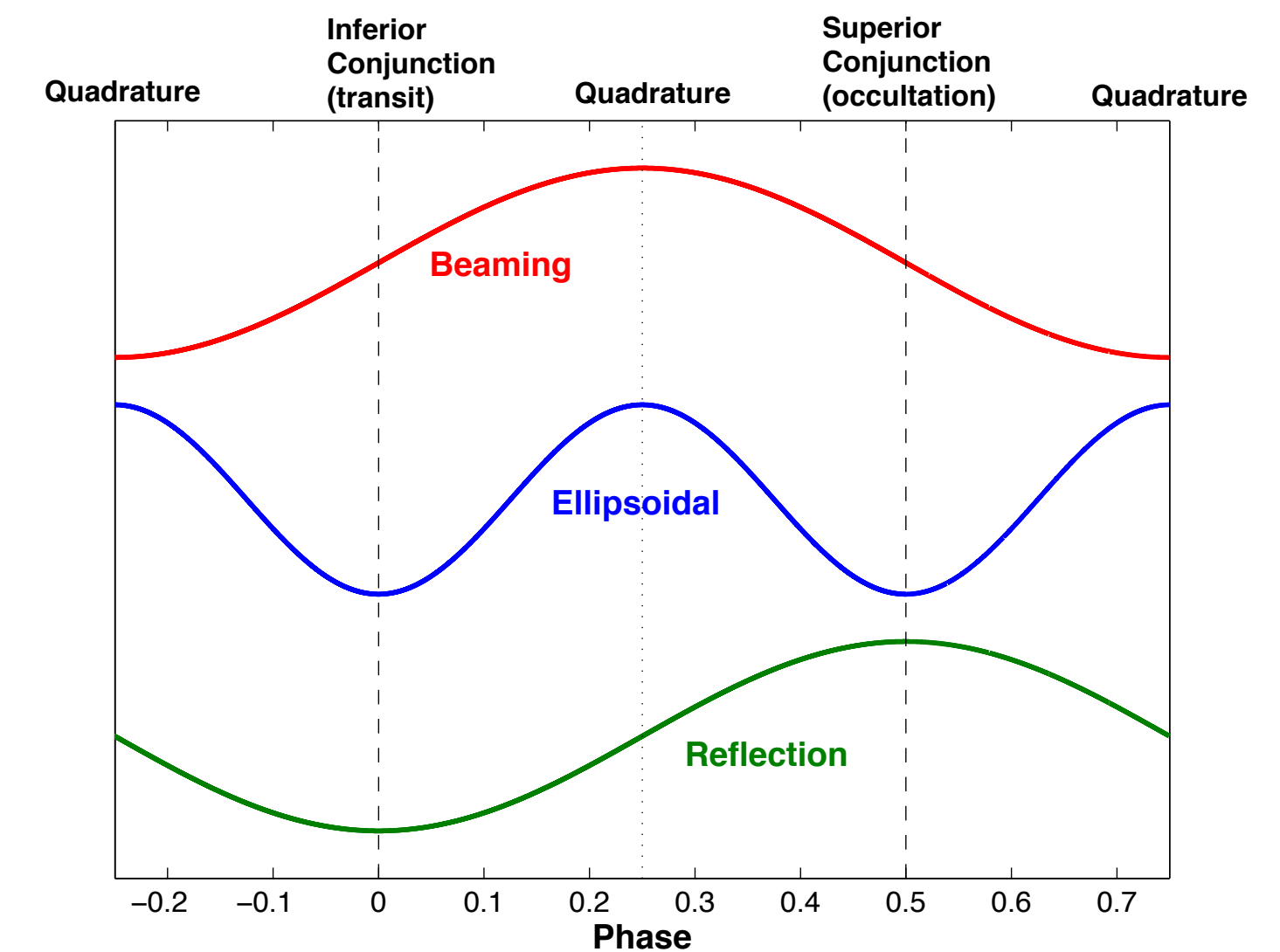


Figure 2. Schematic light curves of the three sinusoidal components of the BEER model: BEaming (red), Ellipsoidal (blue), and Reflection (green; including reflected light and thermal emission). The BEER algorithm identifies an orbital signal in the phase curve as a specific superposition of these three components, as can be seen in the left panels of Figure 1.

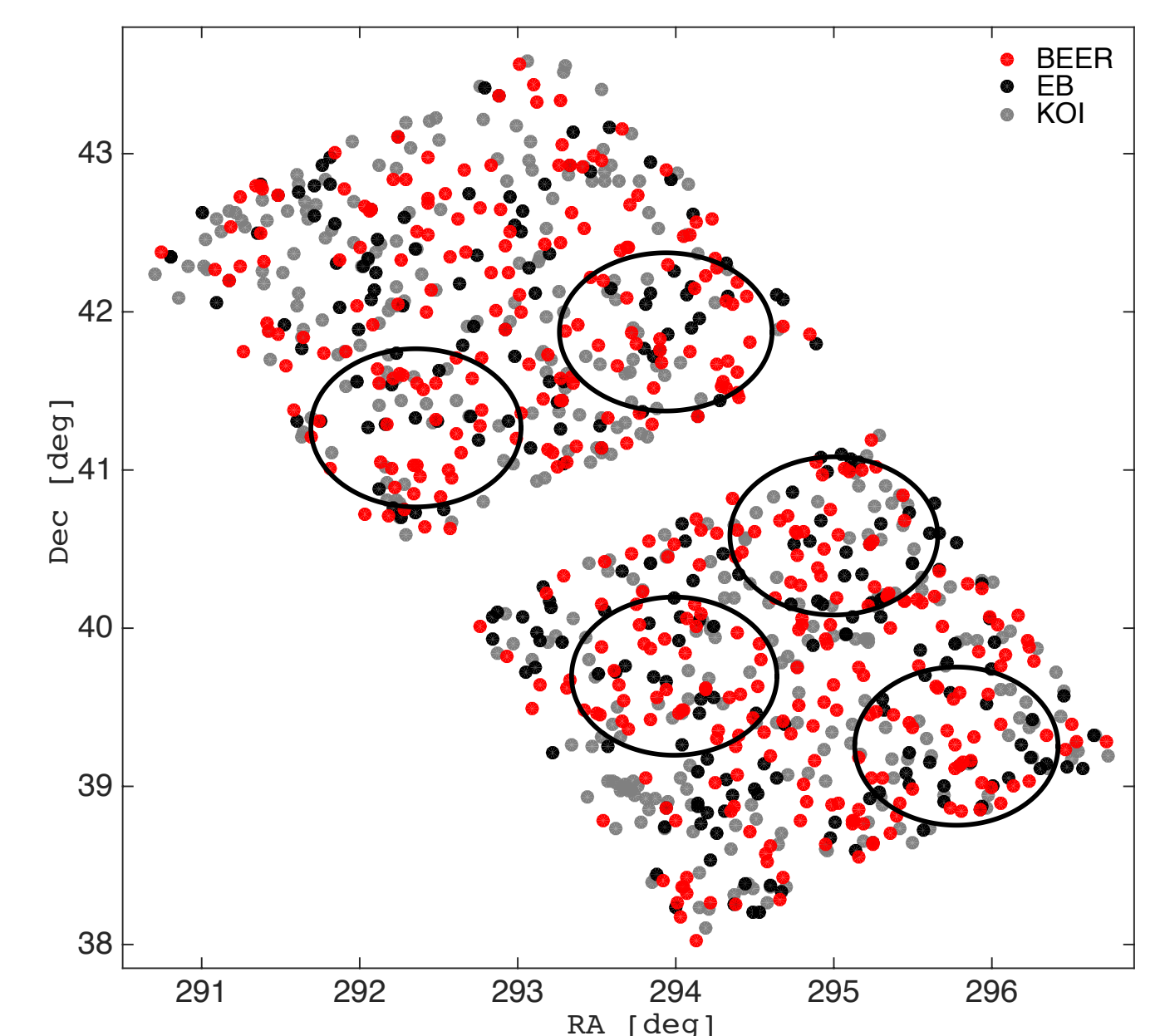


Figure 3. Positions of all beaming binary candidates (BEER; red), *Kepler* eclipsing binaries (EBs; black), and KOIs (gray), within the two *Kepler* CCDs targeted in this project. We chose those two CCDs as they are positioned in the densest region in the field. Our five Hydra circular fields (one degree diameter) are overplotted in black. The list of targets is currently confidential but can be shared by the authors upon request.

This project in numbers:

- 26 WIYN nights (+3.5 scheduled)
- 5 Hydra fields
- 247 targets total, including:
 - 131 beaming binary candidates
 - 85 EBs
 - 31 KOIs

We welcome any feedback/
 thoughts/questions:
shporer@gps.caltech.edu

Spitzer Microlens Detection of a Massive Remnant in a Well-separated Binary

Yossi Shvartzvald (3262) [Shvartzvald, et al. 2015, *ApJ*, 814, 111]

Massive remnants mass distribution: Is there a gap?

Neutron stars (NSs) and stellar black holes (BHs) are the remnants of massive stars after their core collapse. This important population in stellar evolution is poorly studied due to observational challenges, resulting in a small sample of objects. While some NSs can be detected as pulsars, most of our knowledge comes from BHs or NSs in close binary systems that emit X-ray radiation, as the massive remnant accretes matter from a stellar companion (X-ray binaries).

The observed mass distribution suggests the existence of a gap at 3-5 M_{\odot} , separating NSs from BHs. However, the statistical significance of the result is low due to the small sample. Many formation theories do not predict the existence of such a gap, while others that can reproduce this gap have difficulties explaining features of many observed core-collapse supernovae.

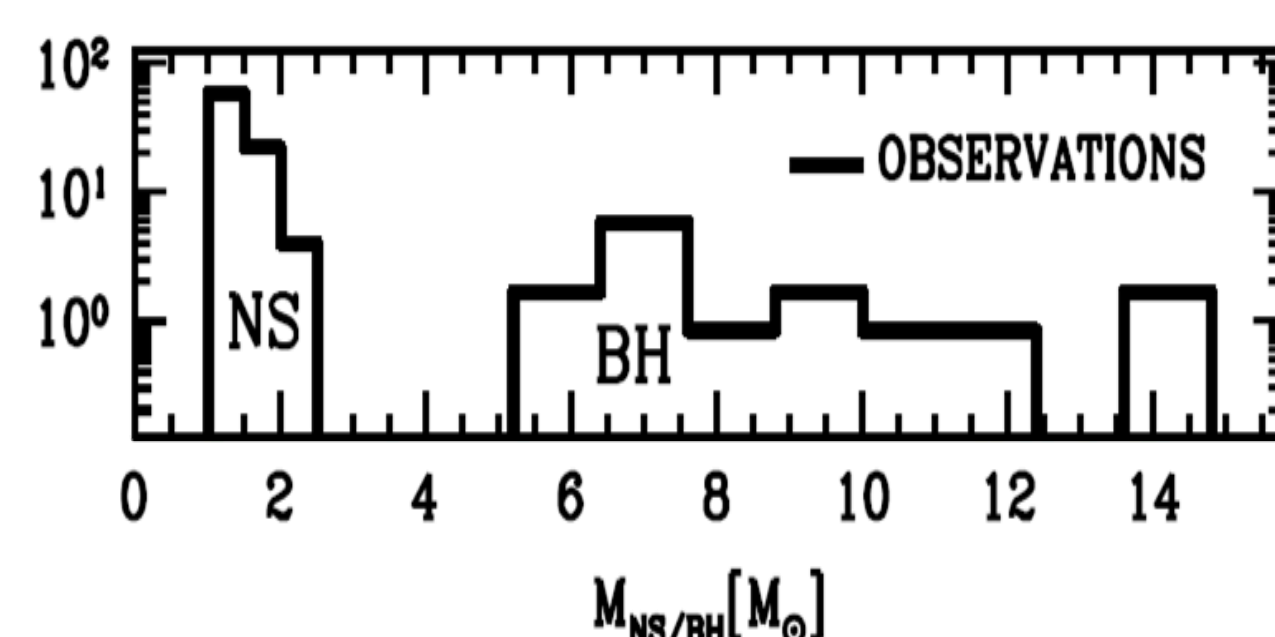
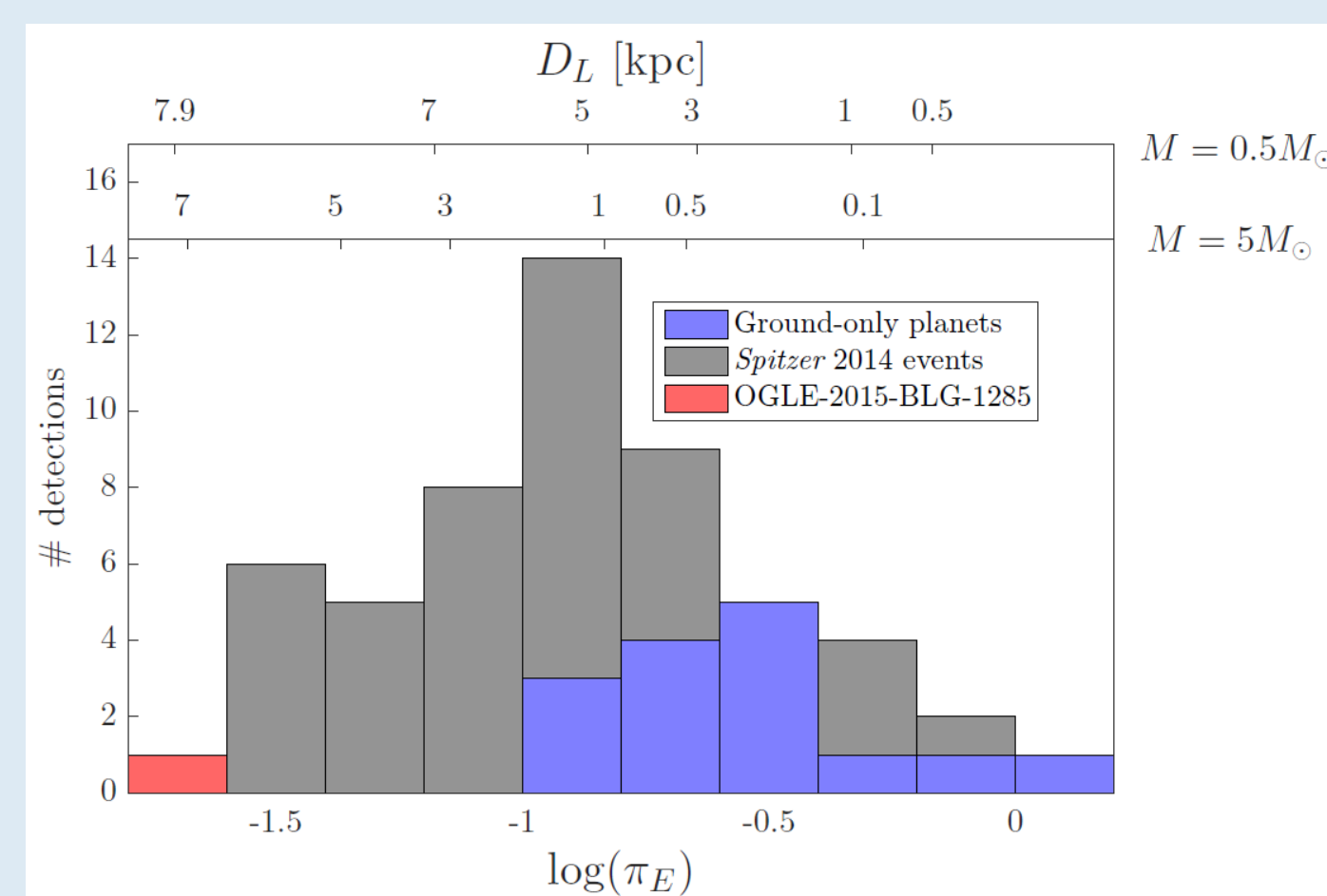


[Figure from Fryer 2013]

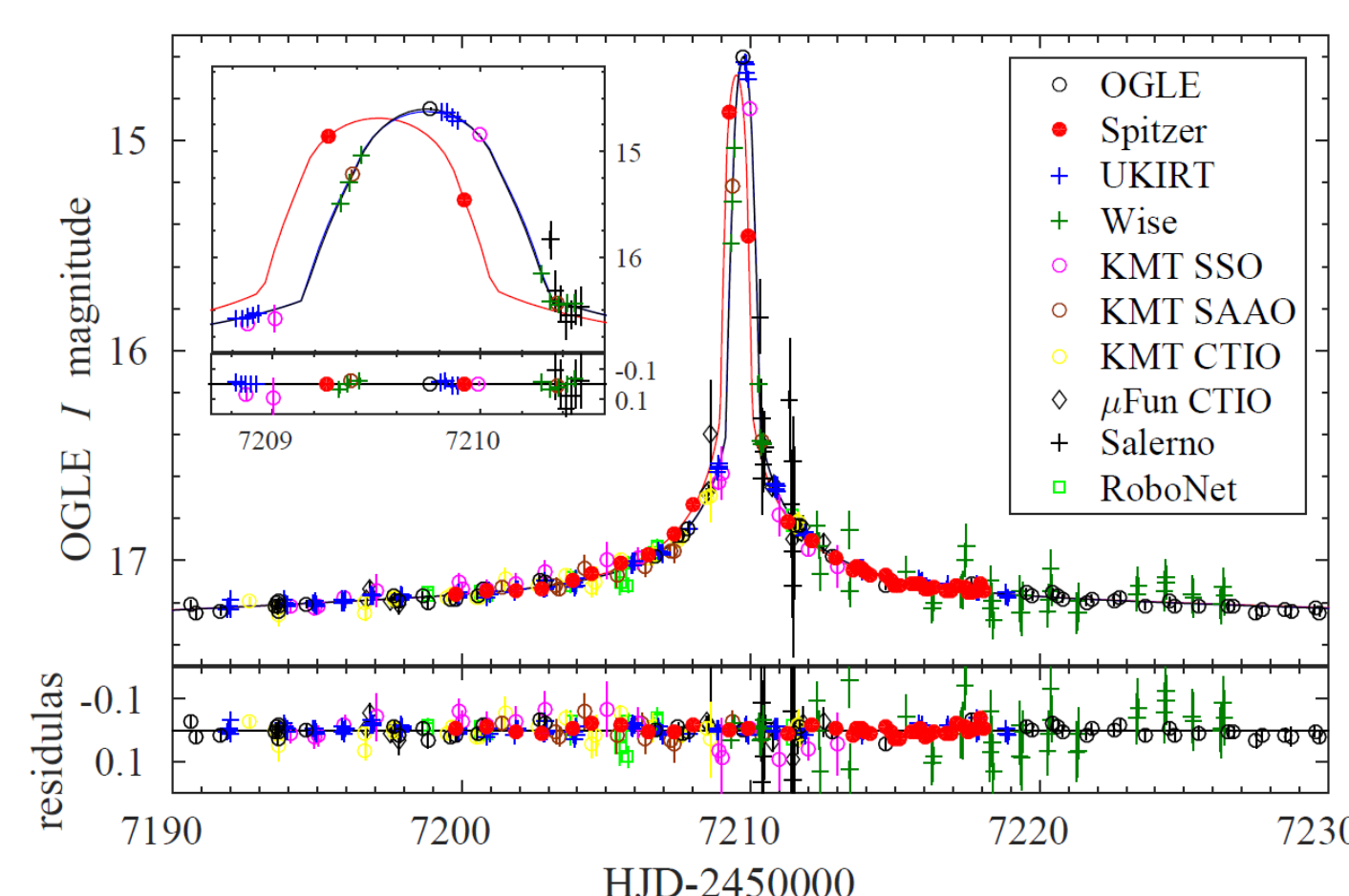
Microlensing mass measurements: Spitzer satellite-parallax revolution

Gravitational microlensing is unique in its ability to detect objects based solely on their gravitational field, and thus appears to be the only way to systematically study the populations of BHs and NSs, whether isolated or in well-separated binaries. The *Spitzer* 2014 and 2015 microlensing campaigns have revolutionized the microlensing field. The satellite observations of over 200 events that were discovered and monitored simultaneously by ground-based surveys facilitated the systematic measurement of the microlens parallax, π_E – a crucial quantity for determining the mass of the lensing system. The microlens parallax tends to be small for massive and/or distant lenses. The parallax detection from the ground, which relies on the fairly slowly accelerated motion of the Earth, is not sensitive to such small signals. Space-based microlensing directly compares contemporaneous light curves from two well-separated observers and can thus reliably measure very small parallax values.



Microlensing event OGLE-2015-BLG-1285: smallest microlens parallax ever measured

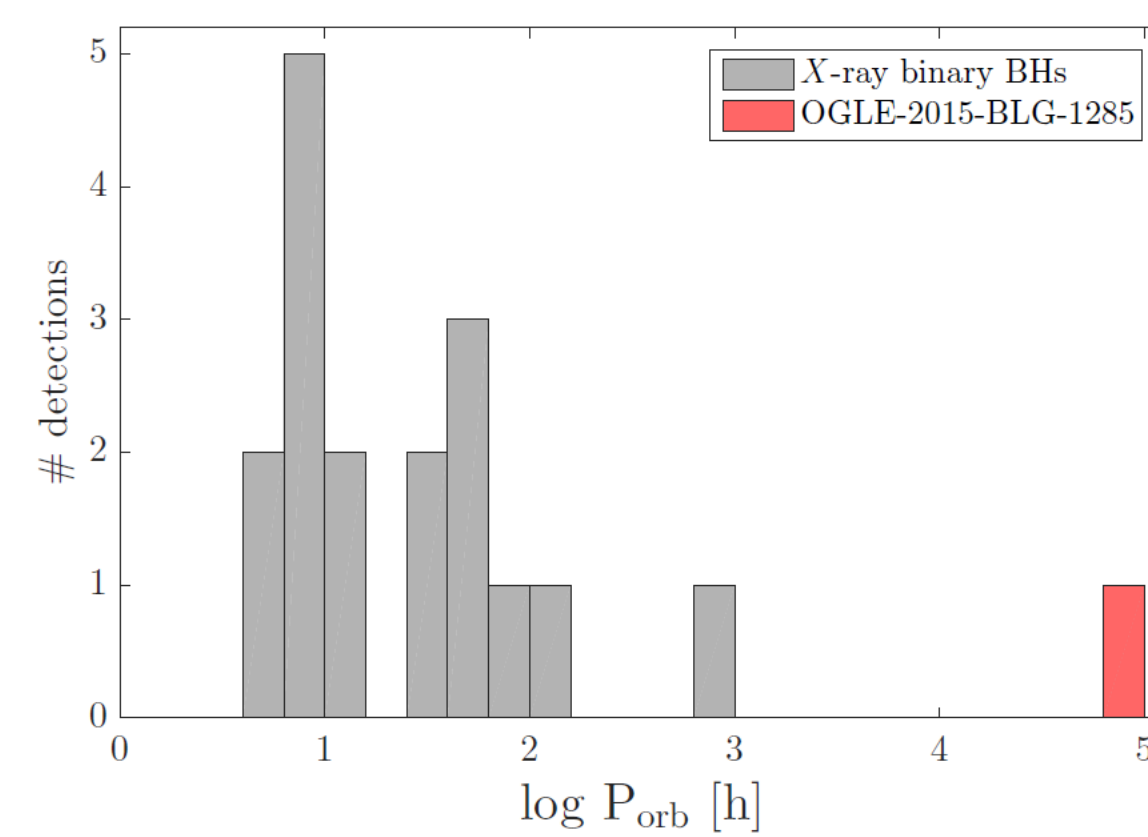
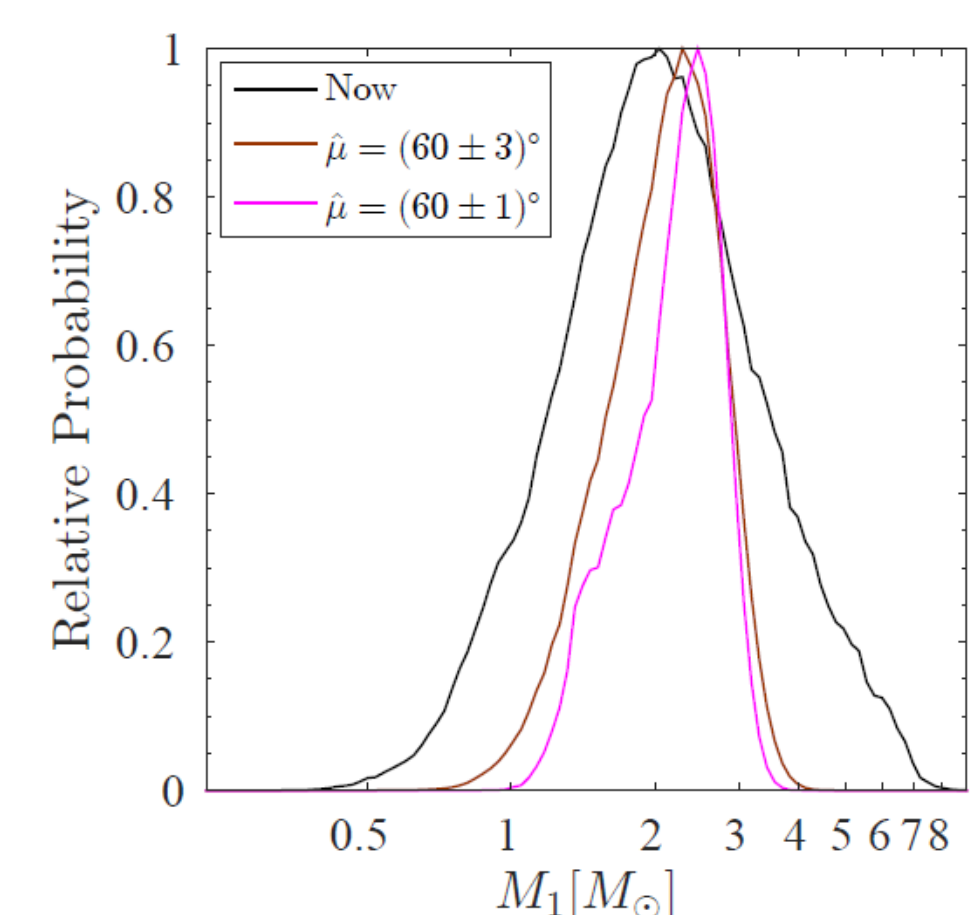
The light curve of microlensing event OGLE-2015-BLG-1285 as seen by *Spitzer* and various ground observatories. The single pronounced feature near the peak of a roughly symmetric and otherwise low-amplitude single-lens event indicates on the presence of a companion. The very small ~ 0.3 day offset between the peak seen by *Spitzer* and the ground hints that the microlens parallax is small, implying of a high-mass distant lens.



A massive remnant in a wide binary: a pathfinder for unstudied population

Parameter	Median	68% confidence intervals
$M_1 [M_{\odot}]$	2.0	[1.2,3.3]
$M_2 [M_{\odot}]$	0.8	[0.5,1.2]
$r_{\perp} [AU]$	6.1	[5.7,6.5]
$D_L [kpc]$	7.5	[7.3,7.7]

The mass of the primary component of the binary lens is $M_1 > 1.35 M_{\odot}$ (80% probability). A main-sequence (luminous) star in this mass range is ruled out by limits on blue light, meaning that a primary in this mass range must be a NS or a BH. Future adaptive optics imaging by 30m class telescopes of the companion, which is a luminous Sun-like star, will yield a much more accurate measurement of the primary mass.



The system lies in the Galactic bulge and has a projected separation $r_{\perp} = 6.1 \pm 0.4$ AU (corresponding to an orbital period of ~ 9 years). This is two orders of magnitude more distant than any known remnant in a binary system.

[Figure adjusted from Corral-Santana, et al. 2016]

Solving the mystery with future space microlensing: Spitzer, Kepler, and WFIRST

The *Spitzer* 2016 microlensing campaign and the proposed *Spitzer* 2017-2018 campaigns will enable us to enlarge the current single massive remnant detection. *Kepler* have recently completed the first space-based microlensing survey as part of Campaign 9 of its K2 mission. The *Kepler* fields were continuously monitored from the ground by a global collaboration operating over 20 telescopes in five different continents (see poster A-2 and Henderson, et al. 2016). The high cadence and simultaneous observations allow us to potentially detect additional massive remnants and make accurate mass measurements. *WFIRST* will conduct a 432-day microlensing survey toward the Galactic bulge divided equally between six 72-day seasons. *WFIRST*'s superb photometry and excellent astrometry will allow us to find and measure the mass for ~ 500 BHs and ~ 1500 NSs (both isolated and in wide binaries). Thus, *WFIRST* will fully probe the massive remnant mass distribution, and will solve the massive remnant mystery.



- 1) Fryer 2013, *Classical and Quantum Gravity*, 30, 244002
- 2) Shvartzvald, et al. 2015, *ApJ*, 814, 111
- 3) Corral-Santana, et al. 2016, *A&A*, 587, A61
- 4) Henderson, et al. 2016, arXiv:1512.09142

[Figure from the poster of the 21st microlensing conference, to be held in Pasadena in January 2017]

Stellar Activity Impacts Exoplanetary Infrared Spectra

Robert T. Zellem (3262)

Mark R. Swain (3262)

The use of the NASA insignia is governed by JPL Rules! DocID:77692. No logos may coexist with the NASA insignia except other agency sponsor logos. Do not include the JPL logo or mission logos when using this poster template.

Abstract

Stellar variability due to surface magnetic activity poses a great challenge to accurately and precisely characterizing the properties of transiting exoplanets, including their atmospheric composition, by altering the observed planetary spectrum. These effects can become especially important for the high precision measurements (<50 ppm) needed to characterize the atmospheric composition of smaller planets (e.g., $R_{\text{planet}} \leq 2R_{\text{Earth}}$).

Stellar Activity Drastically Alters an Observed Exoplanet Spectrum

Stellar variability, in the form of star spots, can affect the measured spectrum of a transiting exoplanet and its retrieved physical properties (Fig. 1; Pont et al. 2008; Agol et al. 2010; Carter et al. 2011; Desert et al. 2011; Sing et al. 2011; Ballerini et al. 2012; McCullough et al. 2014; Oshagh et al. 2014; Damasso et al. 2015; Zellem et al. 2015). For example, spots can cause an underestimation of the planetary radius up to 10% (Oshagh et al. 2014). For the hot Jupiter HD 189733b, its near-IR slope in its primary transit spectrum, previously interpreted as Rayleigh scattering by haze particles (Pont et al. 2008, 2013; Sing et al. 2011, 2016), can also be caused by unocculted star spots on its active K0 host star (Boisse et al. 2009; McCullough et al. 2014). Taking into account unocculted star spots is especially important for current Hubble/WFC3 observations where we estimate they can change the planetary spectrum up to 6σ per spectral bin. For JWST, this effect is even more pronounced, up to 25σ per spectral bin, due to its increased precision and wavelength coverage over Hubble. **Thus if one does not account for spots then an atmospheric radiative transfer analysis will retrieve the incorrect physical properties of the exoplanet, impacting parameters such as molecular abundances, thermal profile, or the existence of clouds or hazes.**

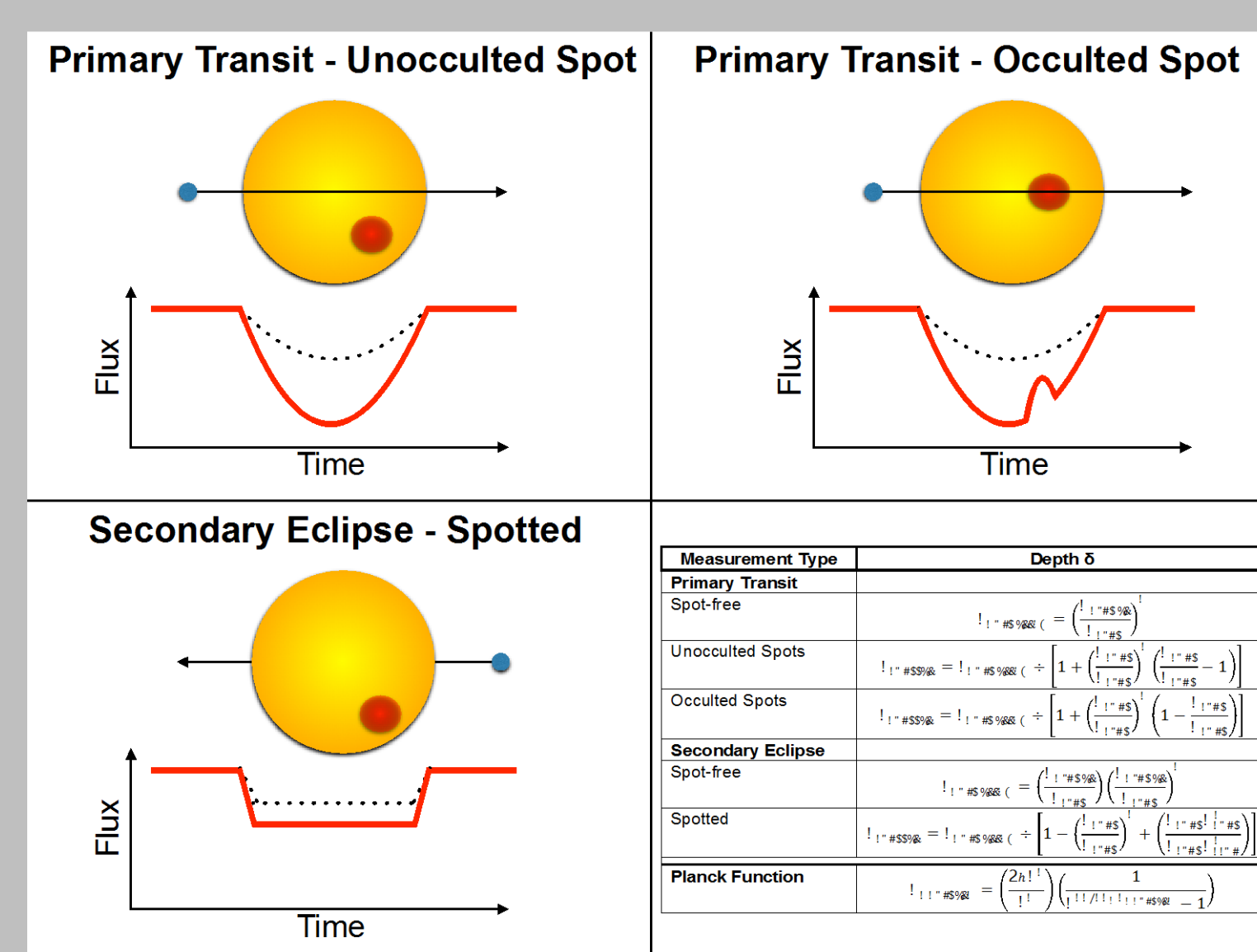


Figure 1: Effect of Star Spots on a Transit Lightcurve. *Top Left:* Unocculted spots cause the primary transit depth to deepen at visible wavelengths (red line) vs. the unspotted case (dotted black line). *Top Right:* Occulted spots overall cause the primary transit depth to deepen at visible wavelengths, but when the planet crosses the spot, the transit depth temporarily decreases (bump). *Bottom Left:* During secondary eclipse, a spotted star looks darker, resulting in a deeper eclipse depth at visible wavelengths. *Bottom Right:* The mathematical equations describing how a transit depth δ changes due to star spots (Berta et al. 2011; McCullough et al. 2014; Pont et al. 2008, 2013; Sing et al. 2011; and this study).

An Example Variable System

For objects with multiple Hubble visits, we can stack and order the spectra in time to visually determine how much the host star's spectrum has changed visit-to-visit (Fig. 3). Our preliminary analysis of Hubble/WFC3 observations of a transiting hot Jupiter indicates that its G0 host star is active at the $\sim 2\%$ level over the WFC3 G141 passband. Presenting the data in this way shows how the stellar spectrum changes between Visit 1 and Visits 2 and 3. This change also extends into the in-transit portion of the data, which probes the atmosphere of the exoplanet, suggesting that this **stellar variability may also influence the observed spectrum of the planet.**

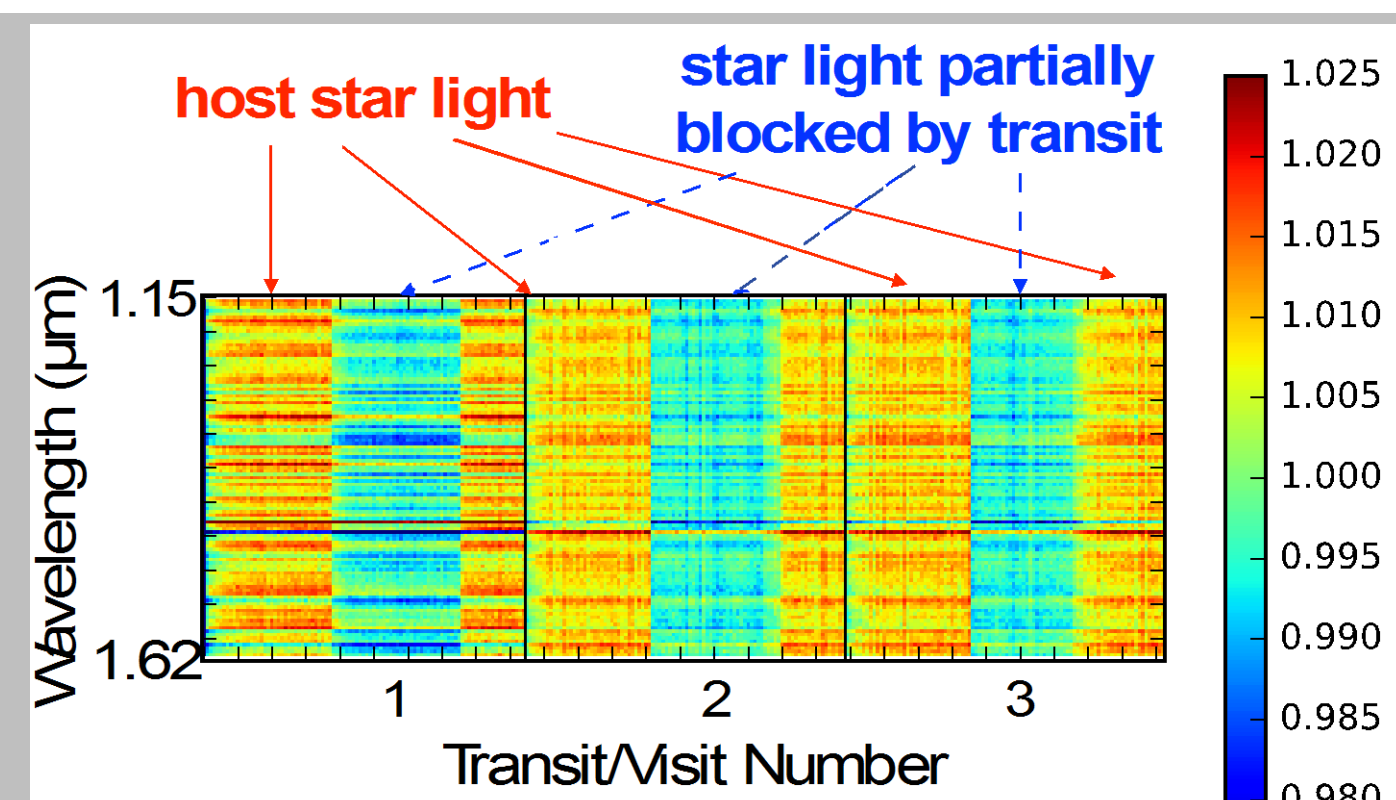
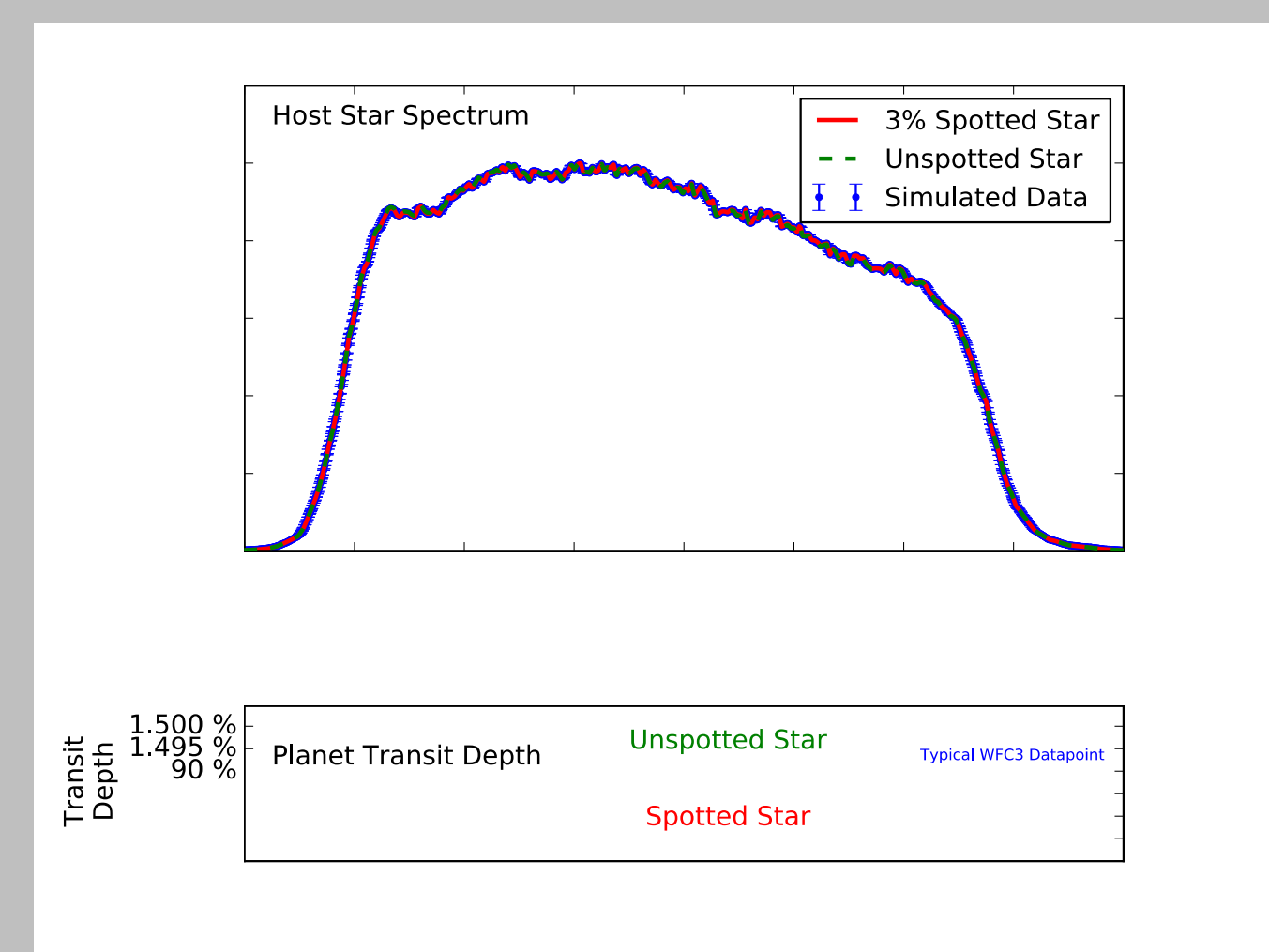


Figure 2: An Exoplanet Host Star with Significant Variability. A time-wavelength image of this exoplanet host star made by normalizing its Hubble/WFC3 spectrum at each integration by the global mean. The wavelength structure shows the parent star changing $\sim 2\%$ between visits, which we estimate is due to 10% spot coverage with an average spot temperature 300 K cooler than the stellar photosphere. These data are accumulated in the near-IR during primary transit, when self-emission from the planet is negligible and the SNR ≈ 2000 per spectral channel.

Unocculted Spots Impact Hubble/WFC3 Spectroscopy

We estimate that **this exoplanet's Hubble/WFC3 spectrum is highly impacted by unocculted spots.** We explore the effects of the star's unocculted spots on the planet's spectrum by first simulating the spotted and unspotted spectra of the host star with PHOENIX stellar models (Husser et al. 2013; Fig. 5). For the planet's spotted spectrum, we adopt a 3% spot coverage and an average spot temperature 300 K cooler than the stellar photosphere. We estimate that the exoplanet's transit depth, and hence its spectrum, is altered by ~ 300 ppm. This change is very significant as it is up to $6\times$ larger than the reported average uncertainties in a recent Hubble/WFC3 transiting exoplanet program (Kreidberg et al. 2015). **In the case of our simulation, unocculted star spots change the planet's spectrum from completely flat, indicating clouds, to one with a Rayleigh slope from photochemical haze particles.** In cool stars, spots can also introduce false detections of molecular signatures (Kreidberg et al. 2014a). For example if a spot is cool enough (≤ 3000 K), it can have H_2O and introduce a false planetary H_2O signature (Fraigne et al. 2014). **Thus unocculted star spots can drastically alter an exoplanet's spectrum, causing its physical parameters to be retrieved incorrectly.**

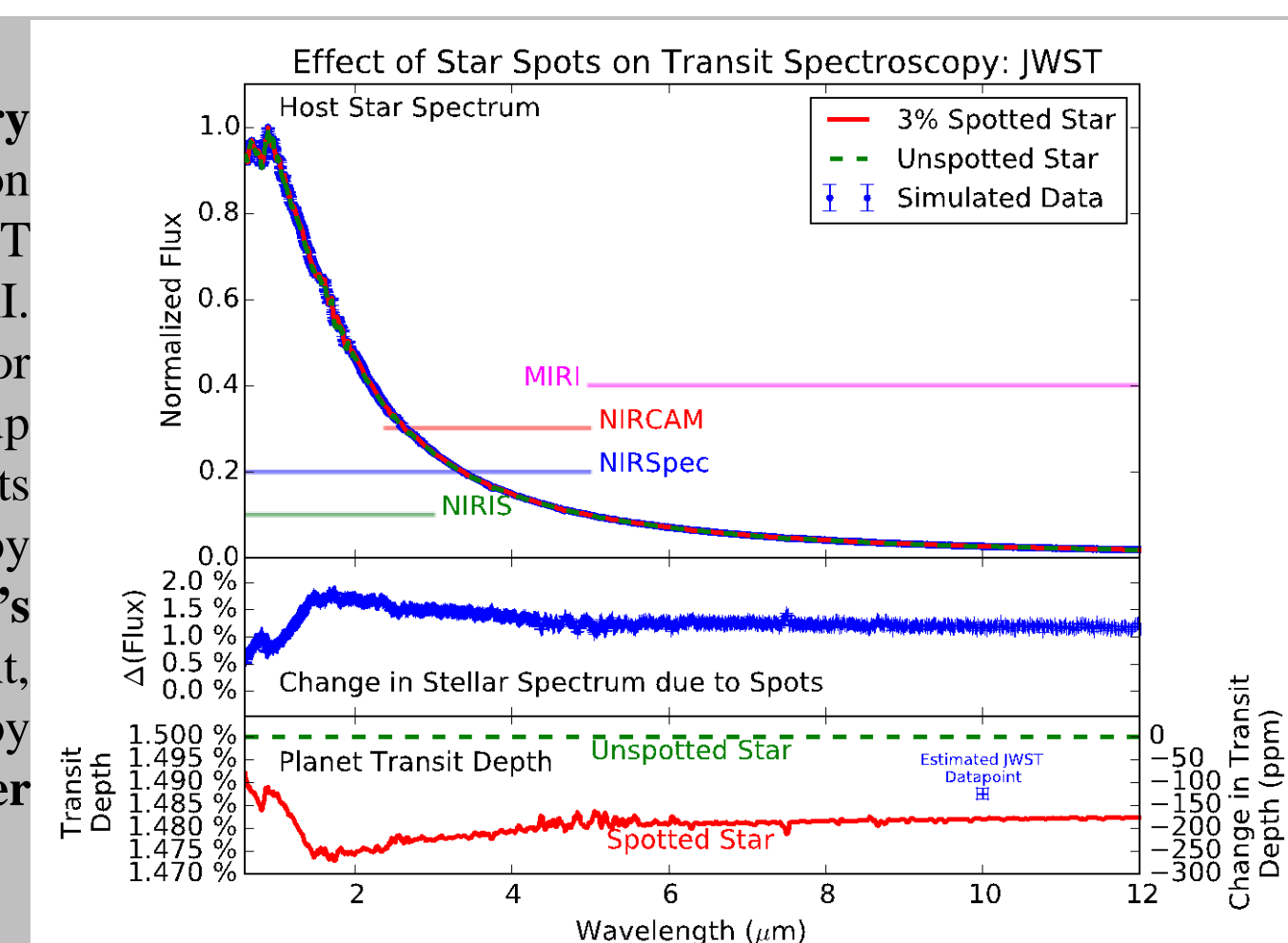
Figure 3: Effect of Star Spots on Hubble/WFC3 Exoplanetary Spectra. *Top Panel:* PHOENIX stellar models (Husser et al. 2013) of a G0 exoplanet host star without spots (green dashed line) and with $\sim 3\%$ spot coverage and an average spot temperature 300 K less than the stellar photosphere (red line; blue dots are simulated with typical Hubble/WFC3 precision). *Middle Panel:* The change in the stellar spectrum due to spots is $\sim 1\%$. *Bottom Panel:* This change in the stellar spectrum alters the exoplanetary spectrum by at least 100 ppm and up to ~ 300 ppm. We simulate both a flat planetary spectrum due to clouds with an unspotted stellar host (green dashed line) and the same cloudy planet but with a star with the same spot properties as in the top panel (red line). Spots both decrease the transit depth and introduce new spectral structure, resembling Rayleigh scattering due to haze particles (e.g., McCullough et al. 2014). Thus spots can cause an exoplanet's spectrum to be misinterpreted. **This change in the planet's spectrum is significant: $\leq 6\times$ larger than a typical Hubble/WFC3 measurement** (shown on right side).



Unocculted Spots Impact JWST Spectroscopy

Our simulation indicates that **it is necessary to correct for any exoplanet spectrum with an active star. This need is even more crucial for JWST observations (Fig. 6).** We estimate that most wavelengths will see at least a ~ 175 ppm decrease in the planet's spectrum, $15\times$ larger than JWST's estimated precision. Near-IR wavelengths in particular, where NIRIS and NIRSpec will operate, will see a ~ 300 ppm change in the planetary spectrum, $25\times$ larger than JWST's photon-limited precision. This effect will be even more exacerbated when multiple datasets from different epochs are combined together (Barstow et al. 2015). For example measuring an exoplanet's complete IR spectrum from $0.6\text{--}28.3$ μm would require both NIRSpec and MIRI observations taken at different epochs, potentially separated by days due to scheduling constraints. However, the star could change considerably between these two observations, as we find in Fig. 4, making it difficult to combine and simultaneously analyze the data.

Figure 4: Effect of Star Spots on JWST Exoplanetary Spectra. *Top Panel:* Same as Figure 3, except this simulation is done over the wavelength ranges pertinent to JWST spectroscopy with NIRIS, NIRSpec, NIRCAM, and MIRI. (N.B., MIRI extends to 28.3 μm ; range truncated here for clarity.) *Middle Panel:* Spots can alter the stellar spectrum up to $\sim 1.5\%$ across JWST's entire bandpass. *Bottom Panel:* Spots on the stellar primary can change the exoplanet's spectrum by ~ 300 ppm. **This change is extremely significant as JWST's estimated precision (12 ppm; see sample datapoint on right, estimated by scaling the Hubble/WFC3 uncertainty in Fig. 3 by JWST's increased mirror size and duty cycle) is $\leq 25\times$ smaller than the change in the exoplanetary spectrum.**



Conclusions

Stellar activity can alter the observed spectrum of a transiting exoplanet. If left untreated, it can also change the radiative transfer fit and subsequent interpretation of the planet's atmospheric properties, such as its molecular abundances and existence of hazes.

References

- Agol, E., et al. 2010, ApJ, 721, 1861
Ballerini, P., et al. 2012, A&A, 539, A140
Barstow, J. K., et al. 2015, MNRAS, 448, 2546
Berta, Z. K., et al. 2011, ApJ, 736, 12
Boisse, I., et al. 2009, A&A, 495, 959
Carter, J. A., et al. 2011, ApJ, 730, 82
Damasso, M., et al. 2015, A&A, 575, A111
Desert, J.-M., et al. 2011, ApJS, 197, 14
Fraigne, J., et al. 2014, A&A, 568, A99
Husser, T.-O., et al. 2013, MNRAS, 385, 109
A&A, 553, A6
Kreidberg, L., et al. 2014a, Nature, 505, 69
—, 2015, Sing, D. K., et al. 2011, MNRAS, 416, 1443
—, 2016, Nature, 529, 59
Zellem, R. T., et al. 2015, ApJ, 810, 11

The Inner Rim in Protoplanetary Disks

The Formation Environments of Hot Exoplanets

Author: Mario Flock (326) and Neal Turner (326)

Motivation:

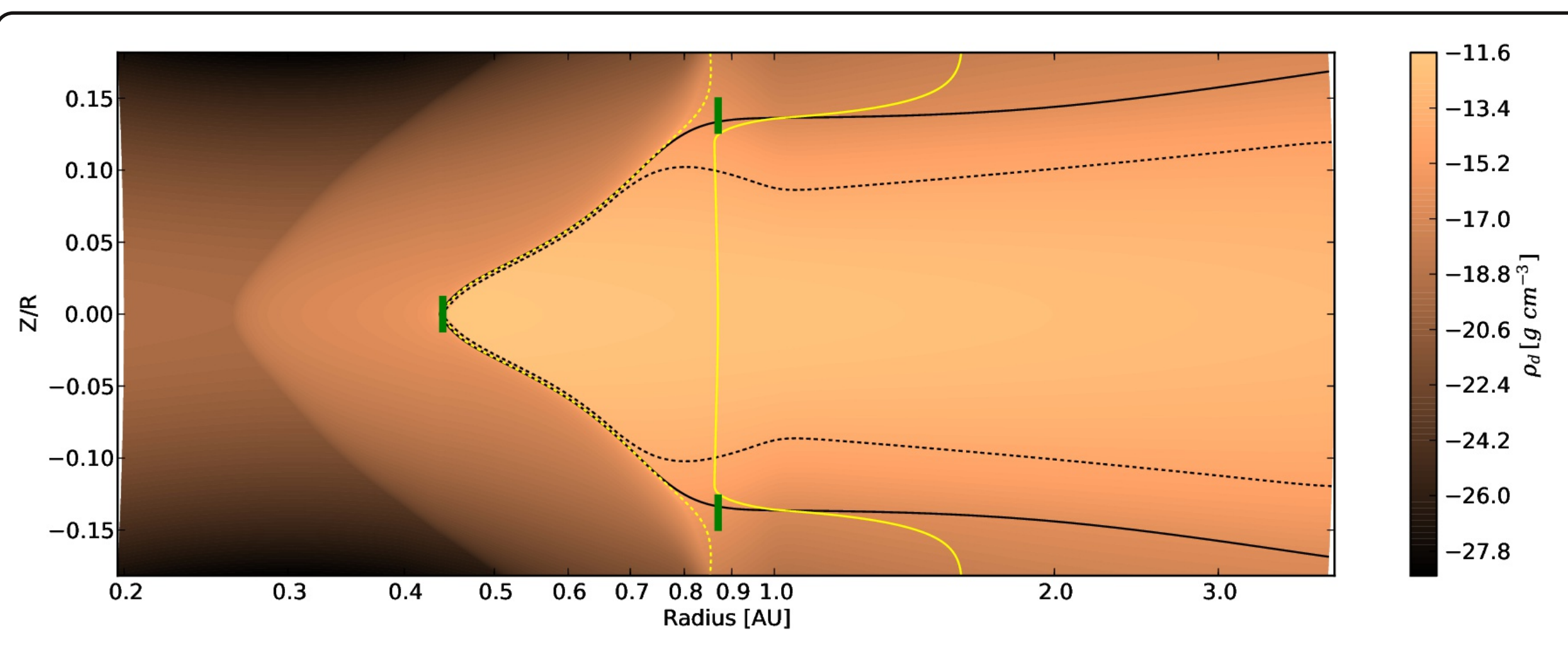
Many stars host planets orbiting within one astronomical unit. How the planets formed is a mystery, but we do know that conditions in the gas and dust near the star are governed by the surface where the starlight heats rocky grains to their vaporization threshold.

Until now, no models of this zone have treated the dynamics and moving shadows the dust casts on material beyond.

Method:

We developed the first radiation hydrodynamical model of the inner dust sublimation front, including stellar irradiation, accretion heating, dust cooling, realistic dust and gas opacities, dust sublimation and condensation.

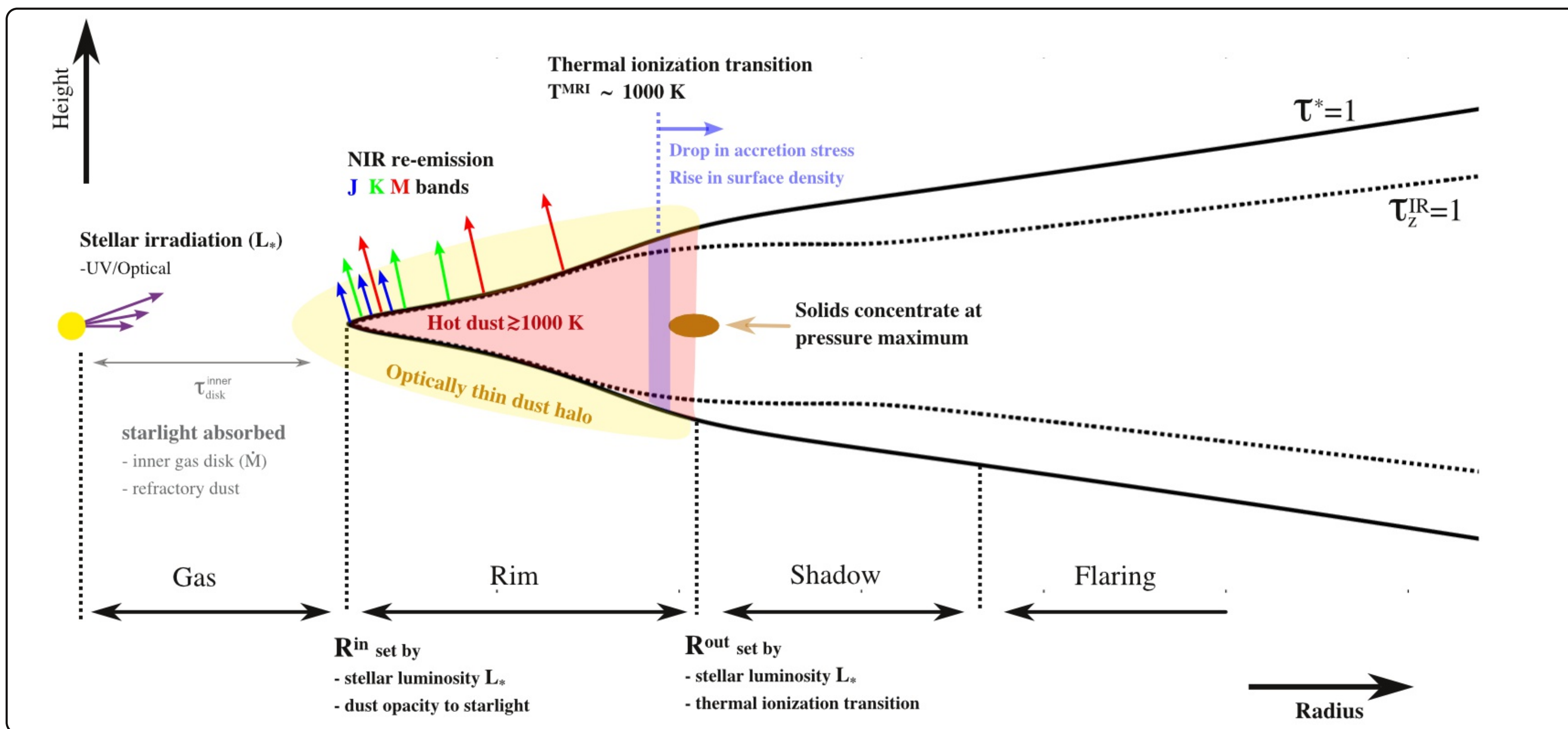
The models are inflow-equilibrium solutions with radially-constant mass accretion rates of 10^{-8} solar mass per year.



Dust density in the R - Z/R plane.

Black lines indicate the optical depth unity for the stellar irradiation (solid) and thermal re-emission (dashed line).

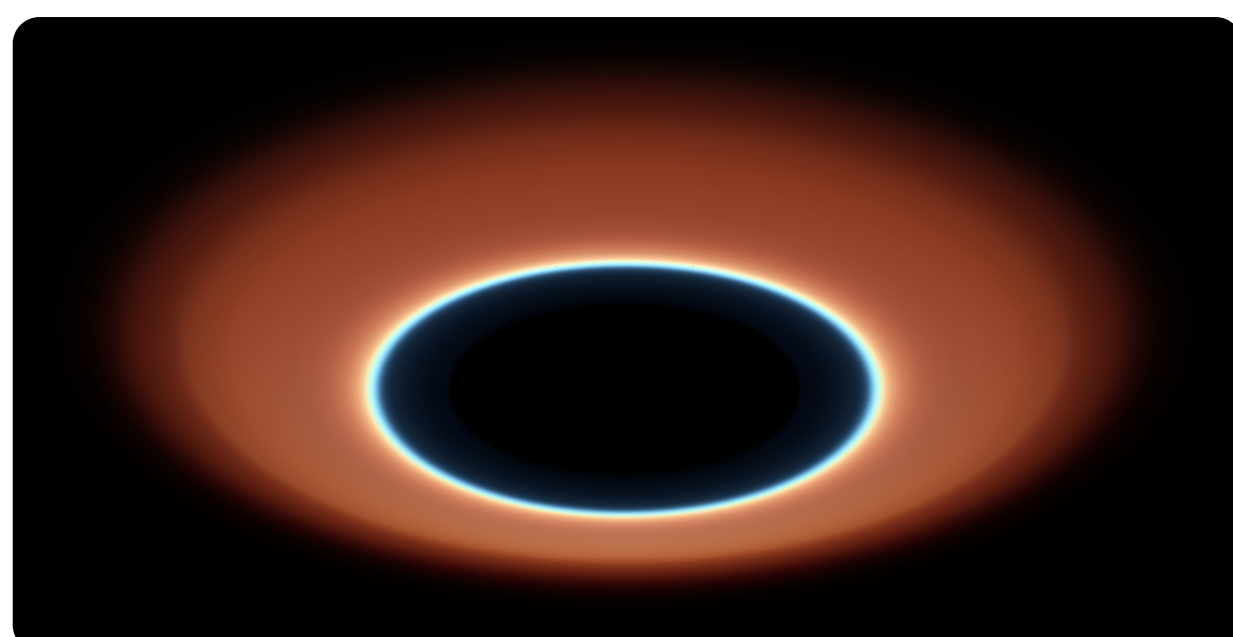
Yellow lines show the 1200 K (dashed) and 800 K (solid line) temperature contours. Green bars mark the inner and outer edges of the dusty surface directly lit by the star at the origin.



We show the first radiation hydrodynamical models of a protostellar disk's inner rim.

The models demonstrate the sublimation front is dynamically stable, and yield detailed predictions of the densities and temperatures where close exoplanets form and migrate.

We are able to obtain synthetic near-infrared images and compare with high-resolution observations.



Synthetic observation of the radiation hydrodynamical model, viewed 60 degrees from face-on.

The blue, green and red channels show the 1.25, 2.2 and 4.8 micron maps on a linear intensity scale. The white-hot ring marks the distance where the light from the central star vaporizes the dust.

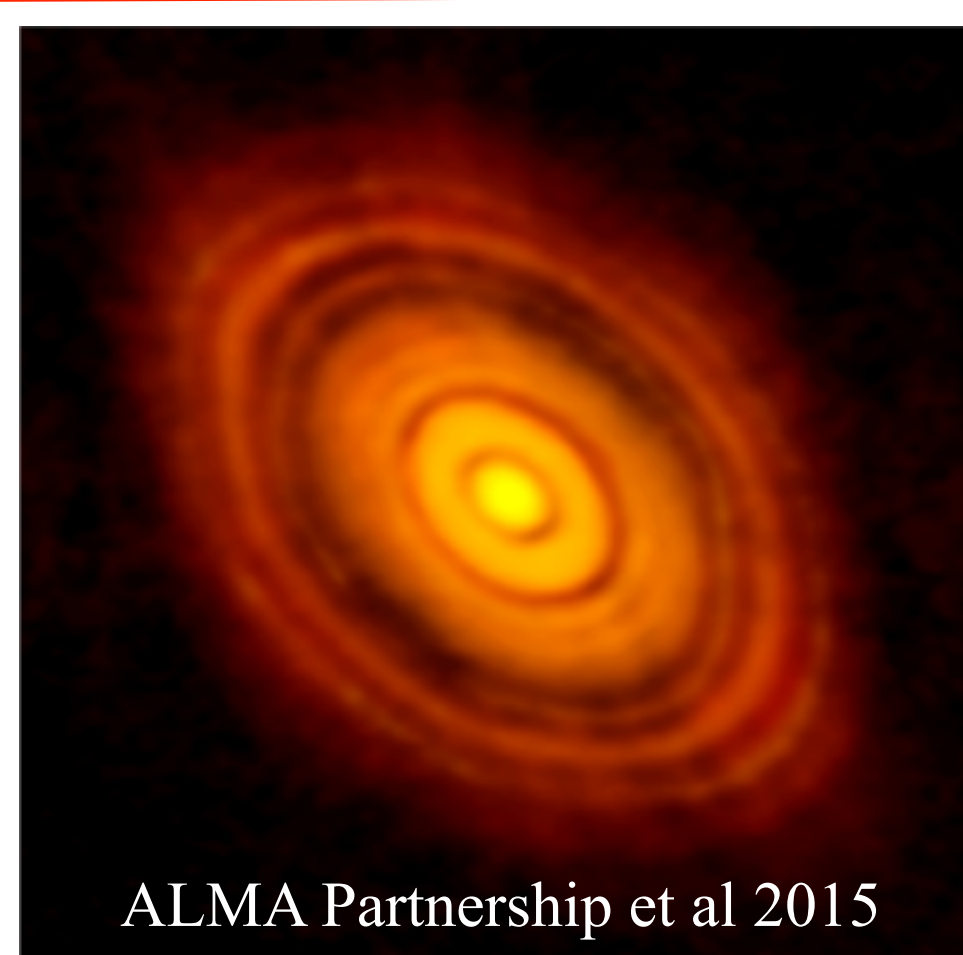
MagnetoCentrifugal Disk Wind Models: Application to ALMA Observations toward the HL Tau Disk

Author: Yasuhiro Hasegawa (JPL/Caltech: 3263)

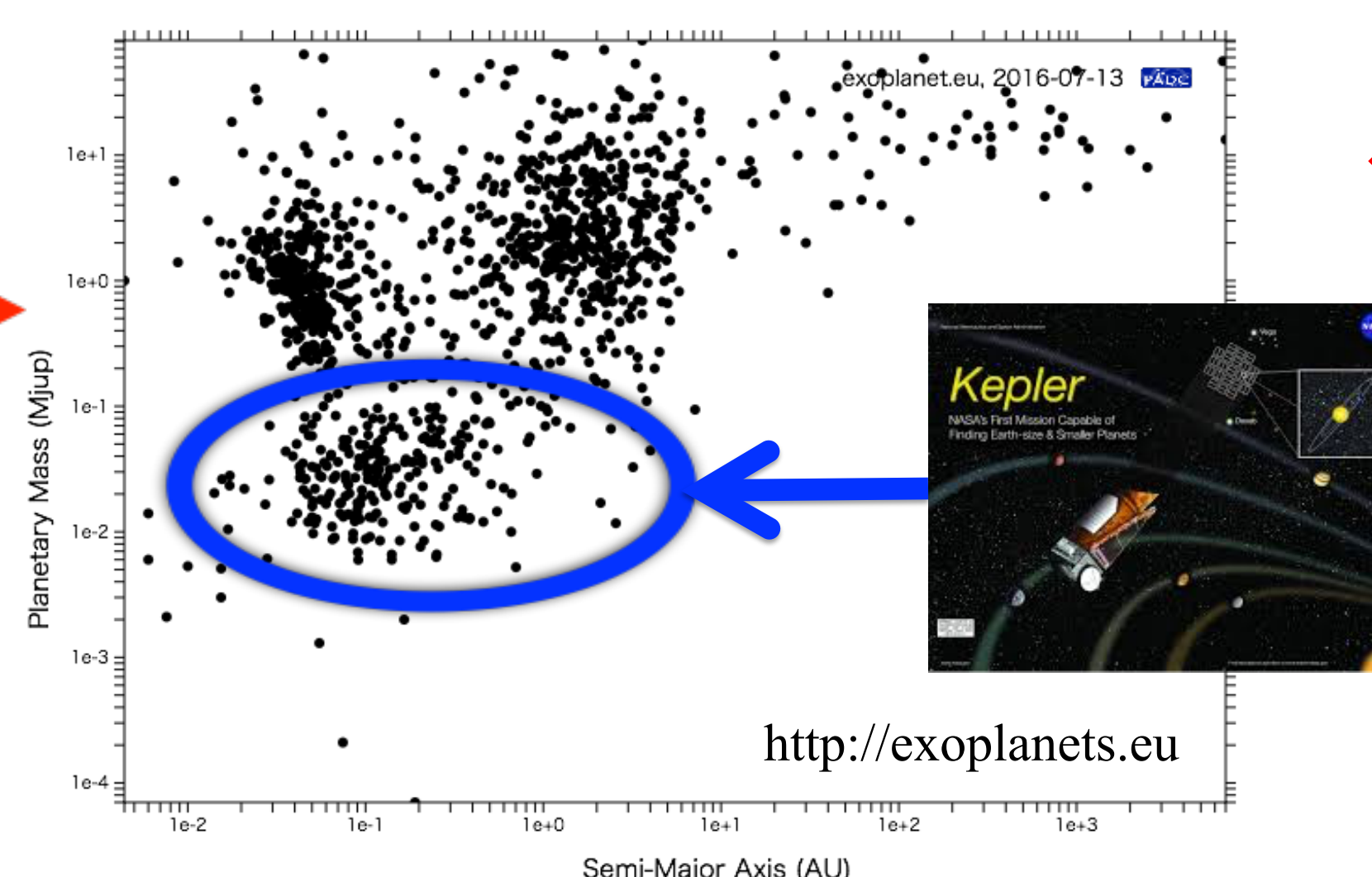
Neal Turner (JPL/Caltech: 3263), Satoshi Okuzumi (TokyoTech)

Introduction: Recent Astonishing Achievements in Exoplanet Sciences

- ◆ **ALMA Image of HL Tau**
- : a young (< 1 Myrs) YSO
- : multiple gaps in the dust continuum emission
- : signature of planet formation !?



~ a few Gyr

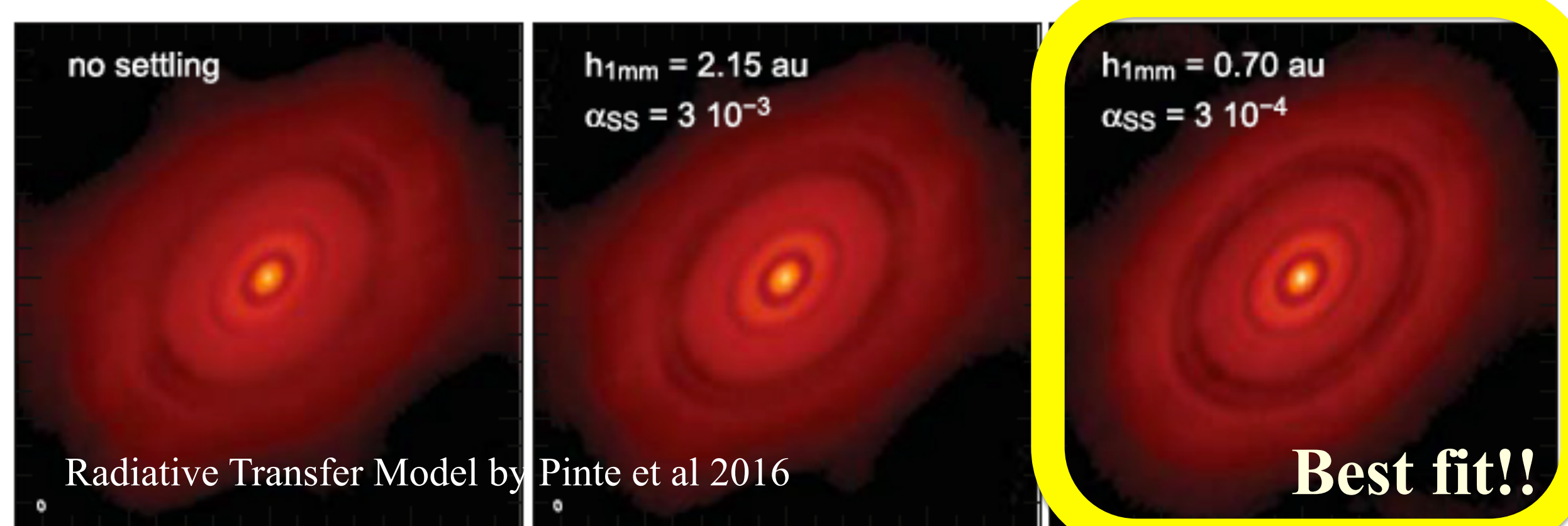


- ◆ **Exoplanet Populations**
- : rare (~ 1%) hot Jupiters
- : more warm Jupiters
- : most dominant super-Earths that do not exist in the solar system

Key Question: Solid Material Distribution in Protoplanetary Disks

- ◆ **High Global Diffusion**
- $\Rightarrow D_{GL} \simeq (10^{-2} - 10^{-1}) c_s^2 / \Omega$
- $\equiv \alpha_{GL} c_s^2 / \Omega$

: it is young and hence has a high disk accretion rate ($\simeq 10^{-7} - 10^{-6} M_{\odot} \text{yr}^{-1}$) (Hayashi et al 1993, Beck et al 2010)



- ◆ **Low Local Diffusion**
- $\Rightarrow D_{LC} \simeq \text{a few} \times 10^{-4} c_s^2 / \Omega$
- $\equiv \alpha_{LC} c_s^2 / \Omega$

: local turbulence should be weak because of a high degree of dust settling (Pinte et al 2016)

Disk Models: Three Possible Origins of Disk Accretion and Local Turbulence

- ◆ **Self-Gravity**
- (Gravitational instabilities, GIs)
- : GIs act as a self-regulating process, and disks become quasi-steady states

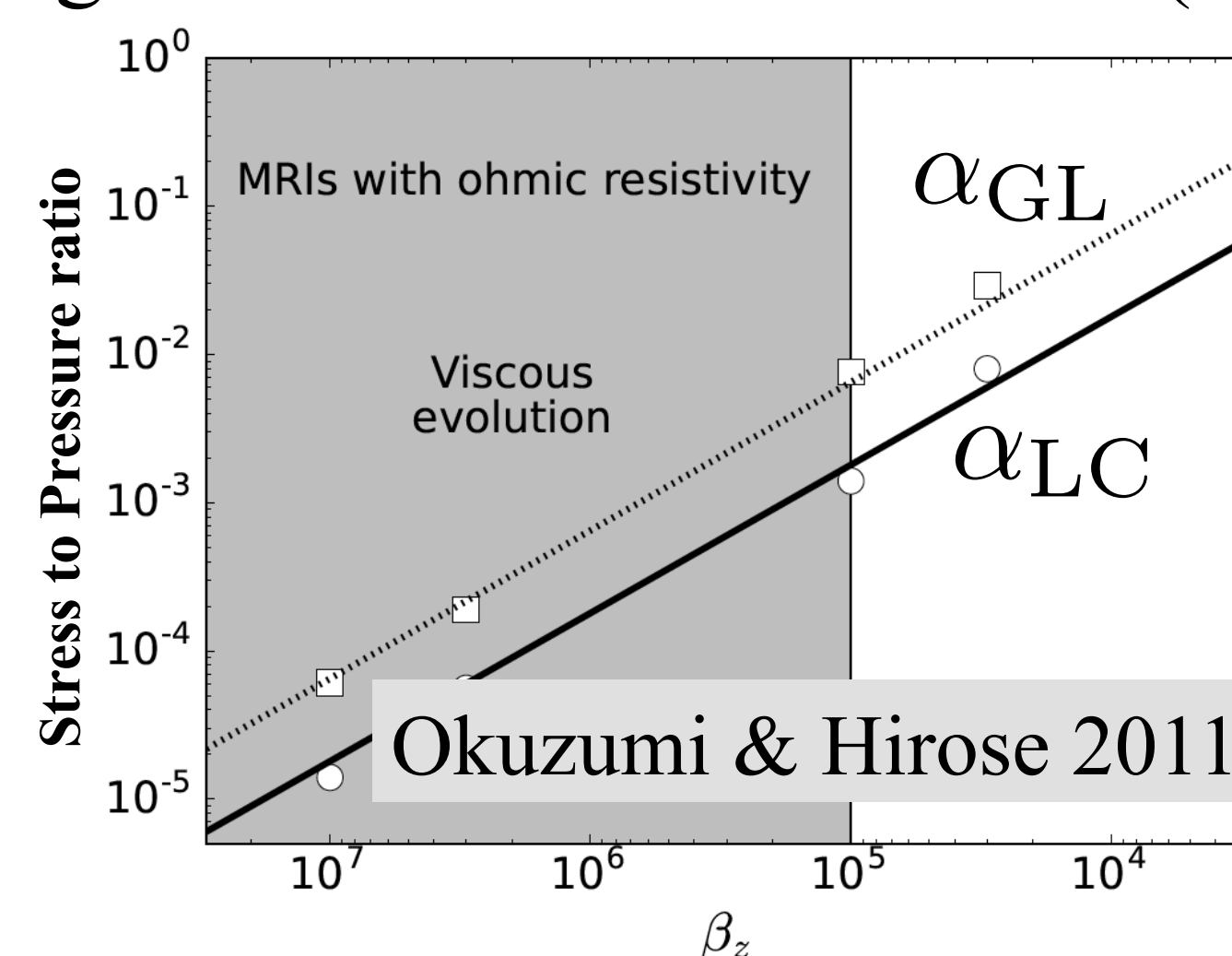
$$\alpha_{GL} \simeq \alpha_{LC} \simeq \frac{\dot{M}_g Q_0 G}{3c_s^3}$$

where $\dot{M}_g \simeq 3\pi\nu\Sigma_g$

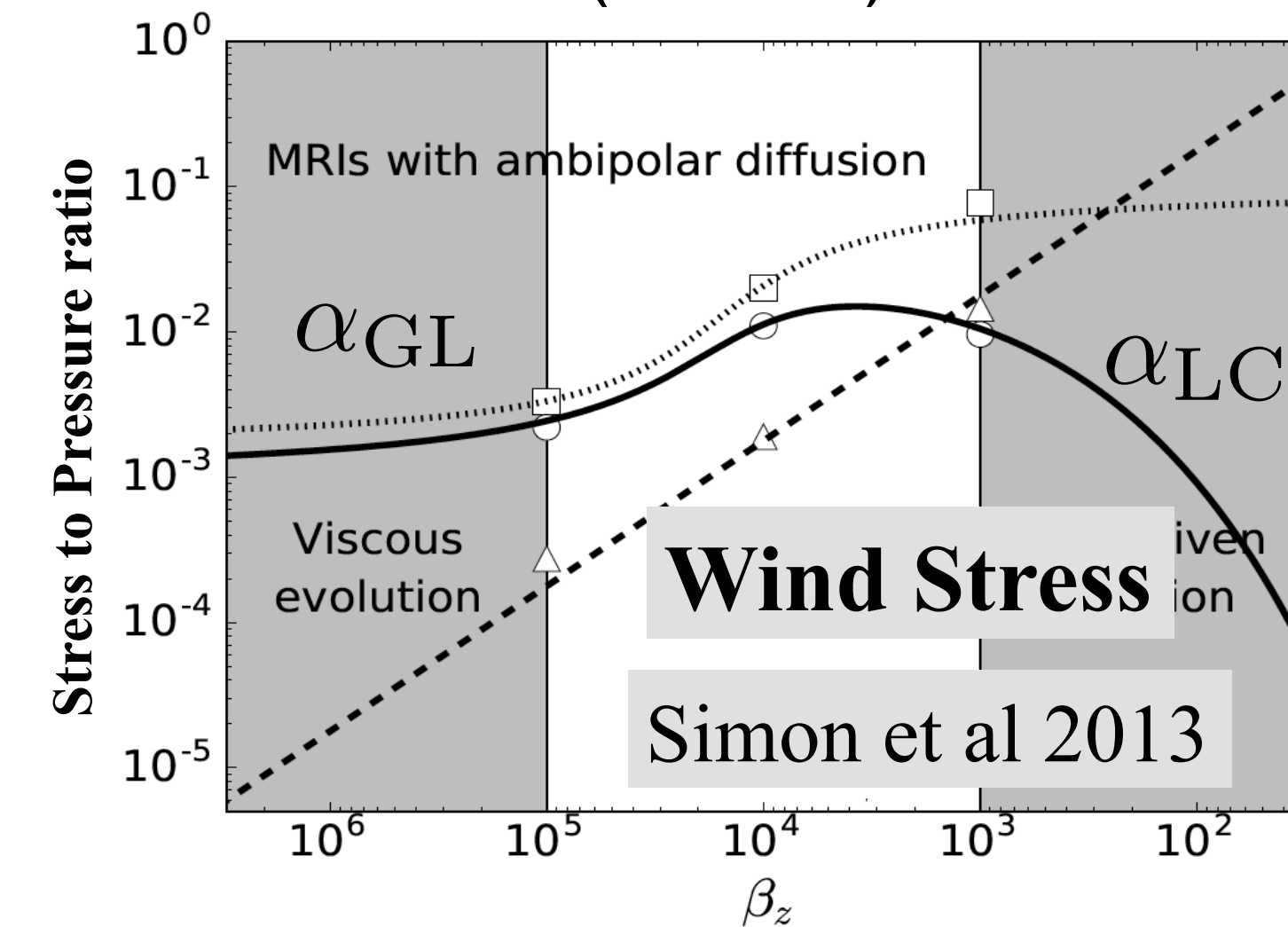
$$Q_0 \simeq 1.3 - 2 \quad \nu = \alpha c_s h_g$$

(e.g., Vorobyov & Basu 2007)

- ◆ **Magnetized Turbulence by magnetorotational Instabilities (MRIs)**



- ◆ **MagnetoCentrifugal Winds (MCW)**



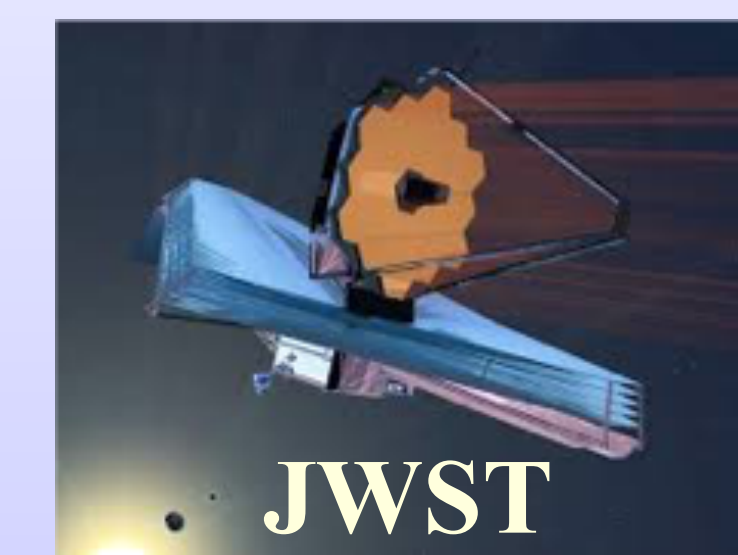
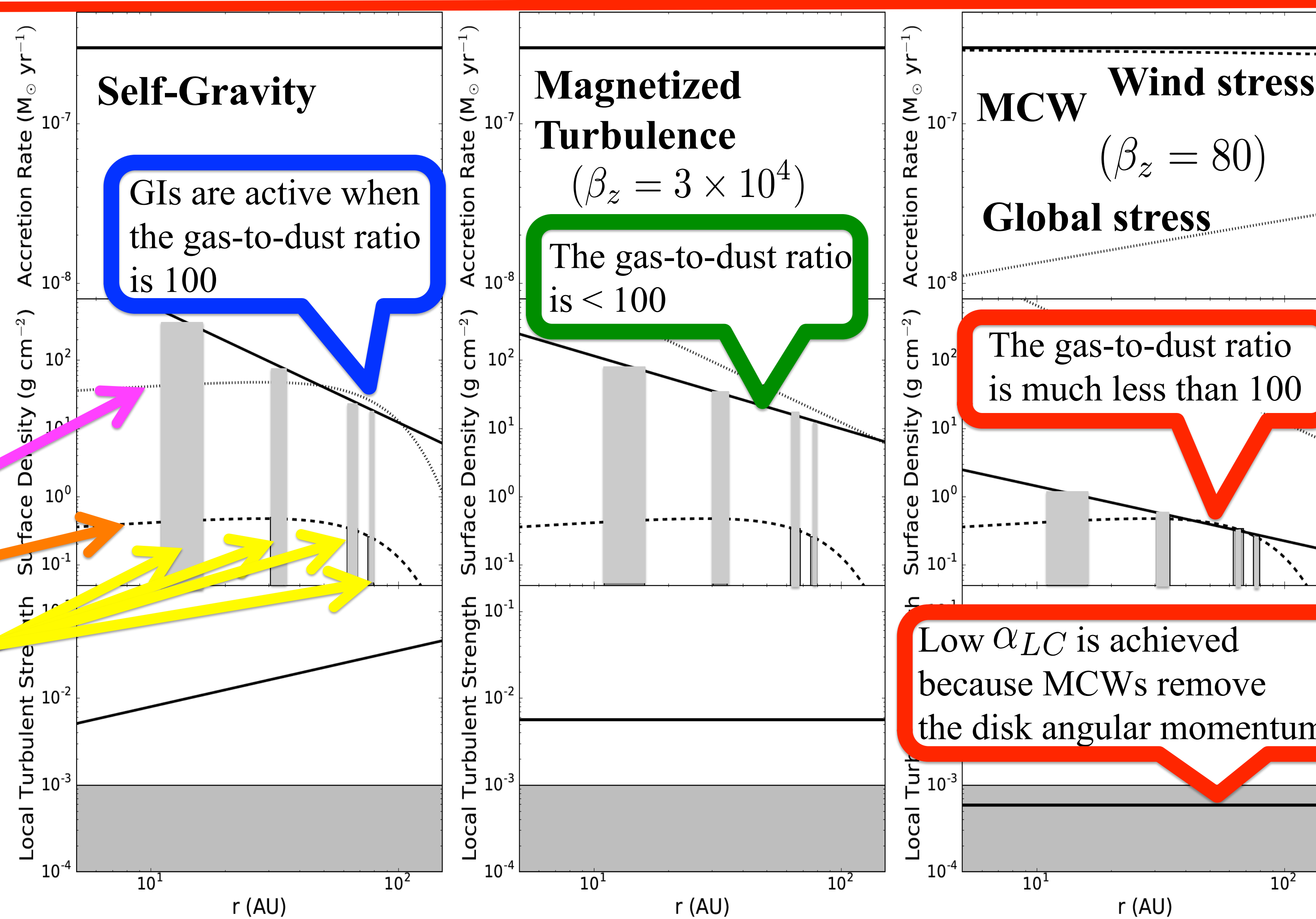
Results & Potential Impacts on JWST

Disks with a high α_{GL} and a low α_{LC} can be realized only for MCW models (right) when magnetic fields threading the disks are very strong

100 times Dust Distribution

Observed Dust Distribution

Locations of Observed Gaps



Two Potential Observational Tests:

- 1) Infer a Low Gas-to-Dust Ratio
- 2) Detect Gas Outflow from Disk Surfaces

Infrared Variability and Time Lags for Periodic Quasars

Hyunsung Jun (JPL, 3266), D. Stern, A. Mainzer (3266), M. J. Graham,
S. G. Djorgovski, A. J. Drake, A. A. Mahabal (Caltech), R. M. Cutri (IPAC)

Introduction

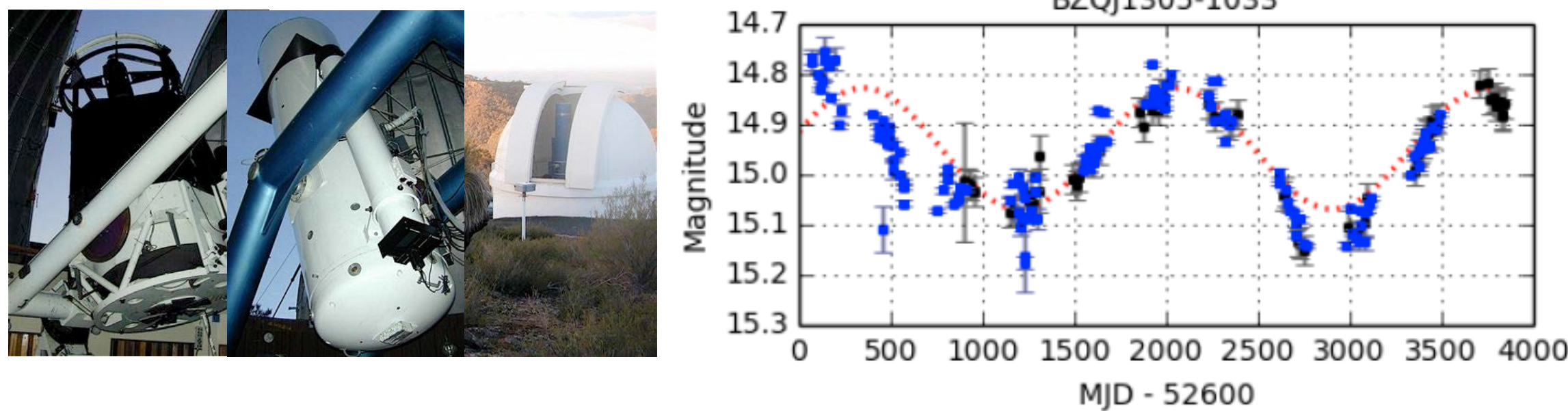
- Quasars (quasi-stellar radio objects) are luminous active galactic nuclei, powered by accreting supermassive black holes (BHs)
- The optical light curves of quasars are often fluctuating, witnessed early since the discovery of quasars
- Quasar variability happens in timescales of hours to years, typically originating from instabilities near the accretion disk or jet precession



Quasar accretion disk (left) and jet (right) surrounding the BH, credit: NASA JPL/Caltech

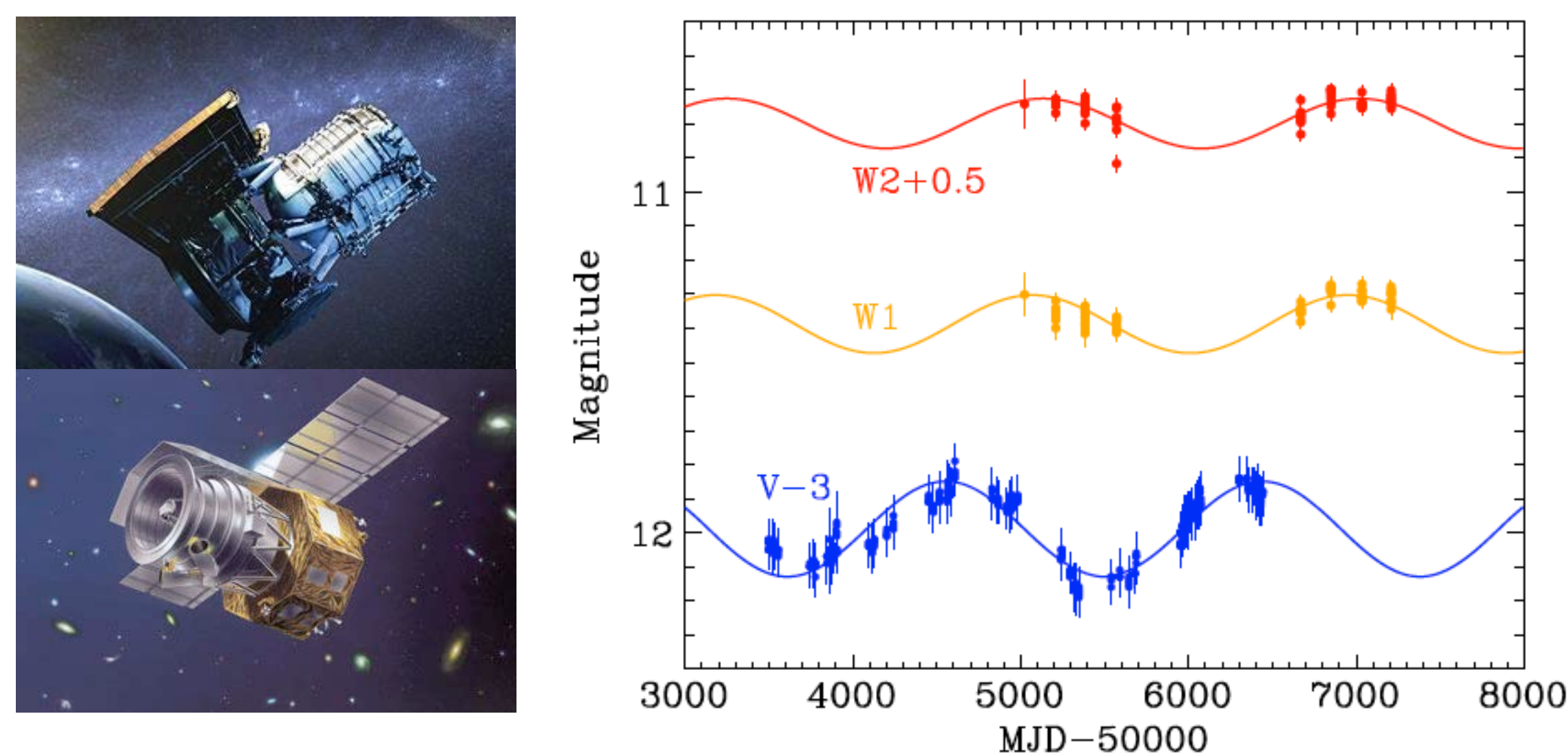
Objective

- Graham et al. (2015b) report 111/250,000 quasar light curves showing unusual, periodic signals over 1.5 cycles and a 9-yr baseline from the Catalina Real-Time Transient Survey (CRTS), thought to be produced from sub-pc binary BHs during gravitational wave dominated spiral
- With mid-infrared survey data available from WISE and Akari missions, we aim to measure i) the significance of the periodic amplitude in the infrared light curves, and ii) optical to infrared time lag, of one of the most pronounced periodic quasars, PG 1302-102



Three CRTS survey telescopes (left), optical light curves for PG 1302-102 (right) including the CRTS (black) and LINEAR (blue) data, credit: <http://nesssi.cacr.caltech.edu/CRTS>

Observations of periodic IR light curves



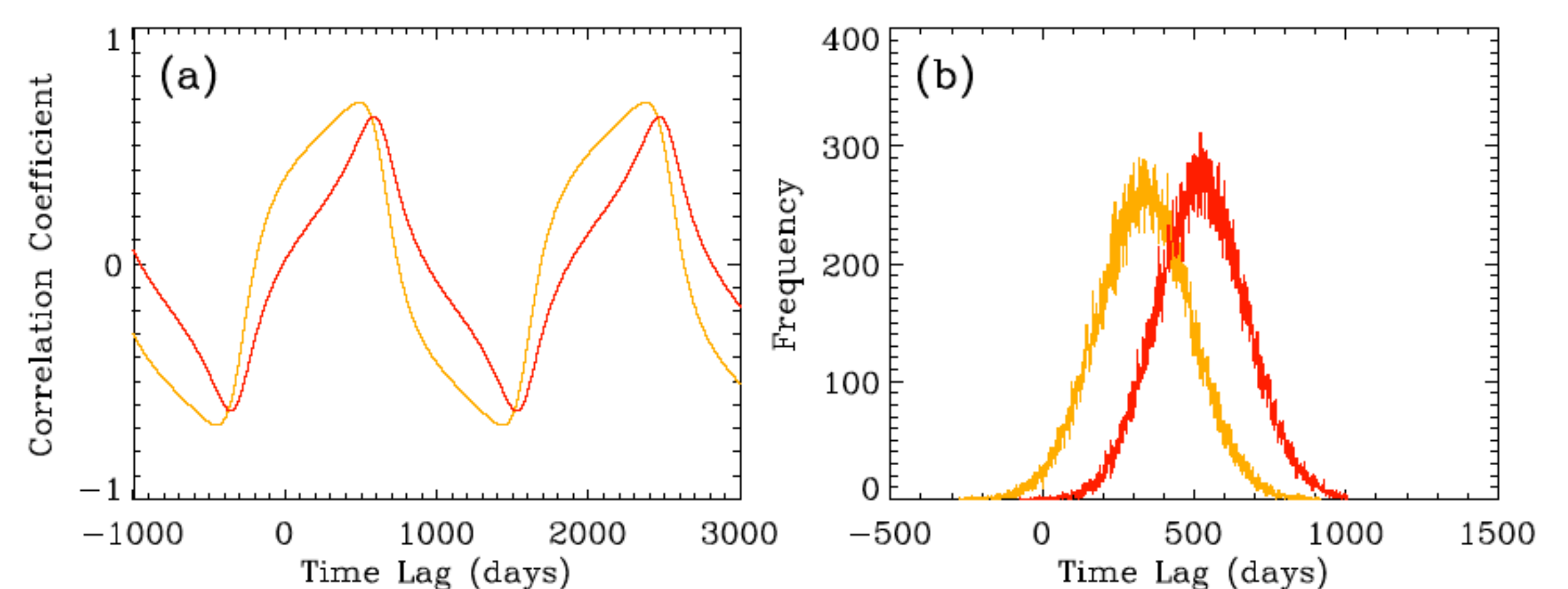
WISE and Akari space telescopes (left) and the optical (CRTS V-band, blue), 3.4 um (W1, yellow), and 4.6 um (W2, red) light curves for PG 1302-102 (right), where ongoing NEOWISE Reactivation survey will cover 2-3 more groups of data by the end of 2016, credit: NASA/JAXA

- We fit the IR data with a sinusoid with period fixed to that of the optical, 5.2 yrs (Graham et al. 2015a)
- We measured the periodic $S/N=A^2/2\sigma^2$, the ratio of the power by the signal to that by the noise, where A =amplitude of the model sinusoid, σ =rms residual of the data after model subtraction
- $S/N=5.7, 4.1, 3.4$ at V-band, 3.4 um, 4.6 um, corresponding to false period alarm probabilities of below 10^{-9} (Horne & Balinuas 1986)

Measurement of IR time lag based sizes

- We measure the IR time lags (τ) by cross correlating the optical model to the IR data, yielding infinite number of periodic solutions
- Uncertainties to the time lags were determined by Monte Carlo simulations of optical models including the measurement uncertainty of the optical period and magnitudes (Peterson et al. 1998)

$$\begin{aligned} \tau_{W1} &= (335 \pm 153) + 1884n \\ \tau_{W2} &= (524 \pm 148) + 1884n \end{aligned} \quad \tau \text{ in days, } n=\text{any integer}$$



The correlation between the optical model and IR data (left, W1 yellow and W2 red) and the measured distribution of simulated optical to IR time lags (right)

- The most likely range of n values are determined assuming that the rest-frame near-IR radiation comes from the inner dusty structure of a quasar at a dust sublimation radius for graphite grains.
- For a face-on orientation $n=1$ ($\tau \sim 2300$ days, $R \sim 1.5$ pc) best fits the size of the dusty region, and for an edge-on orientation $n=2$ ($\tau \sim 4200$ days, $R \sim 1.1$ pc)

$$\tau = R(1 + \sin i)/c + T/2 \quad \begin{array}{l} i = \text{inclination angle,} \\ T = \text{optical period} = 1884 \text{ days} \end{array}$$

Conclusions & Ongoing work

- Through the analysis of mid-IR light curves of PG 1302-102, we find that
- The IR data follows the periodic variability seen in the optical, consistent with a sub-pc binary BH system (Graham et al. 2015ab) in a galaxy merger (Guyon et al. 2006; Hong et al. 2015)
 - The time lag between the optical and IR light curves indicate a light travel time distance to the dusty material surrounding the BH with a \sim pc scale inner boundary, consistent with the periodic variability occurring within the accretion disk rather than the jet
 - We are exploring the entire IR light curves of 111 periodic quasars, in order to make a statistical argument on the significance and origin of periodic quasar variability

- Acknowledgement: This research was supported by an appointment to the NASA Postdoctoral Program at the Jet Propulsion Laboratory, administered by Universities Space Research Association under contract with NASA
- References: Graham et al. 2015a, Nature, 518, 74; Graham et al. 2015b, MNRAS, 453, 1562; Guyon et al. 2006, ApJS, 166, 89; Hong et al. 2015, ApJ, 804, 34; Horne & Baliunas 1986, ApJ, 302, 757; Peterson et al. 1998, PASP, 110, 660

The expansion of the Universe is accelerating

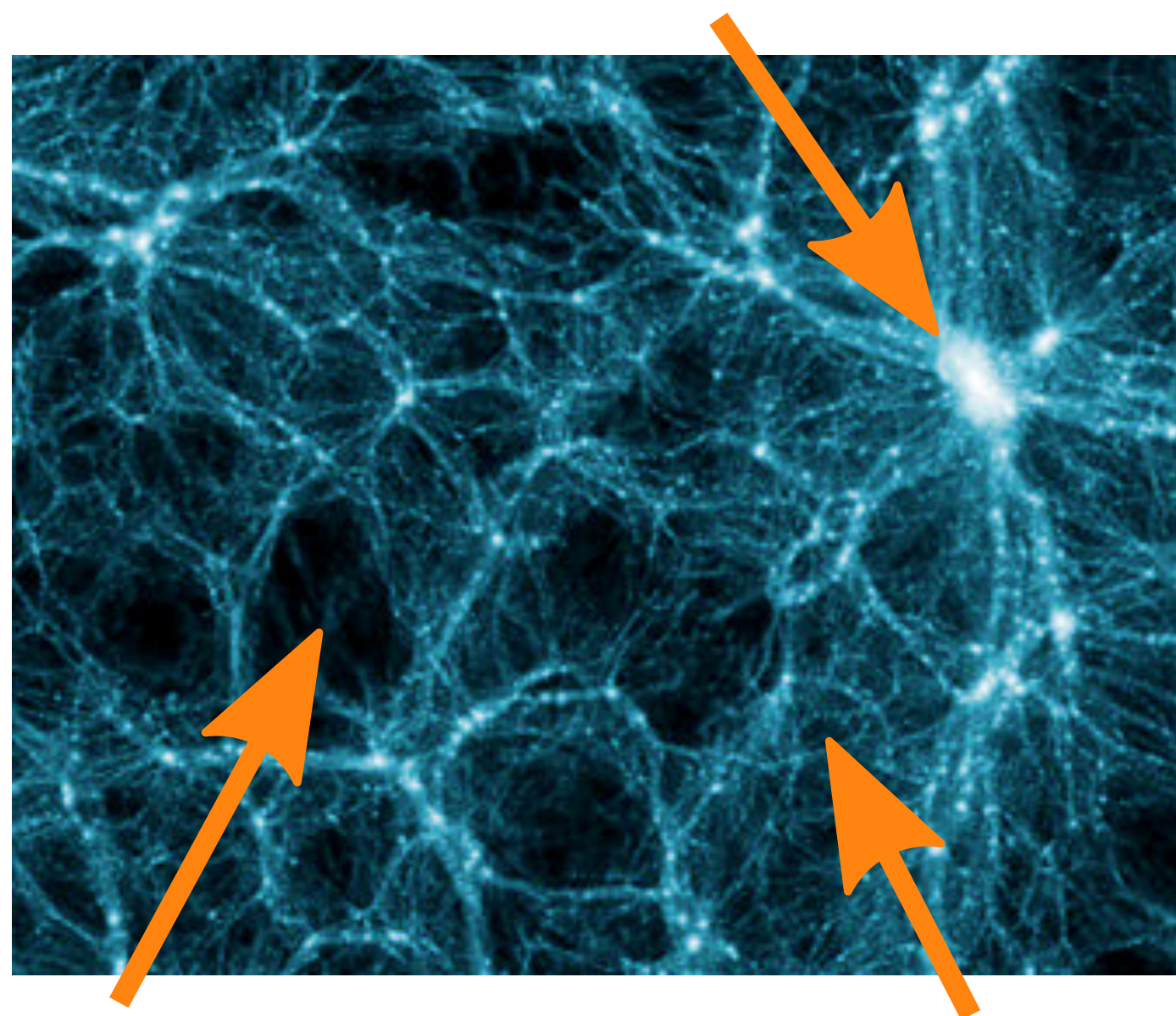
- But why? Huge problem for fundamental physics!
Maybe GR is modified on cosmic distance scales?

Alternative theories of gravity can explain acceleration by adding a new **5th force** of Nature.

Testing General Relativity with the environment-dependence of the cosmic velocity field

Philip Bull (3268)*

Screened
(galaxies/clusters)



Unscreened
(voids)

Transitioning
(cosmic web)

A 5th force must be *screened* at small distances

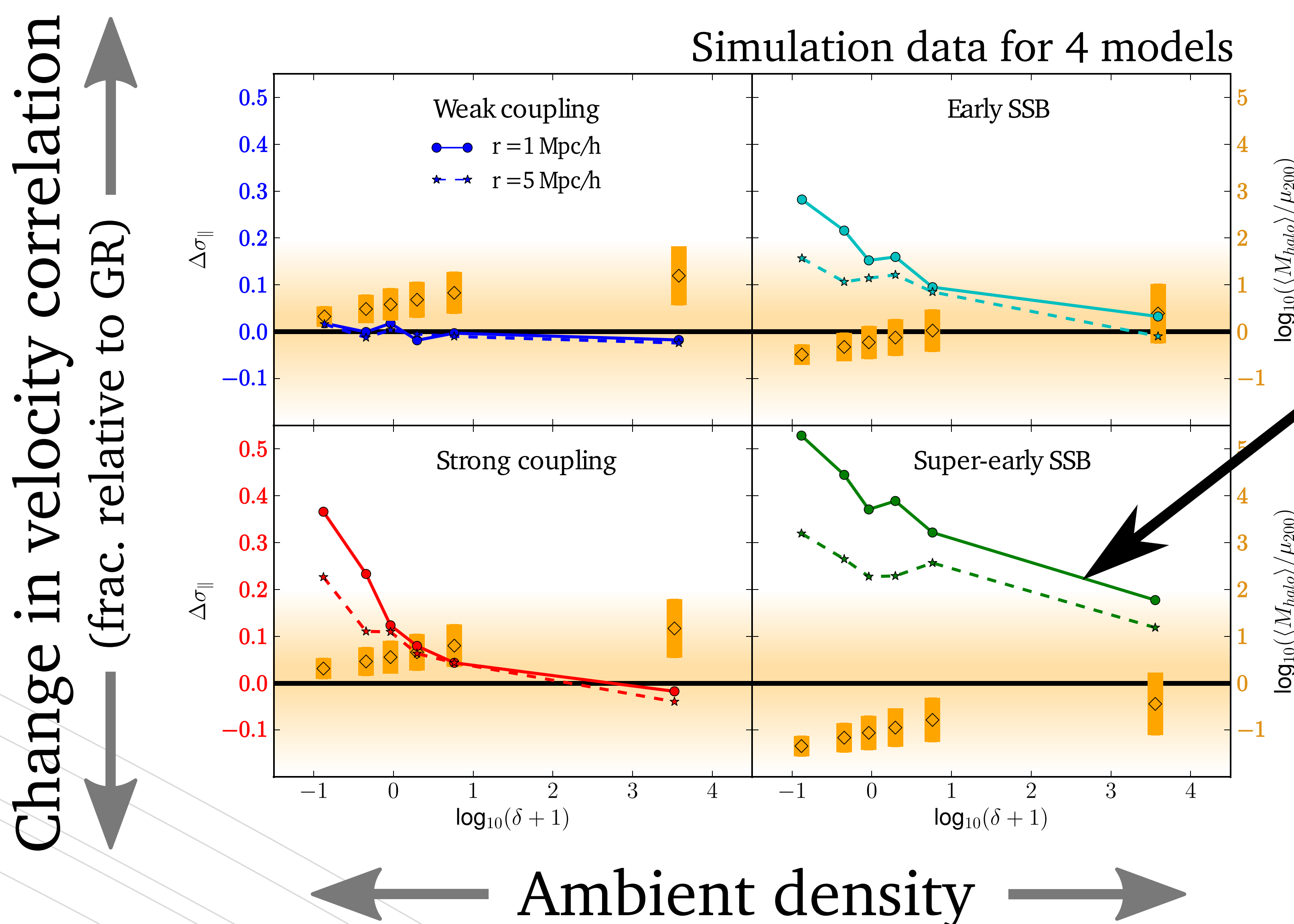
- Tests on Solar System scales match GR *extremely* well, so alternatives must mimic GR here!

Can build theories where the strength of the 5th force depends on the **local environment**, e.g. matter density

A way of observing the screening transition!

- Measure how galaxy velocities are correlated.
Then, bin by the *density of their local environment*.

- Obtained N-body simulations for several modified gravity models
- Developed a **new estimator** for measuring velocity correlations



Clear dependence on ambient density!
Signature of transition (seen if GR is modified)

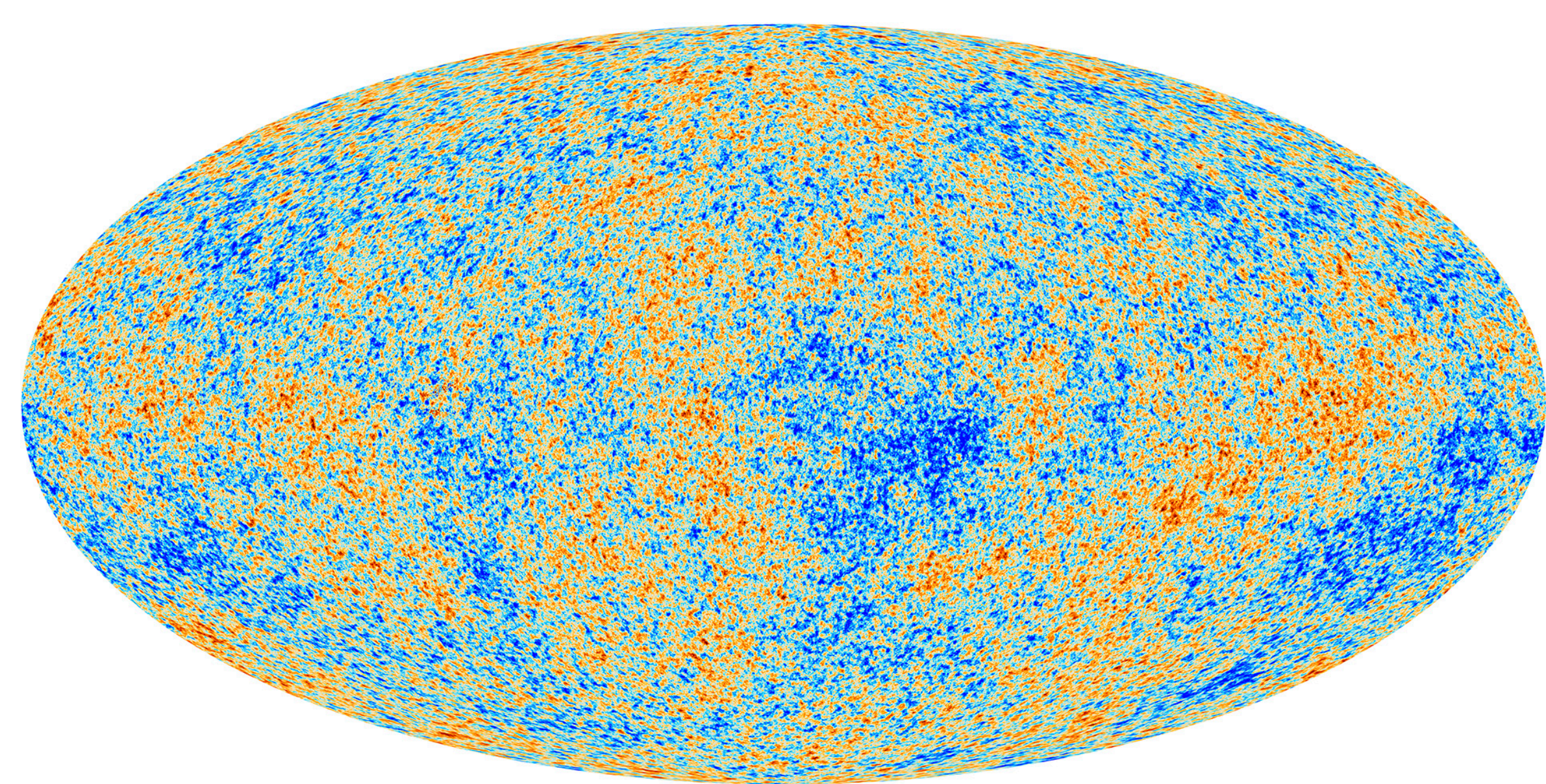
Environment-dependent clustering statistics:
Powerful new tests of GR with WFIRST/SPHEREx

Non-Gaussianity as a test of Inflation

Jérôme Gleyzes (3268)

With Roland de Putter (Caltech) and Olivier Doré (3268)

What were the initial conditions of the Universe?



Snapshot of our Universe 378 000 years after the Big Bang, as seen by the Planck satellite. The different colors correspond to perturbations in the temperature.

The initial conditions are:

- Close to Gaussian
- Scale independent

Evolve General Relativity backwards



The simplest picture: **Inflation**

Period of accelerated expansion, cannot be caused by ordinary matter.

What was going on during inflation?

Simplest scenario: "single field"

A single "quintessence fluid" :
with **negative pressure** unlike usual matter

Scale independent perturbations



Non-Gaussianity necessarily small

Extensions: "multifield"

Multiple "quintessence fluids"

Scale independent perturbations

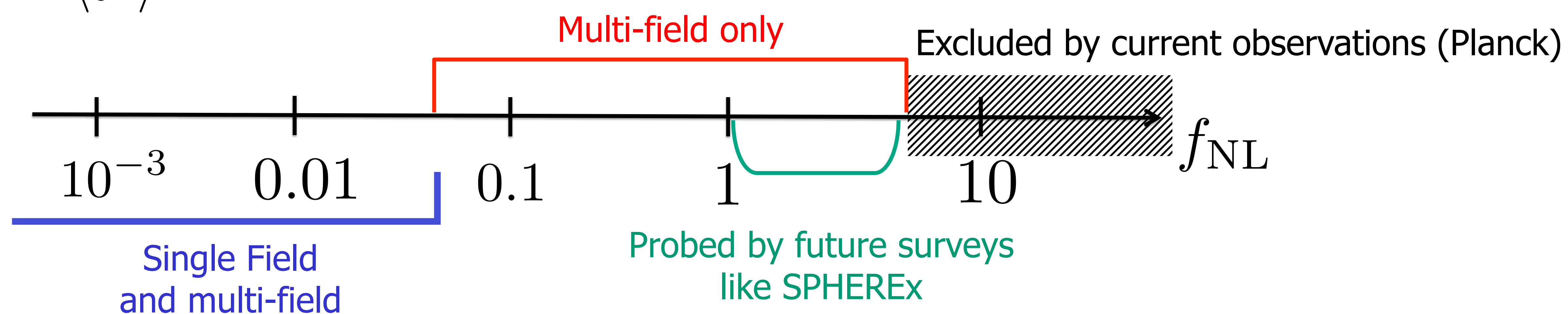


Non-Gaussianity **not** constrained

How to distinguish these scenarios?

$$f_{\text{NL}} \sim \frac{\langle \delta^3 \rangle}{\langle \delta^2 \rangle^2}$$

quantifies the Non-Gaussianity for a variable δ , with average $\langle \delta \rangle$



$f_{\text{NL}} \geq 1 \rightarrow$ Rules out simplest scenario

$f_{\text{NL}} \ll 1 \rightarrow$ Not much information:
most multi-field models actually predict negligible non Gaussianity.

Physical Models of Dust Emission and Polarization in the Planck Era

Author: Brandon Hensley (3268)

In Collaboration With: B. T. Draine (Princeton), H. K. Eriksen (Oslo), I. K. Wehus (Oslo)

Introduction

- Dust grains are heated by the interstellar radiation field and emit in the infrared
- These grains are **aspherical** and preferentially **aligned** with the interstellar magnetic field, causing this emission to be polarized
- This emission is a major contaminant for studies of the polarized Cosmic Microwave Background (CMB)
- Dust polarization also encodes information on the size, shape, and composition of interstellar grains
- We seek a **physical model** of interstellar dust to provide better foreground subtraction for next-generation CMB experiments

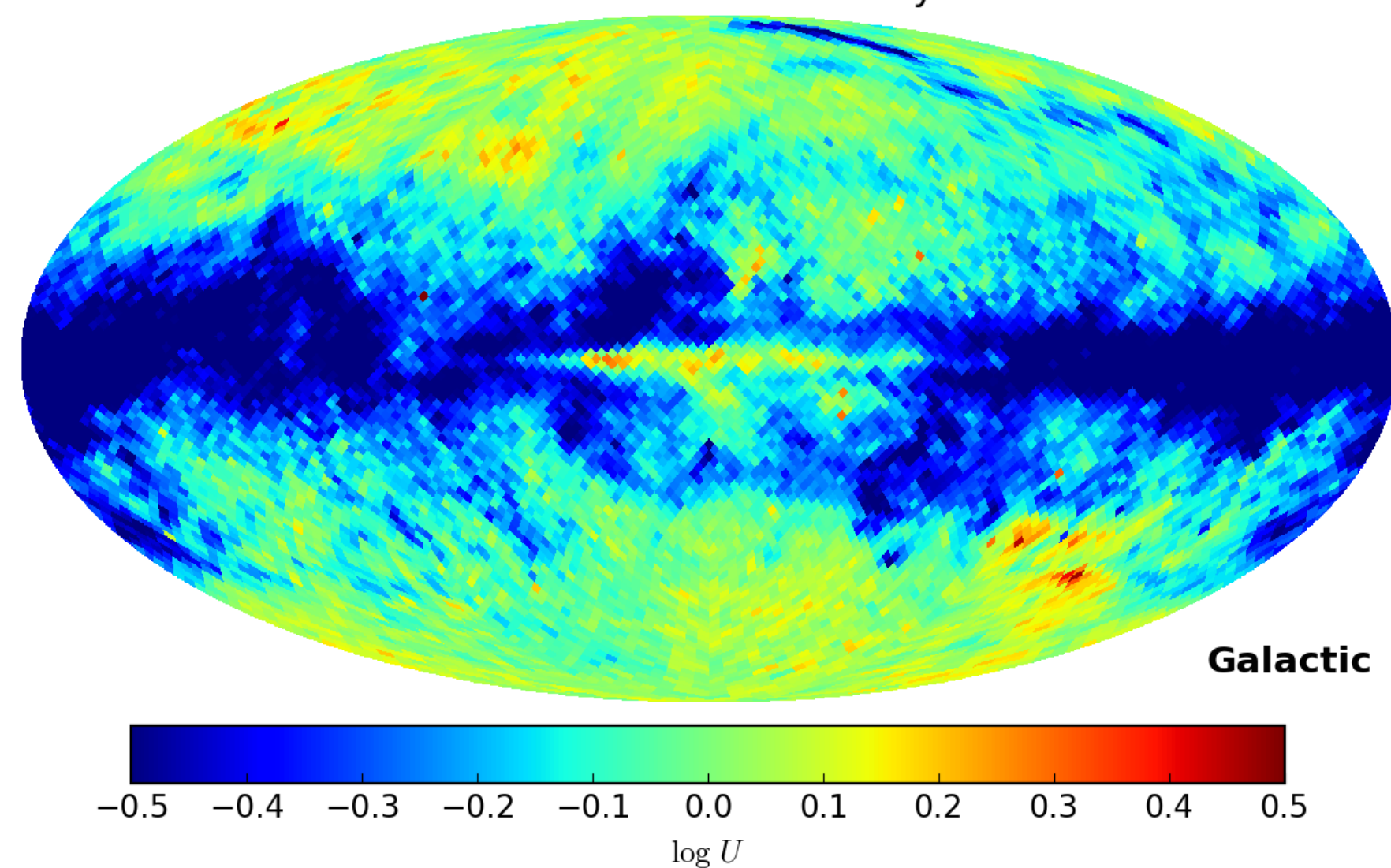
Step 1: Building a Model

- Big idea: leverage observations of dust at all wavelengths in both **emission** and **extinction**, total and polarized, to constrain the dust physics
- Model the material properties of **carbonaceous** and **silicate** grains (sum in black) as a function of size, shape, and frequency

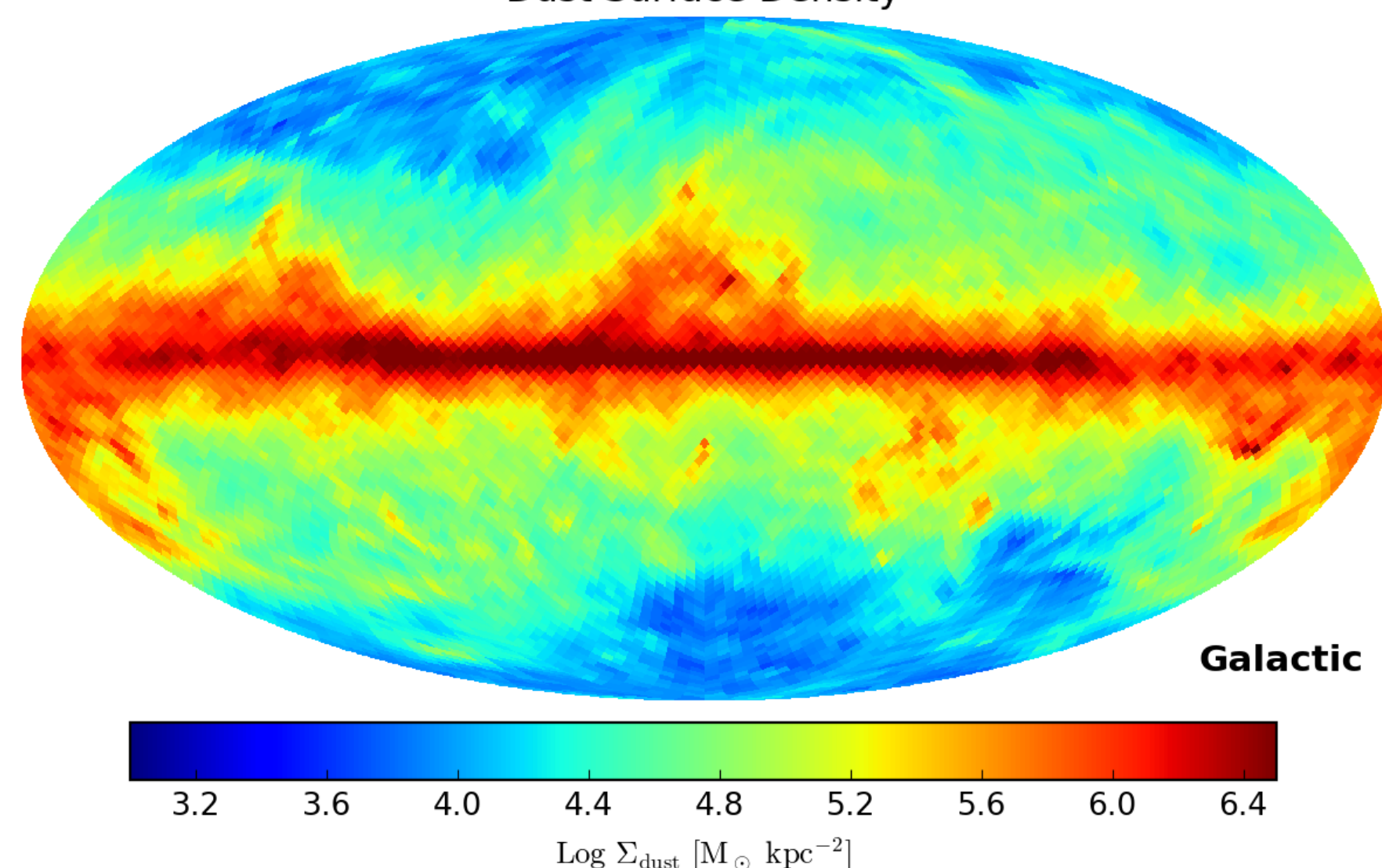
Step 2: Fitting the Model

- Parameterize model in terms of:
 - Intensity of starlight heating dust (dust temperature)
 - Amount of dust of each composition
- Fit parameterized model to full sky *Planck* data to make maps of **physical** dust parameters

Radiation Field Intensity

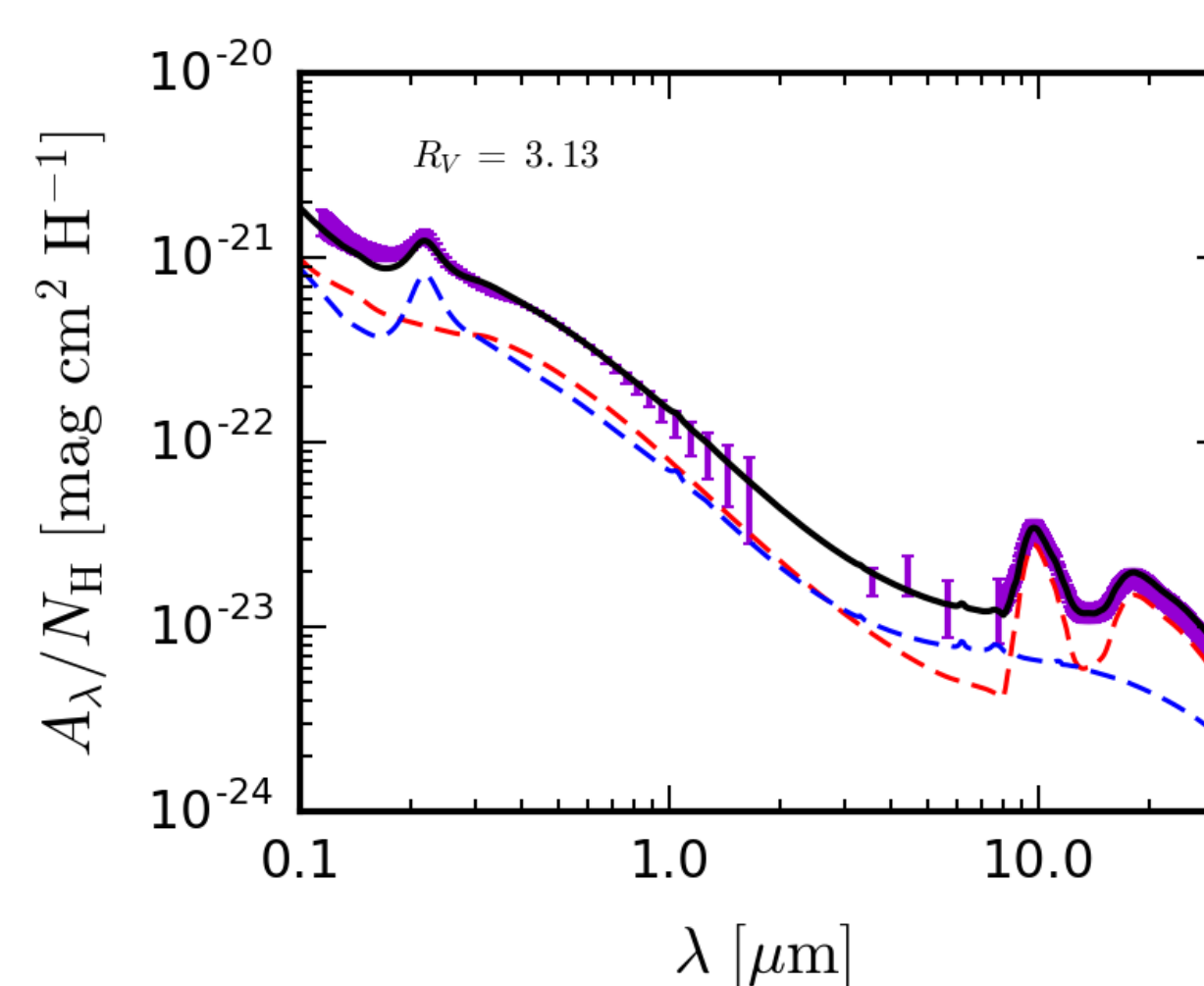


Dust Surface Density

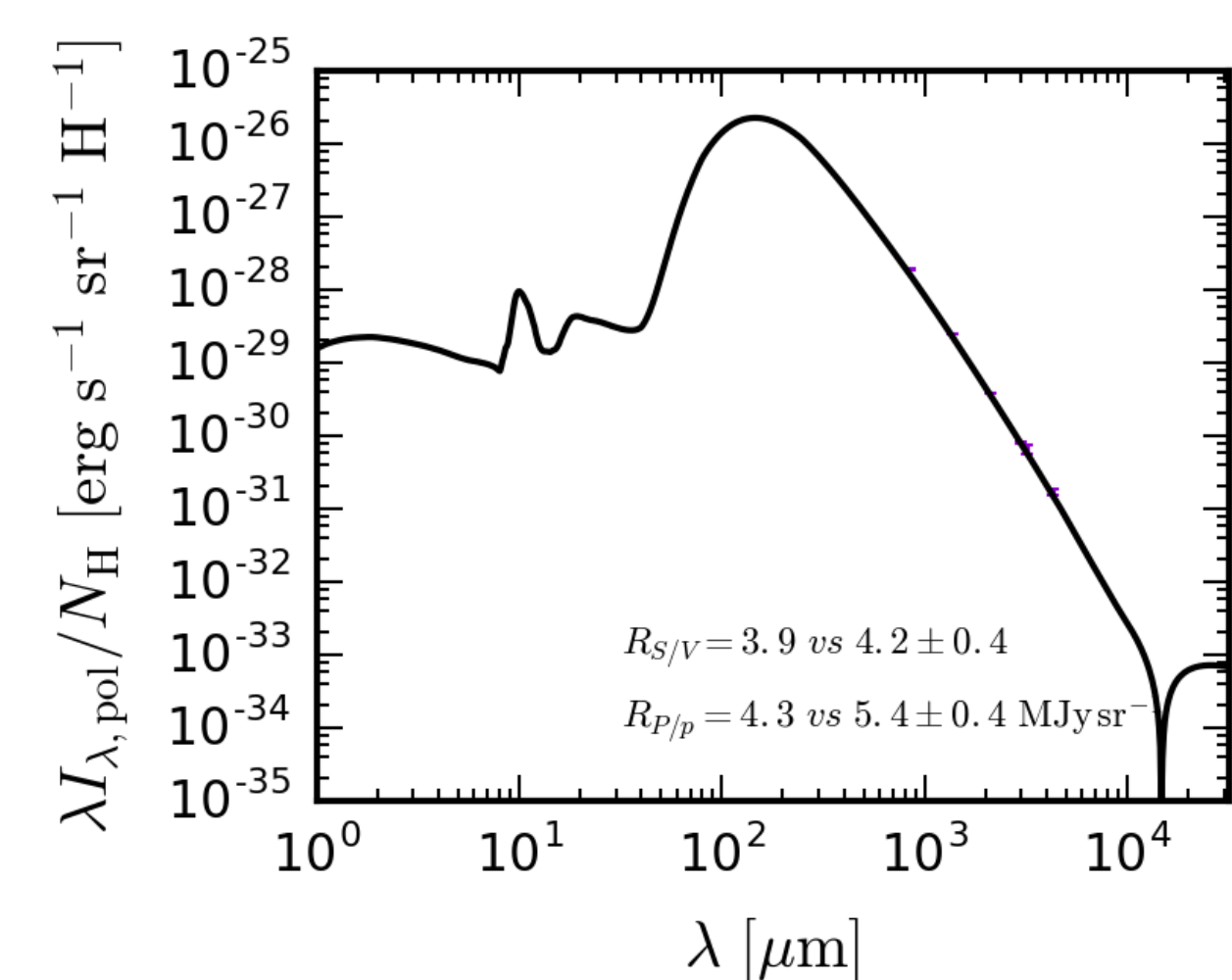
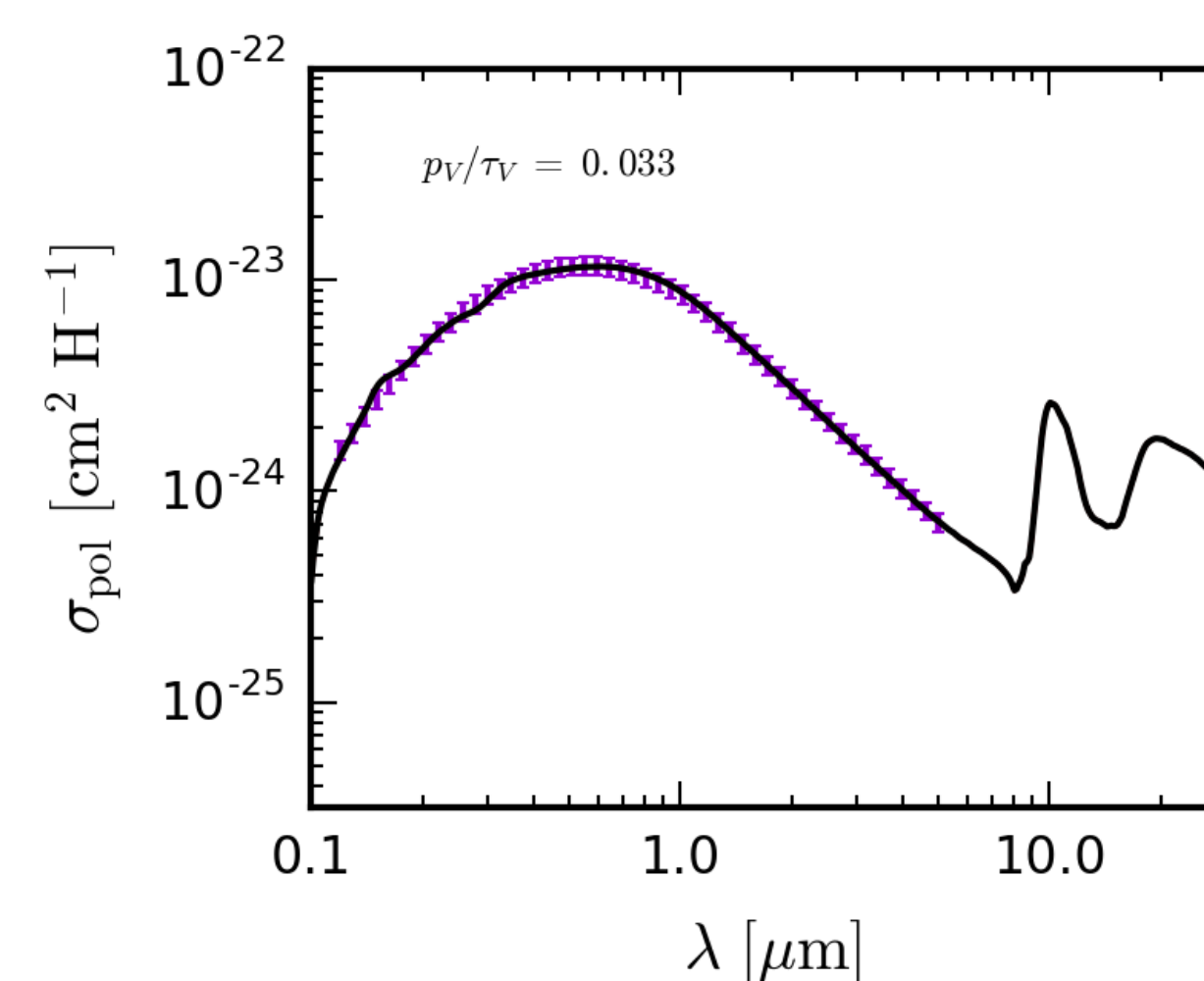
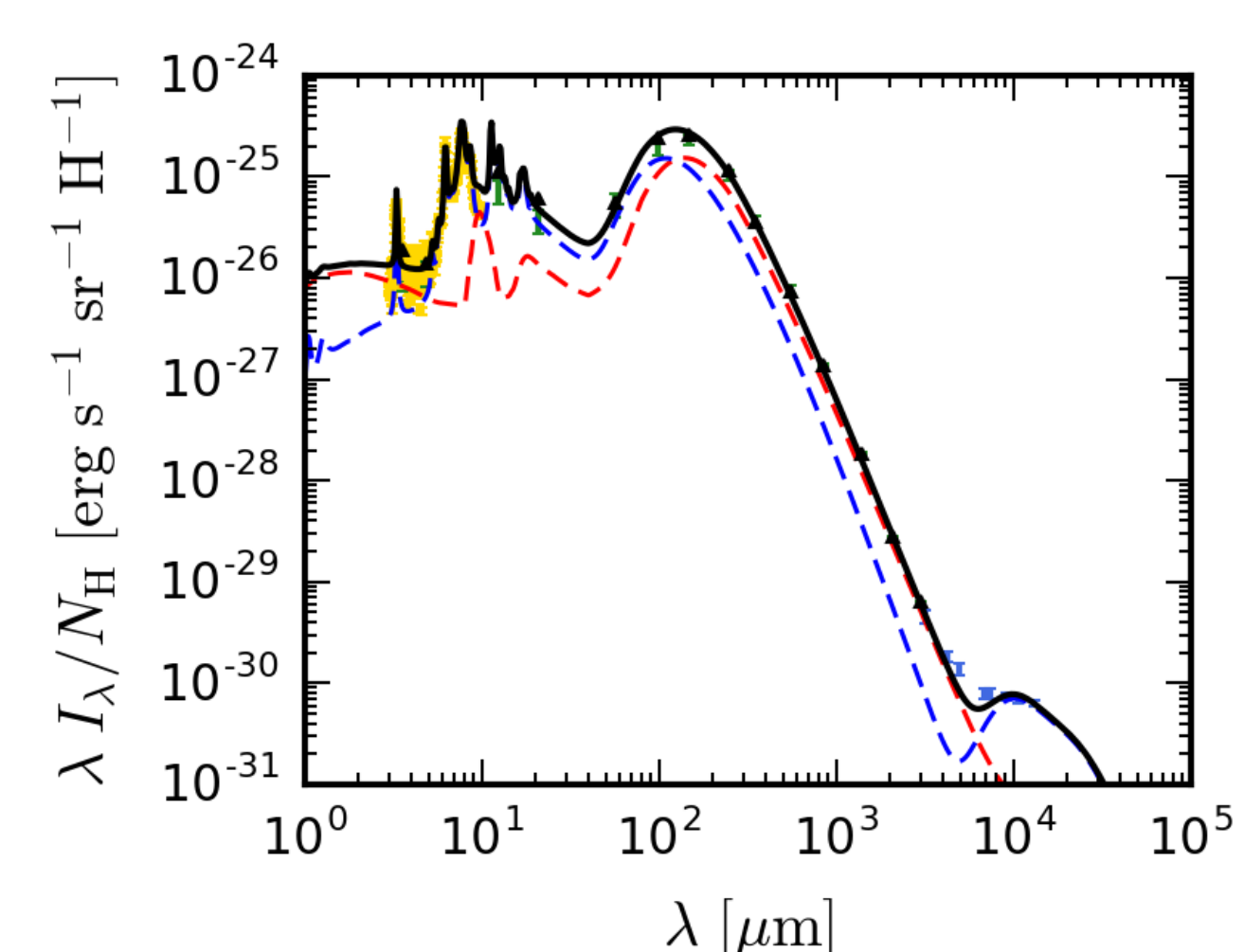


Model Fits for Mean Diffuse Galactic Dust

Extinction



Emission



Step 3: Using the Model

- Study evolution of dust properties in the Galaxy
- Incorporate models into component separation algorithms
- Construct simulated dust skies to test designs for next-generation CMB polarization experiments

Conclusions

- We have constructed a model of consisting of silicate and carbonaceous grains that can reproduce in detail the observed extinction and emission, both total and polarized, from interstellar dust
- We have fit a parameterized version of this model to the *Planck* sky to derive full-sky maps of Galactic dust properties. Refinements are ongoing.
- This new model enables work both on the evolution of dust properties in the interstellar medium as well as foreground modeling for CMB experiments that is anchored on a physical model.

Evidence of Halo Assembly Bias in Massive Clusters

Hironao Miyatake (3268)

Surhud More, Masahiro Takada (Kavli IPMU), David N. Spergel (Princeton)

Rachel Mandelbaum (CMU), Eli S. Rykoff (KIPAC/SLAC), Eduardo Rozo (University of Arizona)

Introduction

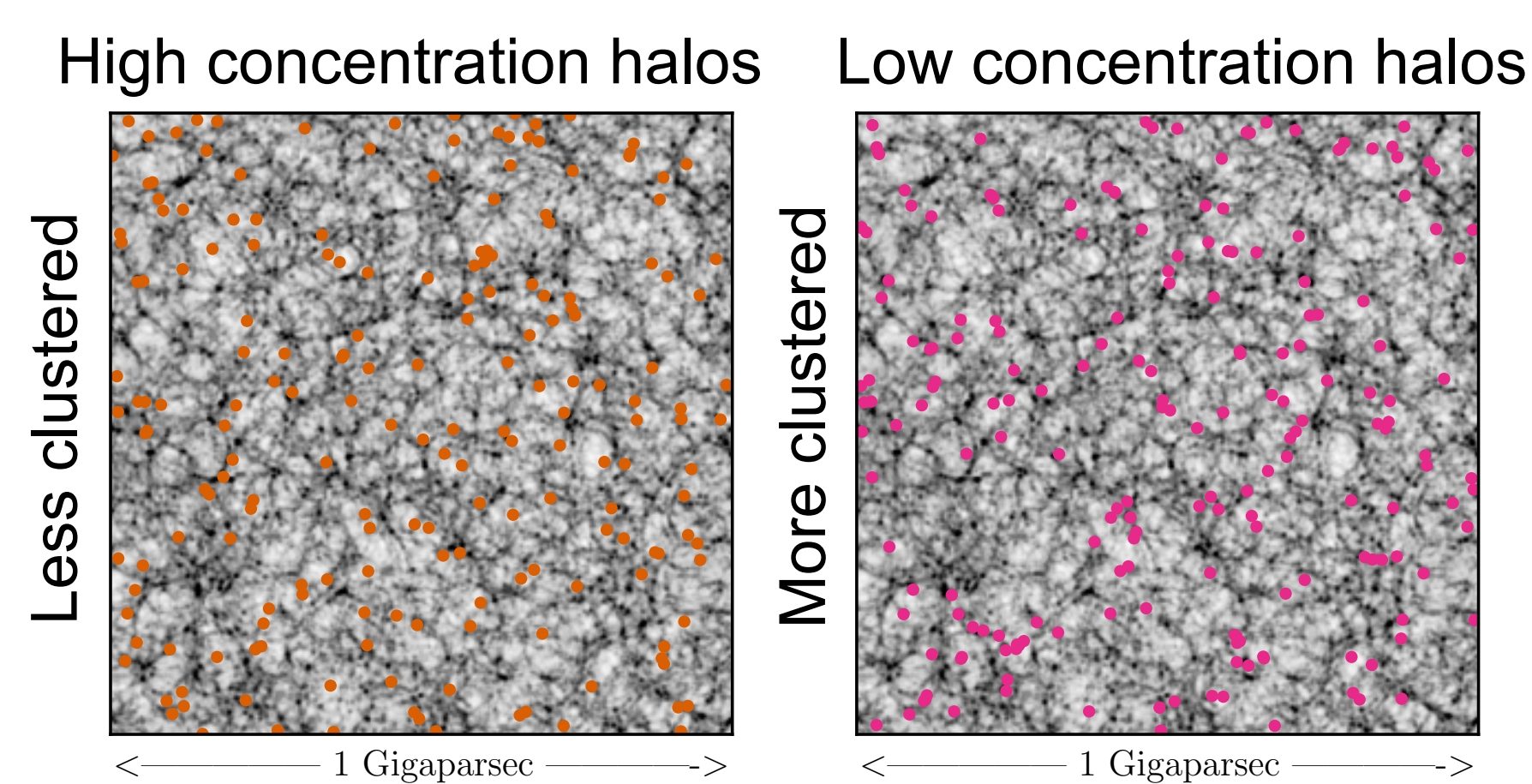
•Cosmological information, such as the nature dark energy, is imprinted in the spatial clustering of matter distribution.

•Since dark matter, which makes up about 80% of matter in the Universe, cannot be directly observed, we need to infer the matter distribution from the distribution of galaxies or galaxy clusters.

•Since clustering amplitudes of galaxies and galaxy clusters (which are formed in dark matter halo) is highly biased compared to the underlying matter distribution, this bias should be properly modeled to extract the cosmological information.

•In the standard bias model, the clustering amplitude depends on *only* halo mass. However, theoretical studies predict it also depends on other properties such as the steepness of the halo density profile (halo concentration) and formation time. Such bias is called *assembly bias* (see figure below).

•There has been no clear observational evidence of assembly bias, but we present the evidence of assembly bias in massive galaxy clusters.



Based on simulations by Prada et al. (2012). Each point indicates the position of a dark matter halo. Left (right) panel shows halos with steep (shallow) concentration profile, and halos that are less (more) clustered.

Measurement

•Data: SDSS DR8 redMaPPer galaxy clusters

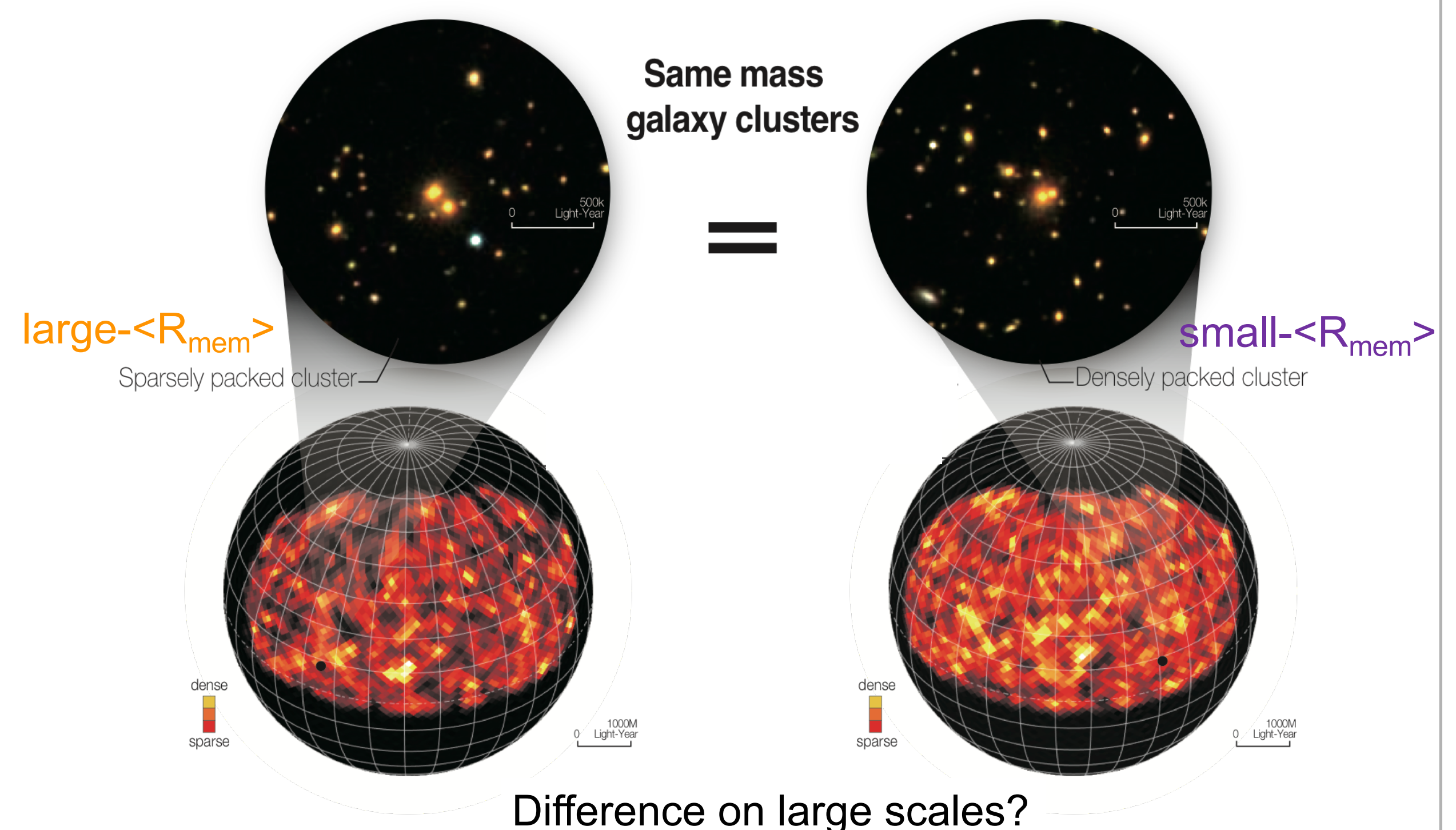
•8,648 clusters spanning $\sim 9000 \text{ deg}^2$ with the number of member galaxies > 20 and $0.1 < \text{redshift} < 0.33$.

•Divide the parent sample into two subsamples based on the average cluster-centric separation of member galaxies.

•subsamples “large- $\langle R_{\text{mem}} \rangle$ ” and “small- $\langle R_{\text{mem}} \rangle$ ”.

•Confirm the two subsamples have the same mass based on the small-scale weak gravitational lensing signal. Weak lensing is sensitive to matter including dark matter, and therefore gives an unbiased estimate of halo mass.

•See if assembly bias is inferred from the large-scale weak lensing signal (clustering of galaxy clusters and neighboring dark matter halos) and clustering signal (clustering of galaxy clusters).



Results

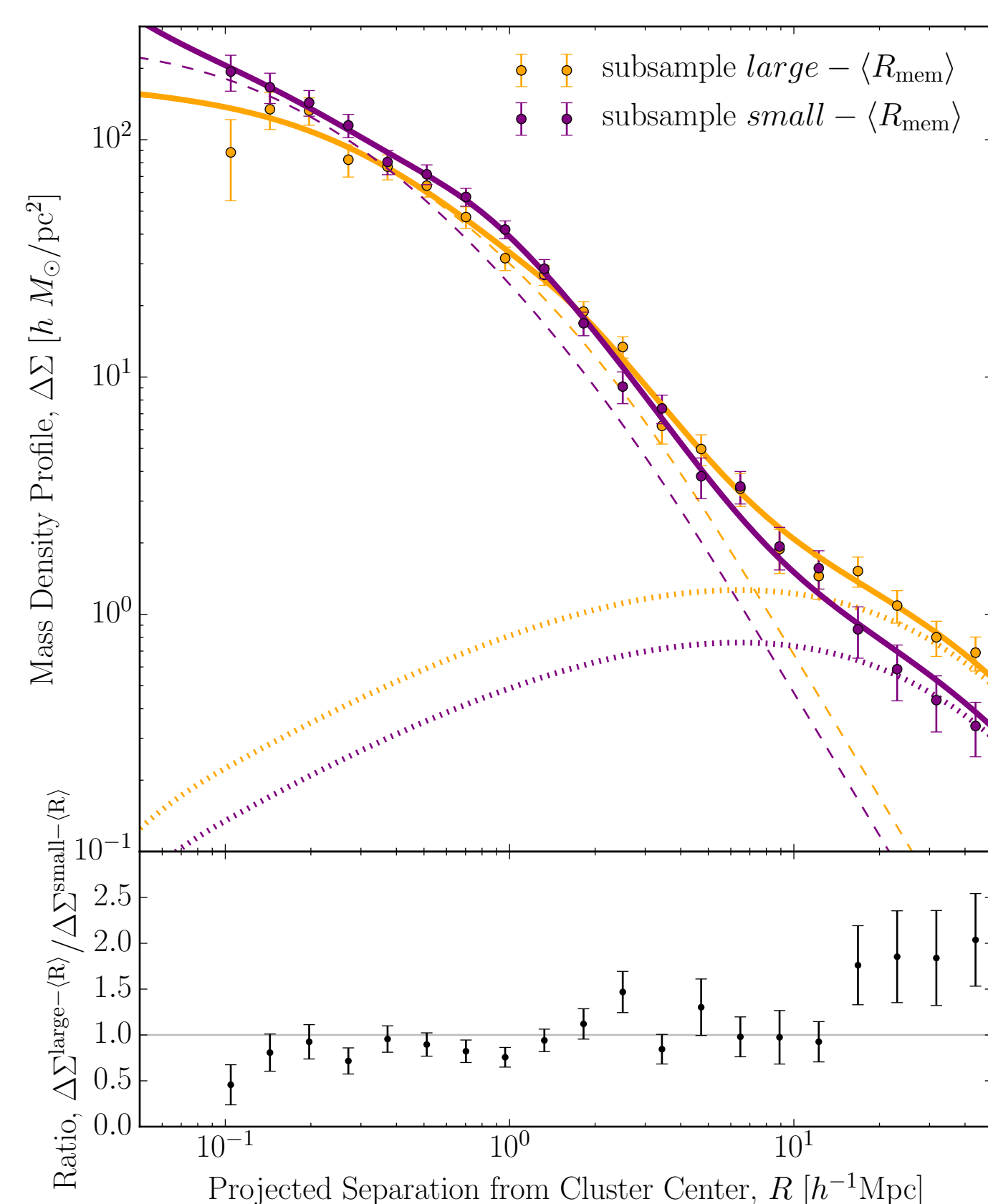
Weak Lensing Signal

•Fitting a theoretical standard profile (NFW, dashed line) to small-scale signal ($R < 10 \text{ Mpc}/h$), we confirm the cluster mass between subsamples is consistent ($M_{200m} \sim 1.9 \times 10^{14} M_{\odot}/h$).

•The difference at large scale ($R > 15 \text{ Mpc}/h$) indicates the evidence of assembly bias. The ratio of the linear bias parameters obtained by the amplitude of cluster-matter clustering (dotted line) is

$$b^{\text{large-}\langle R_{\text{mem}} \rangle} / b^{\text{small-}\langle R_{\text{mem}} \rangle} = 1.64^{+0.31}_{-0.26},$$

which indicates the evidence of assembly bias at 2.5σ significance.

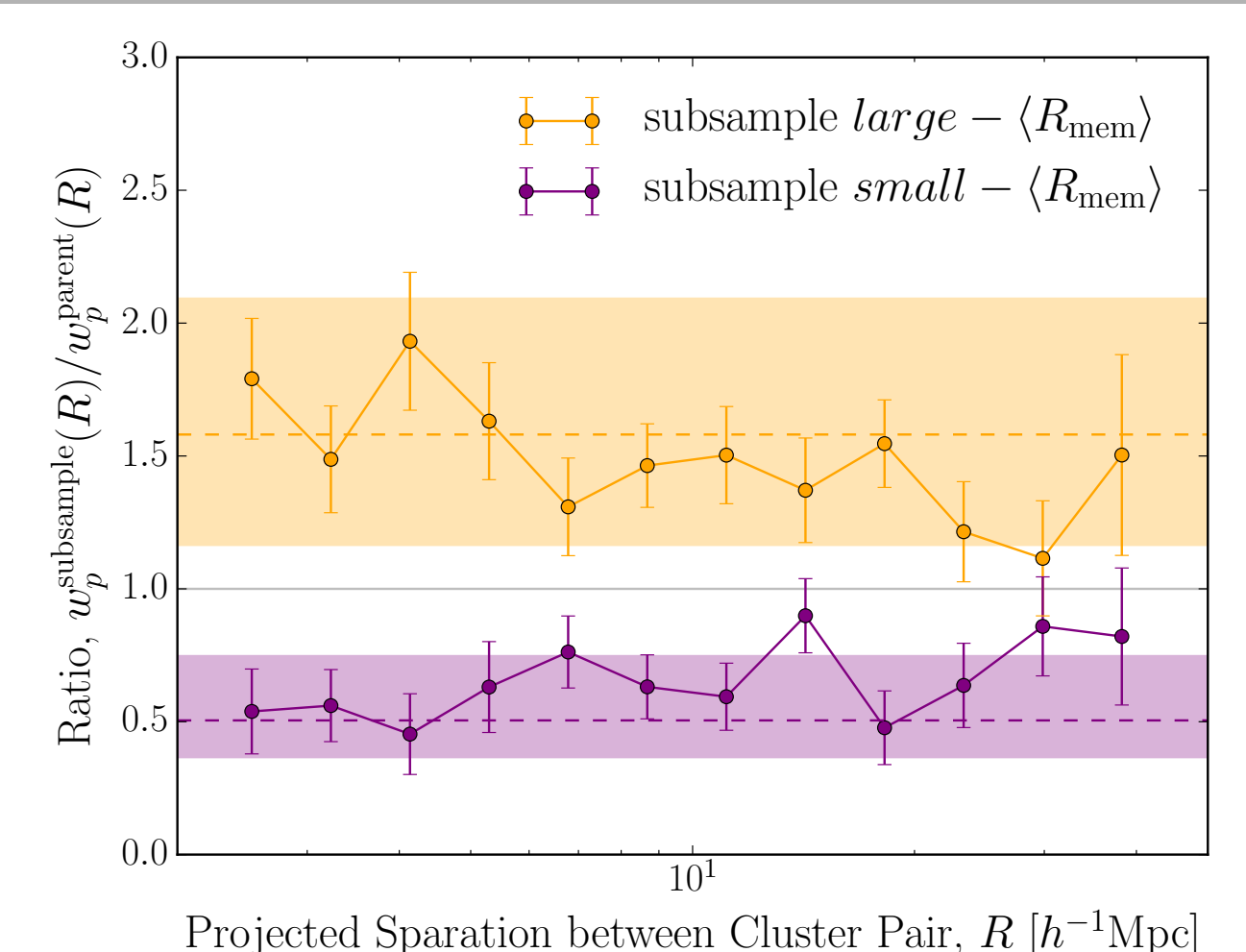


Clustering Signal

• The ratio of clustering signal of subsamples is

$$[w_p^{\text{large-}\langle R_{\text{mem}} \rangle} / w_p^{\text{small-}\langle R_{\text{mem}} \rangle}]^{1/2} = 1.40 \pm 0.09,$$

which indicates the evidence of assembly bias at 4.4σ significance.



Discussions and Conclusions

•We find **the observational evidence of assembly bias** in massive galaxy clusters both from large-scale weak lensing signal (2.5σ) and clustering signal (4.4σ). Cross-correlation with photometric galaxies yields 6.6σ significance (More, HM et al., ApJ, 825:39, 2016).

•Proper modeling of assembly bias is necessary for future cosmology surveys such as WFIRST and Euclid.

•Possibilities of systematic effect that can mimic assembly bias, such as projection effect in weak lensing signal and statistical fluke due to super clusters, are excluded.

•Systematic uncertainties in the redMaPPer cluster catalog is being investigated.

•Details of this study can be found in Miyatake et al., PRL, 116(4):041301, 2016.



The effect of detector nonlinearity on the Wide-Field Infrared Survey Telescope (WFIRST) PSF profiles for weak gravitational lensing measurements

Principal Investigator: **Andrés Alejandro Plazas Malagón (3268-Caltech)**

Jason Rhodes (3268), Chaz Shapiro (389E), Roger Smith (Caltech), Rachel Mandelbaum, Arun Kannawadi (Carnegie Mellon U.)
Jet Propulsion Laboratory, California Institute of Technology

Executive summary: One of WFIRST's main scientific goals is to learn about dark energy through the use of weak gravitational lensing (WL). To extract the WL signal from galaxy shape measurements, the Point Spread Function (PSF) of the system must be known with extreme accuracy. Errors in PSF shape and size estimation will propagate into biases of cosmological parameters (such as the amount of dark energy and dark matter in the Universe). We study the impact that detector nonlinearity (NL) has on PSF determination for WL measurements. We find that NL induces errors in PSF size and shape larger to what is tolerable by accurate WL measurements. We derive a fitting formula that can be used to estimate WFIRST detector NL requirements once a true PSF error budget is established. Our work directly led to funding for lab emulations for WFIRST at JPL.

Motivation

- Dark matter and dark energy are the dominant components of the Universe (~95%). Little is known about their nature.

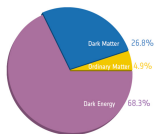


Fig. 1: Composition of the Universe. Credit: ESA-Planck

- The study of the nature of dark matter and dark energy are aligned with NASA's strategic objectives in astrophysics of discovering how the universe works and explore how it began and evolved.

Gravitational Lensing

- The dark matter distribution of the Universe distorts spacetime, bending light from background sources on its way to our detectors.



Fig. 2: When clusters collide, the gas (red, detected by x-rays) and the dark matter separate (blue, "seen" thanks to lensing). Credit: X-ray: NASA/CXC/CfA/M.Markevitch et al.; Optical: NASA/STScI; Magellan/University of Arizona/D.Clowe et al.; Lensing: Magellan/STScI; ESO WFI; Magellan/University of Arizona/D.Clowe et al.

- Gravitational lensing depends on the amount of dark matter and on the geometrical configuration between the observer, the lensing object, and the source.



Fig. 3: Weak lensing of background galaxies due to the large scale distribution of dark matter in the Universe. Credit: Bell Labs/UCent.

- It is an ideal tool to measure the expansion rate and growth of structure of Universe.

- Both depend on the interplay between dark energy and dark matter (the former tends to push the Universe apart, while the latter tries to pull it together).

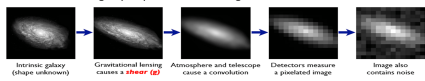
Weak lensing and shape measurement

- When the gravitational lensing distortions on galaxy shapes are only of the order of 1-2%, we are in the weak lensing regime.

- Galaxy shape measurement is highly nontrivial.

The Forward Process.

Galaxies: Intrinsic galaxy shapes to measured image:



Stars: Point sources to star images:

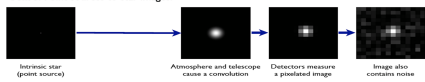


Fig. 5: The weak lensing signal ("shear") must be extracted from a noisy, pixelated, PSF-convolved image of a galaxy. Credit: [2]

- The measurement uncertainty is dominated by systematic errors.

- To extract the weak lensing signal, the Point Spread Function of the system must be deconvolved from the galaxy shapes.

- The inaccurate modeling of the Point Spread Function (PSF) of the system is one of the main systematic errors.

Detector nonlinearity in near infrared detectors and its impact on the WFIRST PSF (Plazas et al., PASP, 2016 [1])

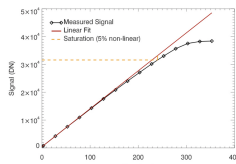


Fig. 4: Nonlinearity in a particular pixel of the Wide Field Camera 3 (WFC3) infrared detector (H2RG) mounted on the Hubble Space Telescope. Credit: WFC3 Data Handbook.

- WFIRST will use near-infrared detectors (H4RG) to perform a weak lensing survey.

- This type of detectors have not been used for WL investigations. Like all detectors (see Fig. 4), they are subject to conversion gain nonlinearities (voltage response to collected photo-charge).

- We used the code GALSIM [3] to study the effect of NL on the size and ellipticity of the WFIRST PSF (see Fig. 5). Errors in these properties bias the weak lensing signal, which in turn biases the determination of cosmological parameters.

- We find that NL induces errors in PSF size and shape larger to what is tolerable by accurate WL measurements (see Fig. 6).

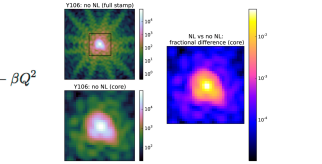


Fig. 5: Example of a WFIRST PSF before and after applying the NL effect, modeled as a quadratic function in the charge collected by each pixel. The effect is small (about 1% at the core), but sufficient to create considerable biases for WL measurements (see Fig. 6). From Plazas et al., 2016 [1]

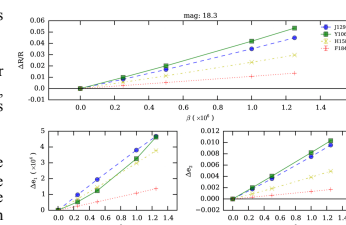


Fig. 6: Errors in size and ellipticity as a function of the quadratic parameter β in our NL model. For a typical value of $\beta = 5e-7 e^-$, NL induces errors in the size and ellipticity of about 1e-3 and 2e-3 respectively (H158 band), larger than the required values of 1e-3 and 4.7e-4 on the knowledge of the size and ellipticity of the PSF in order not to bias cosmological parameter inferences from WL experiments. From Plazas et al., 2016 [1].

Future work and connection to the WFIRST cosmology Science Investigation Team

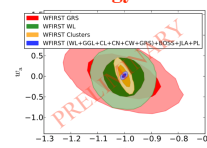


Fig. 8: Likelihood analysis performed with COSMOLIKE [4] to determine the dark energy parameters w_p and w_a (constant and time-dependent components respectively). Credit: T. Eicher.

*These are GGL (galaxy galaxy lensing), CL (cluster lensing) and WL (weak lensing of the large scale structure or cosmic shear). Other cosmological observables are also included in the blue contour (CN, CW, and GRS), as well as priors from other experiments (BOSS, JLA, PL).

National Aeronautics and Space Administration

Jet Propulsion Laboratory
California Institute of Technology
Pasadena, California

www.nasa.gov
Copyright 2016. All rights reserved.

- Dark energy parameters are determined by a joint likelihood analysis of different cosmological observables that include WL* (blue in Fig. 8).

- The uncertainty contours in Fig. 8 take into account only statistical errors. The systematic error produced by an effect such as NL should lie within the blue contours.

[1] Plazas, A., Shapiro, C., Kannawadi, A., Mandelbaum, R., Rhodes, J., Smith, R. "The effect of detector nonlinearity on WFIRST PSF profiles for weak gravitational lensing measurement". arXiv:1605.01001. Accepted for publication in the Publications of the Astronomical Society of the Pacific (PASP).
[2] Bradač, S. et al. "Handbook for the GREATFOU Challenge: An image analysis competition for cosmological lensing". Annals of Applied Statistics, vol. 3, p. 6-27, 2009.
[3] Rowe et al. "GALSIM: The world's galaxy image simulation toolkit". Astronomy and Computing, Volume 10, p. 121-130, 2015.
[4] Kravtsov, E., Eicher, T. "Cosmofit: Cosmological Likelihood Analysis for Photometric Galaxy Surveys". arXiv:1401.0577v2, 2016.

- The results of our study can be used to derive requirements on NL for the WFIRST detectors for different sets of tolerances on PSF properties (see Fig. 7).

- For an example set of assumed requirements on PSF size and ellipticity (1e-4 and 4.7e-5, respectively) and a quadratic model for NL, we find (see Fig. 7) that the NL model parameter β should be calibrated to about 1% to 2.4% (H158 band).

- This work directly led to funding for lab emulations for WFIRST at JPL.

Fig. 7: Fractional error in PSF size and absolute error in PSF ellipticity components normalized by the NL model parameter β , as a function of magnitude for the four HSL filters (I29, Y106, H158, and F184). The ordinate axis in each plot represents the slope of the linear relationships in Fig. 7, derived by linear fitting of points around the vicinity of a given β in each curve of that figure. From Plazas et al., 2016 [1].

Dissecting the Inter-Stellar Medium through Intensity mapping

Paolo Serra (3268)

Olivier Doré (3268) & Guilaine Lagache (LAM, Marseille)

INTRODUCTION

-Constraining the high-redshift star formation history and the reionization of the Universe are key goals of cosmology.

-The Carbon 158 μm emission line ([CII]) is one of the most important tracers of dusty star formation at high redshift

-Intensity mapping technique: instead of detecting individual sources, it measures fluctuations on large regions of the sky in a wide frequency band, increasing sensitivity to faint sources and their clustering

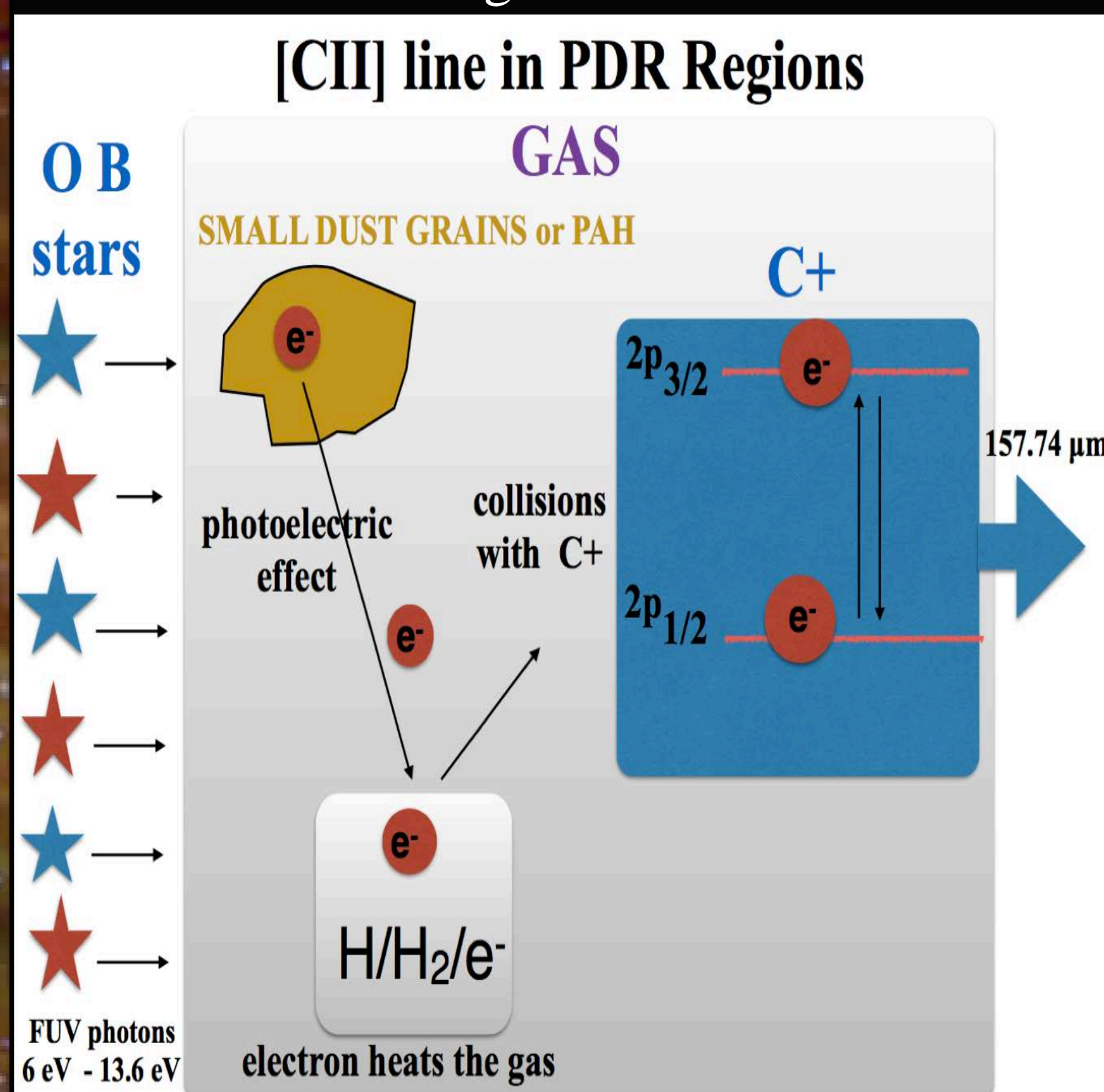
-Intensity Mapping enables us to measure brightness fluctuations of the [CII] emission line, and compute its 3D auto-power spectrum and cross-spectra with other emission lines (from Oxygen, Nitrogen, etc.) produced in the Inter-Stellar Medium (ISM)

-Constraints on the aggregate emission from galaxies to understand the interplay between energetic sources, and the gas and dust at very high redshift.

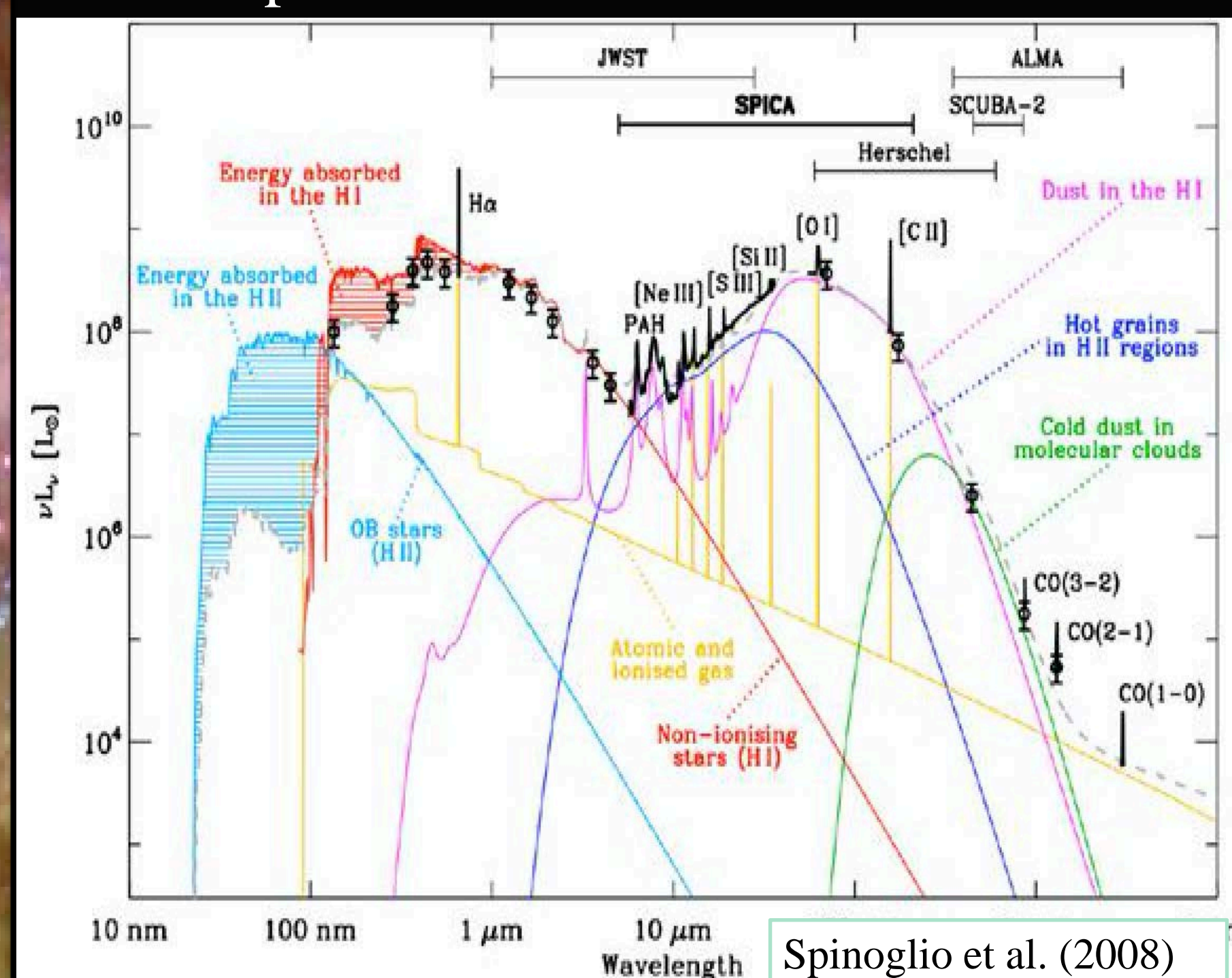
-Emission lines from external galaxies are an important foreground when measuring spectral distortions of the Cosmic Microwave Background spectrum with future space-based experiments like PIXIE; the Intensity Mapping technique allow us to better constrain this foreground.

NEUTRAL CARBON EMISSION

Black box: Input is radiation field from stars, output is emission line at 158 μm . The main mechanism is photoelectric ejection of electrons from dust grains



The Spectral Energy Distribution of a galaxy contains many emission lines produced in different phases on the ISM

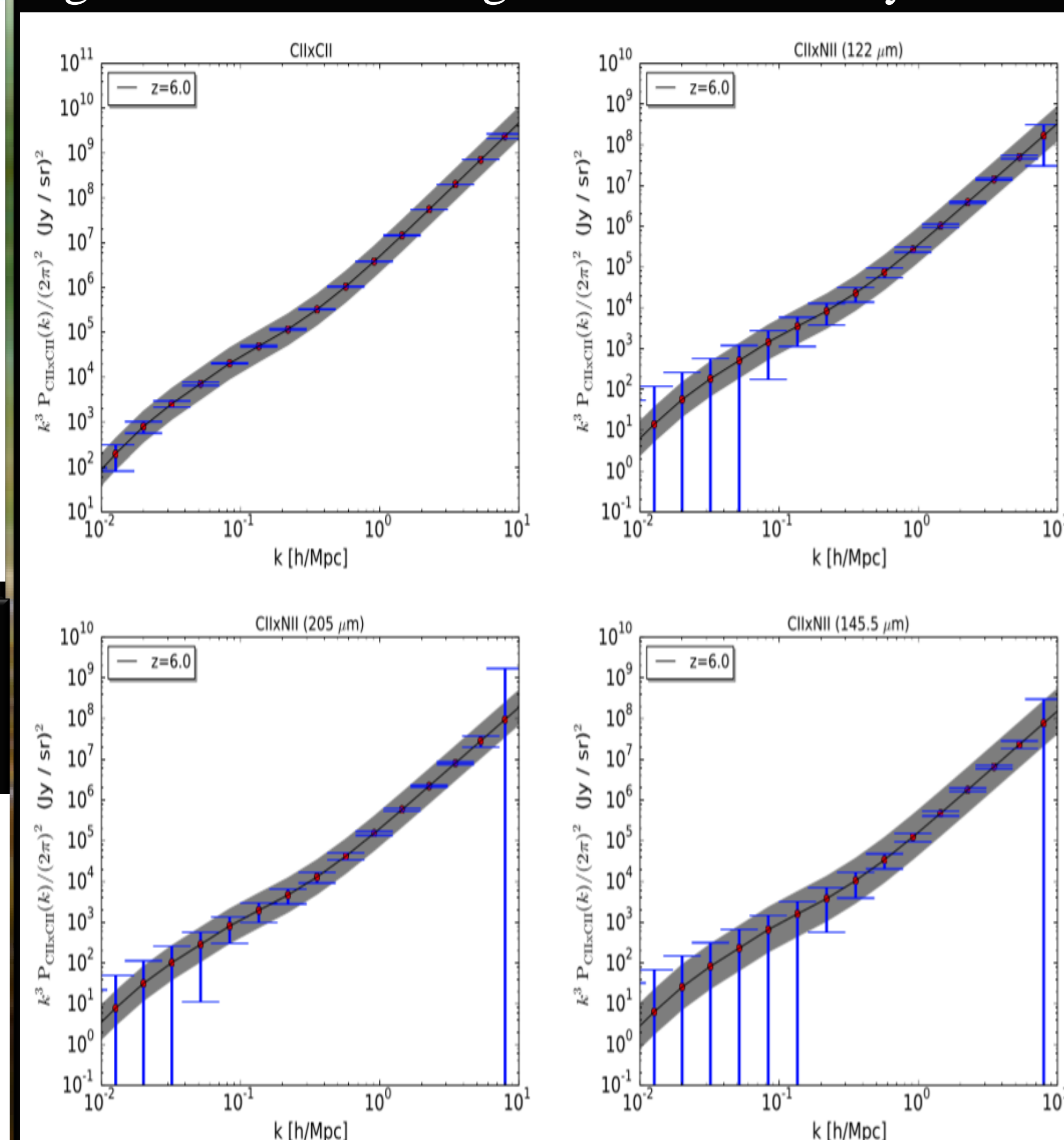


EXPERIMENTAL SETUP

A typical setup for an upcoming ground based-survey consists of a 10 m dish, 16000 bolometers and a 64 beam spectrograph working in the range 200-360 GHz, and with resolution ~ 0.5 GHz

RESULTS

Carbon auto-power spectrum and cross-spectra with Oxygen and Nitrogen will be detectable at high SNR with future ground based surveys



CONCLUSIONS

- Intensity Mapping is a powerful probe of the physics of the early Universe
- The cross-correlation between different lines allows us to gain insights on the various phases of the ISM, and to avoid foreground contamination from low-redshift lines
- Strong constraints on star formation history at high redshift
- Line emissions from multiple atoms/molecules at multiple redshifts are an important foregrounds for future surveys aiming at constraining CMB spectral distortions. Intensity mapping surveys, by constraining the mean amplitude of emission lines, will help constraining the global contamination signal

